Title

Segmentation of X-ray CT and Ultrasonic Scans of Impacted Composite Structures for Damage State Interpretation and Model Generation

Author

Ellison, Andrew Cannon

Publication Date

2020

UNIVERSITY OF CALIFORNIA SAN DIEGO

Segmentation of X-ray CT and Ultrasonic Scans of Impacted Composite Structures for Damage State Interpretation and Model Generation

A dissertation submitted in partial satisfaction of the

requirements for the degree Doctor of Philosophy

in

Structural Engineering

by

Andrew C. Ellison

Committee in charge:

Professor Hyonny Kim, Chair
Professor Jiun-Shyan Chen
Professor Veronica Eliasson
Professor William Hodgkiss
Professor Kenneth Loh

2020

The Dissertation of Andrew C. Ellison is approved, and it is acceptable in quality and form for publication on microfilm and electronically:

Chair

University of California San Diego

2020

Table of Contents

List of Abbreviations

CAD	Computed aided design
CAI	Compression after impact
CDM	Continuum damage mechanics
CFRP	Carbon Fiber Reinforced Polymers
CT	Computed tomography, X-ray computed tomography in this work
DCDT	Direct current deformation transducers
DIC	Digital Image Correlation
FEA	Finite element Analysis
IGA	Isogeometric Analysis
NDE	Non-Destructive Evaluation
TOF	Time of Flight (between UT waveform peaks)
UCSD	University of California, San Diego
UT	Ultrasonic testing, specifically single sided pulse-echo ultrasonic scanning in this work

List of Figures

List of Tables

Acknowledgements

I would first like to provide my sincerest thanks to my advisor Professor Hyonny Kim for continually guiding me through my Ph.D. study. No matter how lost I got, he could always get me back on course.

During this program I had the good fortune to spend two summers at the NASA Langley Research Center where the mentorship and help I received greatly accelerated my research. I would most like to thank my technical advisors Drs. Frank Leone and Cheryl Rose who kept me on track towards answering the right questions and Wade Jackson kept scanning specimens for me no matter how busy it got. I would also like to thank the other research engineers of the Durability, Damage Tolerance, and Reliability Branch: Carlos Dávila, Andrew Bergan, Will Johnston, and James Ratcliffe for their help and advice during my time at Langley. Lastly I would like to thank the technicians who made sure all of my tests ran smoothly: Teresa O'Neil, Nate Gardner, and Michael McNeill.

Throughout my Ph.D. I have had the pleasure of working alongside Marco Pigazzini and Eric Kim, who have both kept me sane through all of the modeling and experiments. I would also like to thank all my friends colleagues at UCSD: Albert Liang, Abdullah Hamid, Rodrigo Chavez, Chaiane Wiggers de Souza, Moonhee Nam, Kostas Anagnostopoulos, Javier Buenrostro, Adrian Rivera, Mimi Ngo, Margherita Capriotti. I would also like to thank the staff of the UCSD Structural Engineering department, especially Steve Porter who provided a lot of help in making our experiments work, even when on a time crunch.

Lastly, I would like to thank my family for their continual support of everything I do and for pushing me forward. I would also like to thank my girlfriend Sarah Haroon for sticking with me through this entire Ph.D. journey.

Technical Acknowledgements:

These works were supported under the NASA Advanced Composites Project No. 15-ACP1-0021.

Chapter 3 contains unpublished work researched together with Hyungsuk Eric Kim and Hyonny Kim.

Chapter 4 is, in part, an edited version of work that had previously appeared in:

Ellison, A., & Kim, H. (2018). Computed tomography informed composite damage state model generation. *Journal of Composite Materials*, *52*(25), 3523–3538. https://doi.org/10.1177/0021998318773464. The author of this dissertation was the primary investigator and author of this study.

Ellison, A., & Kim, H. (2019). Shadowed delamination area estimation in ultrasonic C-scans of impacted composites validated by X-ray CT. *Journal of Composite Materials*. SAGE Publications Ltd. https://doi.org/10.1177/0021998319865311. The author of this dissertation was the primary investigator and author of this study.

Ellison, A., & Kim, H. (2019). Automated Computed Tomography Segmentation of Impact- Damaged Curved Composite Structures. DEStech Publications.

https://doi.org/10.12783/asc34/31260. The author of this dissertation was the primary investigator and author of this study.

Parts of Chapter 5 are taken in part from:

Pigazzini, M. S., Bazilevs, Y., Ellison, A., & Kim, H. (2018). Isogeometric analysis for simulation of progressive damage in composite laminates. *Journal of Composite Materials*, *52*(25), 3471–3489. https://doi.org/10.1177/0021998318770723. The author of this dissertation was a co-author in this work. Comparisons of CT results with IGA modeling was developed in collaboration with Marco Pigazzini.

Methods for converting NDE into flat panel CAI models are an edited version of work originally published as:

Ellison, A., & Kim, H. (2018). Computed tomography informed composite damage state model generation. *Journal of Composite Materials*, *52*(25), 3523–3538. https://doi.org/10.1177/0021998318773464. The author of this dissertation was the primary investigator and author of this study.

Vita

2015 Bachelor of Science, Structural Engineering, University of California San Diego

2017 Master of Science, Structural Engineering, University of California San Diego

2020 Doctor of Philosophy, Structural Engineering, University of California San Diego

Publications

Ellison, A., & Kim, H. (2018). Computed tomography informed composite damage state model generation. *Journal of Composite Materials*, 52(25), 3523-3538.

Ellison, Andrew, and Hyonny Kim. "Shadowed delamination area estimation in ultrasonic C-scans of impacted composites validated by X-ray CT." *Journal of Composite Materials* 54.4 (2020): 549-561.

Ellison, A., Kim, H., "Computed Tomography Informed Composite Damage State Model Generation." American Society of Composites, 32nd Conference. West Lafayette, IN. Oct 23-25, 2017.

Ellison, A., Kim, H., "Shadowed Delamination Area Estimation in UT C-Scans of Impacted Composites Validated by X-Ray CT." American Society of Composites, 33rd Conference. Sept 24-26, 2018.

Ellison, A., Kim, H., "Automated Computed Tomography Segmentation of Impact-Damaged Curved Composite Structures." American Society of Composites, 34th conference - Sept 23-25, 2019.

Ellison, A., Kim, H.E., Kim, H., "Guided Wave NDE and Residual Strength of Composite Panels with Stiffener Impact Damage." Twenty-Second International Conference on Composite Materials, Melbourne, Australia, 2019.

Pigazzini, M. S., Bazilevs, Y., Ellison, A., & Kim, H. (2018). Isogeometric analysis for simulation of progressive damage in composite laminates. *Journal of Composite Materials*, 52(25), 3471-3489.

Bazilevs, Y., Pigazzini, M. S., Ellison, A., & Kim, H. (2018). A new multi-layer approach for progressive damage simulation in composite laminates based on isogeometric analysis and Kirchhoff–Love shells. Part I: basic theory and modeling of delamination and transverse shear. *Computational Mechanics*, 62(3), 563-585.

Pigazzini, M. S., Bazilevs, Y., Ellison, A., & Kim, H. (2018). A new multi-layer approach for progressive damage simulation in composite laminates based on isogeometric analysis and Kirchhoff–Love shells. Part II: impact modeling. *Computational Mechanics*, 62(3), 587-601.

Abstract of the Dissertation

Segmentation of X-ray CT and Ultrasonic Scans of Impacted Composite Structures for Damage State Interpretation and Model Generation

by

Andrew C. Ellison

Doctor of Philosophy in Structural Engineering

University of California, San Diego, 2020

Professor Hyonny Kim, Chair

Composites are frequently used in aerospace structural applications due to their high strength to weight performance, but due to their layered structure they are vulnerable to transverse impacts. Impact damage in composite laminates often consists of highly interactive damage modes composed of delamination, matrix cracking, and fiber breakage. In order to ensure the safety of composite structures, a variety of non-destructive evaluation (NDE) techniques are used to characterize impact damage. However, procedures for utilizing NDE to create and validate models of residual strength after impact are not yet established due to either limitations in the characterization of impact damage, as in the case of Ultrasonic pulse-echo scanning (UT), or due to the complexity of interpretation of the NDE technique, as in the case of X-ray computed tomography (CT). Improved quantification of damage from CT and UT characterization may lead to improved predictive capabilities for the prediction of structural performance after an impact event.

This work presents a novel automatic damage segmentation procedure for CT scans of impacted composites that converts the complex 3D dataset into simplified damage visualizations and 2D damage maps for each composite layer. The results of this procedure were utilized to create and validate a modeling procedure to improve UT characterization of impact damage, and to validate and generate finite element models of impact damage and residual strength performance. The generated residual strength models were created with varying levels of damage modeling fidelity and it was found that the level of damage modeling needed for accurate failure prediction depends greatly on the structural geometry and the presence of major damage features. This NDE and modeling effort was supported by a series of impact and residual strength experiments for flat and stringer stiffened composite panels. The developed techniques proved capable of characterizing impact damage in a variety of structural configurations and establishing models that incorporate this damage at different levels of complexity.

1 INTRODUCTION

1.1 MOTIVATION

Carbon fiber reinforced materials are being utilized in an increasing number of critical structural applications that may be subjected to impact events during their lifetime, particularly in modern aircraft design [1]. In order to ensure the safety of composite structures after these events, an understanding of how impact damage reduces the strength and lifespan of such structures is required. When a composite component undergoes an impact, a complex state of damage may develop based on the structure of the composite with primary damage modes being fiber breakage, matrix cracking, and delamination [2, 3]. Even in the case of low velocity impacts that leave barely visible indentation, delamination and matrix cracking could severely reduce the strength of the structure, particularly the compressive strength which may be reduced by up to 50% [4]. Thus for these composite structures, load bearing capacity must be maintained throughout the component's service life. The FAA Advisory Circular (AC) 20-107B [5] established guidelines for minimum damage tolerance and load carrying capability after damage events based on damage detect-ability criteria. These categories are summarized in Figure 1.1 as presented by Bouvet and Rivallant [6]. Low velocity impacts such as tool drops generally fall into either category 1 or 2 for detect-ability. Category 1 damage must be shown to withstand the structure's designed ultimate load capacity during the aircraft's service life. Often this verification is performed through expensive experimental trials that take into account several impact types and severities. Due to the potential cost savings of reducing experimental requirements, advanced finite element modeling has been increasingly used as a supplement to experiments.

However, due to the complexity of the composite residual strength after impact problem, standardized high fidelity and accurate modeling techniques are not yet fully established.

This work seeks to improve residual strength modeling capability by incorporating non-destructive evaluation (NDE) techniques, such as X-ray computed tomography and ultrasonic pulse-echo scanning, into the modeling pipeline at varying levels of fidelity. First, NDE characterization provides a potential for improved quantification of model performance, allowing impact model verification to move forward from simple metrics of overall damage area and force-history response to verifications of damage location and shape at each individual composite layer. Second, the incorporation of NDE detected damage into residual strength modeling allows for a more physically accurate representation of the initial damage state. Development of methods to further utilize NDE in modeling contexts may hasten the creation of verified modeling techniques to demonstrate structural capacity, thereby reducing the need for costly residual strength testing.

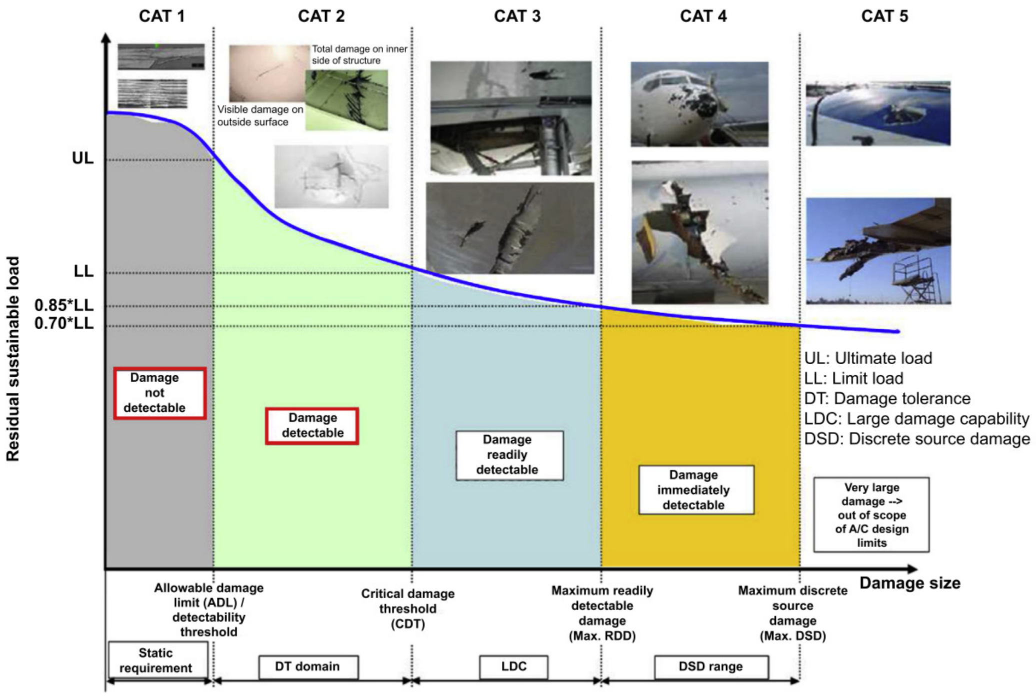

Figure 1.1. Categories of damage and design requirements for aircraft. Low velocity impact generally falls under CAT 1. [6]

1.2 OBJECTIVE

The broad goal of this work is to improve the understanding of composite impact damage and its effect on structural performance. A major component of this effort is based around characterizing impact damage using X-ray computed tomography (CT) and ultrasonic scanning and using these results to validate impact simulations, create NDE informed residual strength models, and assess the damage characterization performance of CT and UT.

The first objective of this research was segmentation of NDE datasets for impacted composite structures such as ultrasonic pulse-echo scanning and X-ray computed tomography scans. Segmentation of these datasets consists of converting the scan data into information at each ply and interface in order to enable interpretation of the damage in the context of the composite structure. The resulting automated segmentation procedures were applied to scans of flat and curved structures and tools were developed for generating models and validating impact simulations.

The second objective of this research was to utilize segmented results to improve modeling techniques and capabilities for impact damage. First, impact simulations were performed and delamination results were compared with layer-by-layer damage maps from the CT scans to verify that the modeling technique not only captures the damage extent, but also location and shape. Second, damage states from NDE were imported into finite element modeling to quantify what level of damage modeling fidelity is required to capture the effect of impact damage on residual composite strength.

The last objective of this research was to create a large, publicly accessible dataset of impacts, NDE, and residual strength testing so that researchers could more easily create and validate models of residual strength after impact.

1.3 BACKGROUND/LITERATURE REVIEW

This section provides a summary of the current state of the art in composite impact and residual strength research including the use of finite element modeling and non-destructive evaluation. A more detailed summary of analysis methods for non-destructive evaluation data and their use in residual strength modeling is provided in subsequent sections. First a review of impact and residual strength techniques is given for flat panel impact cases and then for stiffened structures.

In an impact event on a composite structure, a complex damage state can form internally with little to no external evidence of damage. Previous studies of impact damage in composites have focused on several different features of the impact damage formation including: dent depth versus delamination size [7], the interactions between matrix cracking and interfacial disbond [8–11], the effect of delaminations on the buckling stability [12], and the reduction in stiffness of the damaged region [8]. In addition, the overall response of composites to a dynamic impact event and the effects of boundary conditions and impactor and specimen geometry have also been thoroughly studied [2, 3].

For flat panel impact and residual strength studies, the primary test used to verify post-impact strength at the coupon level is the ASTM D7137 standard [13] which utilizes a 4x6" coupon to create a damage state near the limits of detect-ability and perform residual strength testing where the failure is primarily driven by the impact damage state as opposed to global buckling deformation. Studies of impact and residual strength modeling generally take one of two strategies: modeling impact and the residual strength test with the same model, or modeling an initial damage state taken from a non-destructive evaluation scan as a seed damage point. Recent work that takes the two-step approach to impact and residual strength modeling includes work by Tan et al. [14] which utilized cohesive zones between layers and non-linear plastic behavior for the composite matrix to capture the residual indentation from the impact event. Also, González et al. [15] presented an impact and residual strength model that captured impact damage from modeling as a starting point for a residual strength model. The proposed benefit of this modeling approach is that the model may be able to capture damage modes that are difficult to capture with non-destructive evaluation. However, these approaches are still limited to only capturing damage modes that are explicitly included, whereas a non-destructive scan may detect certain damage modes that are not captured by this two step approach to modeling residual strength.

Other approaches to residual strength modeling are generally based on an initial damage state detected from non-destructive evaluation scanning. Moura et al. [16] presented an input method of using a single large delamination based on ultrasonic scanning to identify an initially disbonded region. Both Suemasu et al. [17] and Craven et al. [18] presented compression after impact models that incorporated more complex delamination shapes by assuming a spiral delamination shape through the thickness at multiple layers. More recently, Action et al. [19] presented an extended finite element model of residual strength incorporating CT and UT data to generate a residual strength model. Approaches to model generation based on non-destructive evaluation data are explored more in Section 5.2.

For stiffened structures, impact damage to stringers on stiffened panels is of concern because these are key load carrying elements. Two of the most commonly studied structural arrangements are the single stringer stiffened panel [20] and the multi-stringer panel [21]. Impacted stringers can exhibit two major failure modes under post-impact compression loading, depending on the location and severity of the impact. The first major failure mode is stringer-skin disbond growth of the initial disbond area caused by skin side impacts under the flange. The second major failure mode of interest is due to crippling of the stringer caused by internal damage to the stringer itself (e.g., from internal impact directly onto the stringer). Several authors have investigated impacted post-buckling response of stringer stiffened panels with respect to the first type of damage. Bisagni et al. [20] presented a study of single stringer panel damage tolerance using Teflon inserts between the skin and stringer flange to simulate damage from an impact event. Riccio et al. [12] also investigated the inclusion of a Teflon disk as an initial damage state in a multi-stringer panel. In addition to investigations of disbond damage between the stringer and skin, Ridha et al. [22] has investigated stringer impact damage onto omega-shaped stiffeners, but to the authors' knowledge, residual strength testing after this type of impact is not published in the literature. In this study we investigate impacts and residual strength on both skin-side flange-impacted and direct cap-impacted composite stringers.

1.4 APPROACH

This project targets the entire scope of residual strength after impact testing, with a specific focus on the analysis of non-destructive evaluation data. The overall flowchart of this project is shown in Figure 1.2. As can be seen in the flowchart, this research leverages several cross-connections between experimental testing and modeling with the final end goal of performing and predicting residual strength after impact. NDE was the primary driver of connections between tests and modeling with a specific push towards implementing NDE information into residual strength modeling. This project was also divided into two major experimental programs. First, impact and residual response of flat standard compression after impact panels and second, impact and residual response of stringer stiffened panels.

This dissertation is organized into four main body chapters. The first two chapters (Chapters 2 and 3) summarize the experimental impacts, non-destructive evaluation, and residual strength testing of the flat panel specimens (Chapter 2) and the stringer stiffened specimens (Chapter 3). Chapter 4 then presents a series of segmentation and analysis methods developed to interpret the collected NDE data into the context of composite structural damage. Chapter 5 then uses those analysis tools to create methods to validate impact modeling and generate residual strength modeling using NDE data as an initial seed damage state.

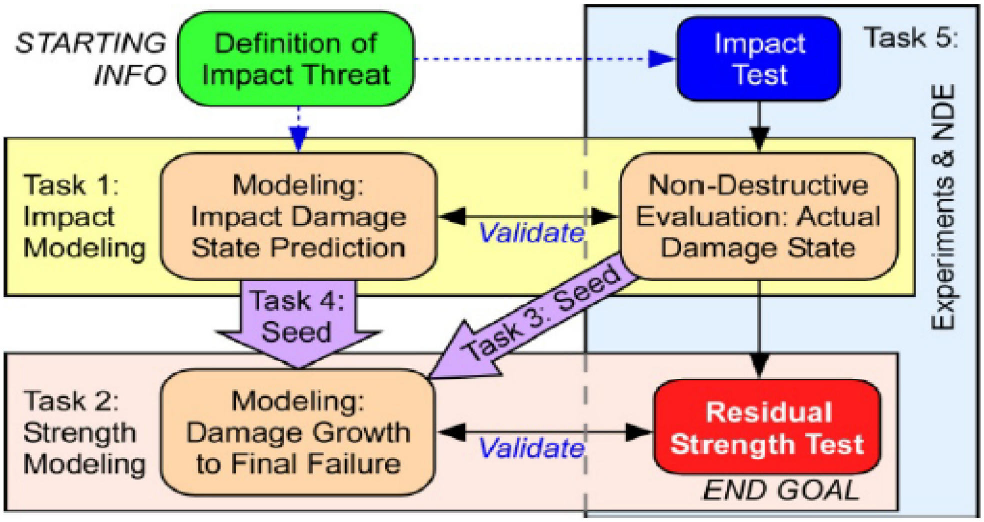

Figure 1.2. Project flowchart.

1.5 NOVEL CONTRIBUTIONS

This work has created several analysis tools and experimental observations including:

1. A novel method for segmenting impact damage states in flat and curved composite laminates from X-ray CT datasets has been developed that converts the 3D CT data into damage maps for each ply and interface.
2. A method for predicting pulse-echo ultrasonic scan results that are lost due to shadowing has been developed that utilizes models of impact damage behavior to predict delaminations based on partial information.
3. Methods to implement segmented CT and UT information into finite element models have been developed at a various levels of fidelity.

4. Fully characterized datasets of impact, NDE, and residual strength have been created for both standard flat panel CAI specimens and single stringer stiffened panel specimens. These datasets will be published publically so that future research can utilize either the experimental or modeling information to create and validate new predictions of residual strength after impact.

1.6 UCSD HOSTED DATABASE

Throughout the course of this work, a large amount of experimental and NDE data was collected. To support future work in impact and residual strength analysis and the development of modeling tools based around NDE data, these datasets were uploaded to the University of California San Diego library data repository. These datasets can be found at the following locations:

Ellison, Andrew C.; Kim, Hyonny (2020). Flat Panel Impact and Residual Strength Testing and Characterization by Ultrasonic and X-Ray Computed Tomography Non-Destructive Evaluation. UC San Diego Library Digital Collections. https://doi.org/10.6075/J01C1V8V

Ellison, Andrew C.; Kim, Hyungsuk Eric; Kim, Hyonny (2020). Stiffened Composite Panel Impact and Residual Strength Testing and Characterization by Ultrasonic and X-Ray CT Non-Destructive Evaluation. UC San Diego Library Digital Collections. https://doi.org/10.6075/J0N29VB8

A more detailed description of the datasets can be found in Appendix A.

1.7 TECHNICAL ACKNOWLEDGEMENT

This work was funded as part of a NASA Research Announcement (NRA) under the Advanced Composites Project at the NASA Langley Research Center. All computed tomography scans for this work were collected at NASA Langley by Wade Jackson. Stringer stiffened panels were manufactured at UCSD with great help from Chaiane Wiggers de Souza, Moonhee Nam, Paul Lee, John Hamrang, and Eric Kim. Impact testing of stiffened panels and preparation of panels for compression testing was conducted as a joint effort with Eric Kim. Comparative impact modeling studies were performed with Marco Pigazzini. Compression testing of both flat and stringer stiffened panels was performed at NASA Langley Research Center with test-stand operation by Teresa Oneil and DIC data collection by Michael Mcneill and Nate Gardner.

2 FLAT PANEL EXPERIMENTS AND NDE

This chapter presents the experimental impacts and residual strength testing of flat composite panels conducted for this dissertation. The experimental program was divided into three components: impact testing, non-destructive damage characterization, and residual strength compression testing. Example NDE scan results for these specimens are shown in this chapter, and further analysis of these results will be given in Chapter 4.

2.1 FLAT PANEL IMPACT TESTING

T800S/3900-2B carbon/epoxy unidirectional 24 ply prepreg panels with a quasi-isotropic $[0/45/90/-45]_{3s}$ layup, were manufactured as 305 x 305 mm panels and cut out following the ASTM D7137 compression after impact (CAI) standard into 102 x 152 mm specimens [13]. To represent the outer surfaces of actual aircraft laminates, an exterior layer of thin plain weave fiberglass was incorporated into the layup, and aircraft-grade paint was applied following autoclave cure. Specimens impacted for this research are summarized in Table 2.1 with specimen names starting with TC-24. Additionally, several specimens from the series of impact tests described in Delaney [23] were utilized for the X-ray CT study presented in Chapter 5 (LV-059, 155, 162). These specimens were impacted via pendulum impactor with additional 3.18 mm rubber strips between the test fixture and the specimen surface and have specimen names starting with LV- and are summarized in Table 2.1. The rubber strips are the primary reason that the impact energies listed for these specimens are in general higher than the impact energies for the TC-24 series specimens with similar damage sizes. Further details about the impact testing of the

LV- specimens are given in Delaney [23] Specimen LV-162 from this set of tests was tested in CAI, however due to excessive specimen taper the test was not considered valid.

Experimental impacts were conducted with a drop weight tower impactor onto the laminates supported by a picture frame test fixture with a 76 x 127 mm test window as shown in Figure 2.1a. Specimens were clamped directly by the impact test fixture. A 5.6 kg impactor with tip radius of 25 mm was used with impact energies of around 20, 25, and 30 J. These energies were chosen to create varying levels of damage that could be well captured by the CT scan area of around 35 x 25 mm. Impacts and other specimen data are summarized in Table 2.1.

Impact force histories are shown for all tests in Figure 2.1. The higher impact energies show more oscillatory behavior compared to the low energy impacts. This may indicate a different response of the boundary conditions, or the creation of more significant internal damage. However, the overall impact contact duration seems independent of the impact energy at about 3.5 ms for all impacts.

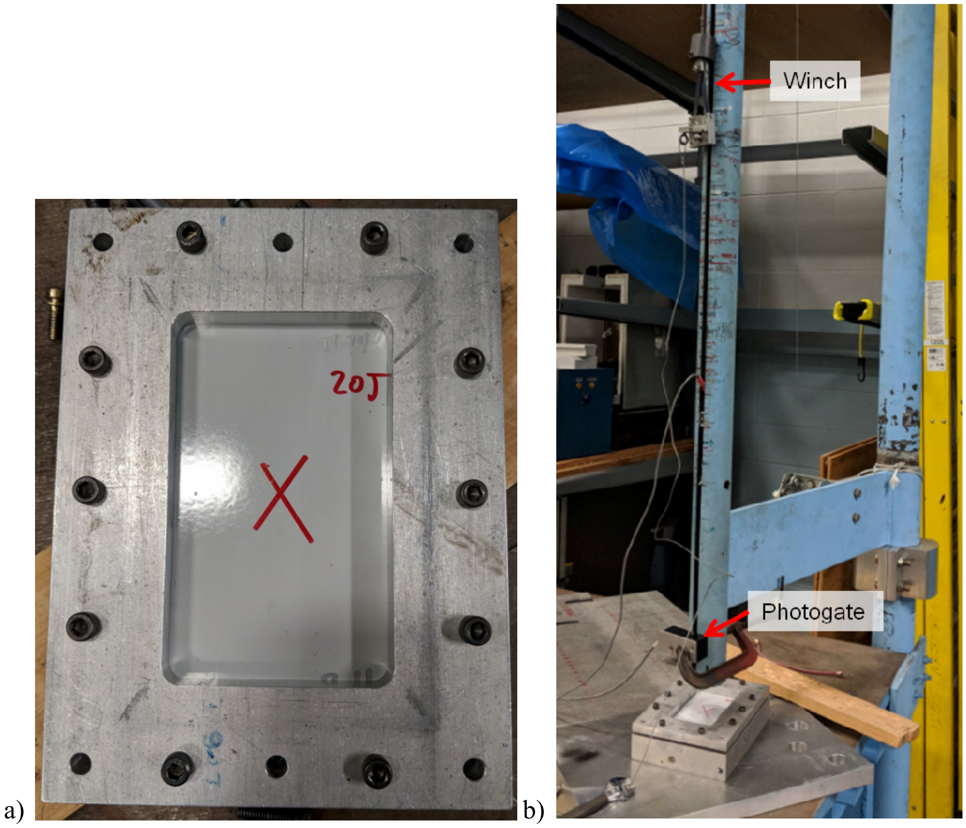

Figure 2.1. a) Flat panel impact fixture. b) Drop tower impactor setup.

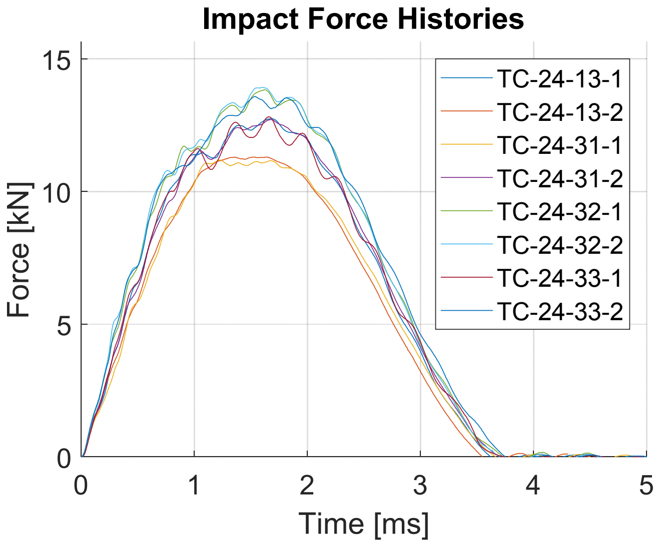

Figure 2.2. Impact force histories for all drop tower impact tests.

Table 2.1. Flat panel impact summary. Specimens with the TC-24 designation were impacted for this work and specimens with the LV- designation were previously impacted as a part of Delaney et al. [7] and were not measured for specimen thickness due to significant taper near the specimen edges.

Specimen Name	Plies	Specimen Thickness [mm]	Impact Energy [J]	Peak Impact Force [kN]	C-Scan Delam Area [mm^2]	Measured Dent Depth [mm]
TC-24-13-1	24	4.58	24.4	13.6	723	
TC-24-13-2	24	4.60	18.5	12.1	507	
TC-24-31-1	24	4.81	19.5	12.0	566	0.191
TC-24-31-2	24	4.76	24.1	13.6	634	0.229
TC-24-32-1	24	4.72	29.3	14.8	1084	
TC-24-32-2	24	4.78	29.3	14.9	1149	0.267
TC-24-33-1	24		24.1	13.7	857	0.203
TC-24-33-2	24		29.5	14.5	1546	0.241
LV-059	24	N/A	39.7	15.0	355	0.16
LV-071	16	N/A	35.5	12.6	256	0.11
LV-155	16	N/A	25.7	10.1	252	0.13
LV-162	24	N/A	48.9	16.2	509	0.16

All the impacted panels were visually inspected and found to have nearly undetectable indentations on the order of about one ply thickness (about 0.2 mm), although some specimens displayed minor surface cracking. Measured dent depth is included in Table 2.1 for some specimens. Photos of the impacted surface are shown in Figure 2.2 for a variety of conditions including normal lighting (Figure 2.2a), incident glare (Figure 2.2b), and surface cracking (Figure 2.2c). Though the damage may be detectable in the lighting conditions shown in Figure 2.2a, these impacts may not be detected by a standard visual inspection of an aircraft skin given the distance from the surface these inspections take place.

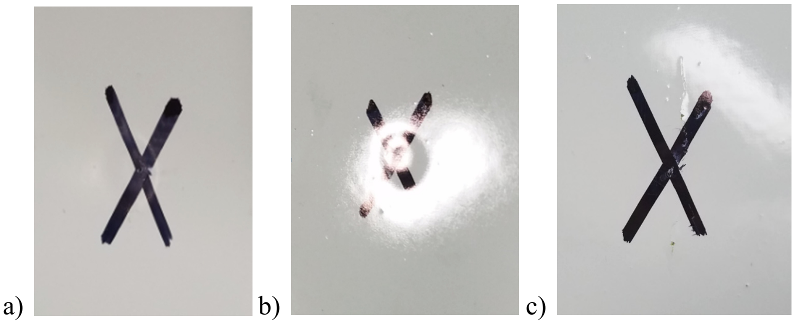

Figure 2.3. a) Impact location showing barely visible indentation in normal lighting condition. b) Impact location showing indentation highlighted by incident glare. c) Impact location showing some visible surface cracking.

2.2 Flat Panel NDE

Post impact, specimens were scanned in pulse-echo ultrasonic (UT) C-scan by the NASA Floating Ultrasonic System located at NASA Langley Research Center with a resolution of 0.508 mm per scan-line. An example time-of-flight C-scan result from this system is shown in Figure 2.3a for specimen TC-24-31-1. The experimentally observed variation in delamination area is typical for this specimen geometry and impact type [7]. Delaney [23] specimens LV-162 and LV-059 were also characterized by UT C-scan with an immersion tank PocketUT C-scan system at UCSD with a resolution of 0.254 mm per scan-line. An example time-of-flight result from this system is shown in Figure 2.3b for specimen LV-162. Further details about the UT method are given in Chapter 4.9.

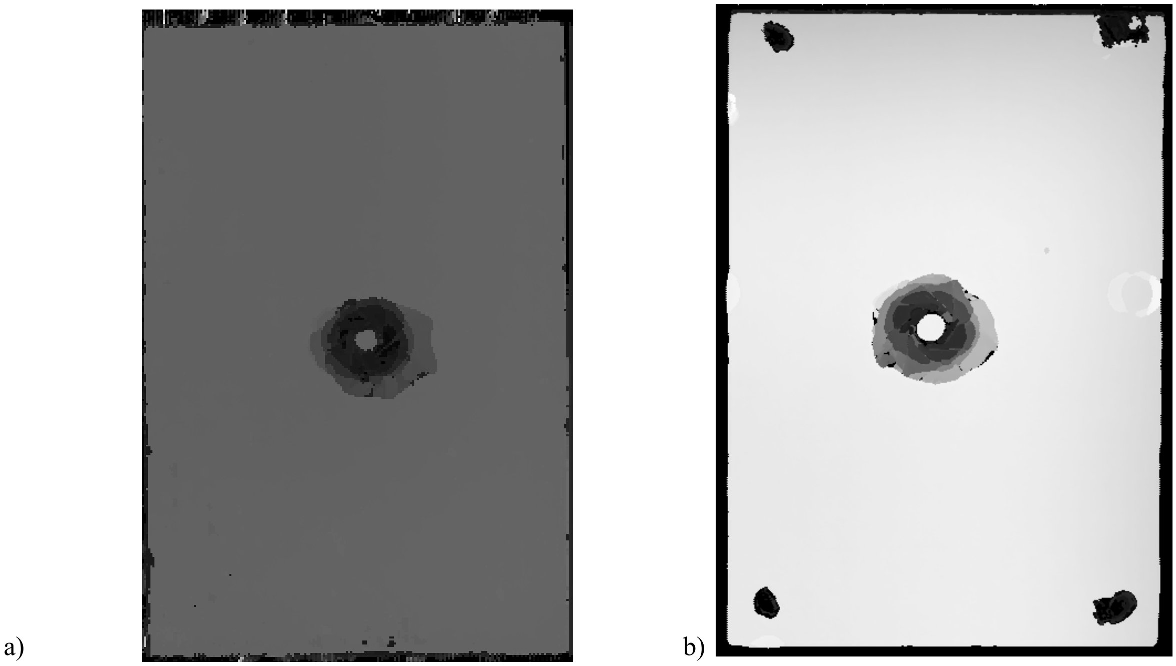

Figure 2.4. a) Time-of-flight UT results for a) specimen TC-24-31-1 and b) specimen LV-162. Overall specimen dimensions are 101.6 x 152.4 mm.

Impact damage was also characterized by X-ray computed tomography (CT). Scanning was performed with a HYTEC Inc. CT system with a Varian PaxScan 4030E detector array with an excitation voltage of 70 kV and current of 85 µA. This system is located at the NASA Langley Research Center. Scan results were reconstructed with VGStudio Max. Resulting reconstructed data sets had a voxel resolution of about 14 µm. Reconstructed 3D image data were visualized and prepared for segmentation with the open source software ImageJ [24]. Example slices of collected CT datasets are shown for specimen TC-24-31-1 in Figure 2.4. Further details about the X-ray CT method are given in Section 4.1 and scanning artifacts such as the ringing observed in the example slice in Figure 2.4 are discussed further in the Section 4.8.

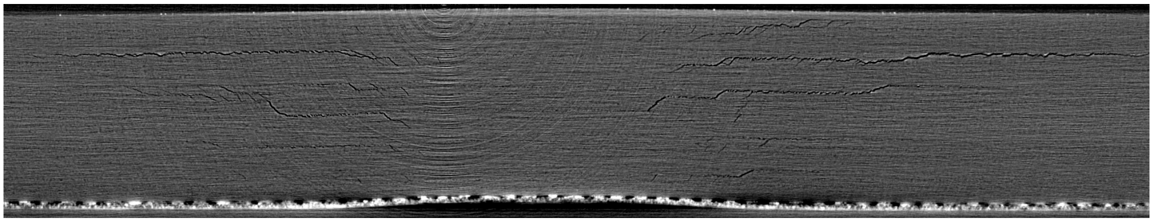

Figure 2.5. Example CT dataset slice of specimen TC-24-31-1. Primary features of interest include the horizontal delamination cracks, the angled ply cracks, the black and white fiberglass layer and the ring artifacts.

2.3 RESIDUAL STRENGTH TESTING OF FLAT PANELS

Specimens were compression after impact (CAI) tested according to ASTM D7137 [13] using a Boeing/Wyoming CAI fixture as shown in Figure 2.5. This fixture features out-of plane constrained boundary conditions on all four sides to prevent global buckling and promote compression failure due to impact damage as the failure mechanism. Compression was conducted at an end shortening rate of 0.25 mm per minute. 3D digital image correlation (DIC) images were collected for both sides of the specimen with two camera pairs for the front and back and an additional camera pair to characterize the boundary movement. Additionally four direct current deformation transducers (DCDT) measurements were taken between the loading platens to verify the crosshead displacement. The test configuration is shown in Figure 2.6.

Figure 2.6. Flat panel compression after impact test fixture.

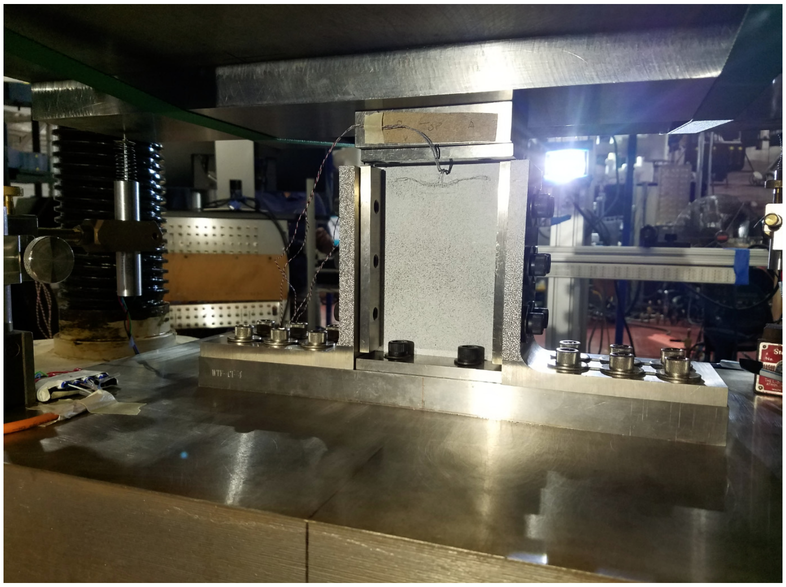

Figure 2.7. CAI test configuration.

Table 2.2. Flat panel CAI test results.

Specimen Name	Impact Energy [J]	CAI Peak Force [kN]	CAI Fail Displacement [mm]
TC-24-13-1	24.42	158	1.34
TC-24-13-2	18.53	*	*
TC-24-31-1	19.54	169	1.45
TC-24-31-2	24.13179	154	1.33
TC-24-32-1	29.4	130	1.14
TC-24-32-2	29.31	131	1.14
TC-24-33-1	24.16	137	1.73
TC-24-33-2	29.50	118	1.49
TC-24-30-1	N/A	*	*
TC-24-30-2	N/A	*	*

* refers to test failure at boundary conditions giving invalid results.

In total, ten specimens were tested with seven specimens exhibiting the desired failure mode and three experiencing failure at the loaded edges giving an invalid test result. Of the seven successful test specimens, five specimens were compressed directly to failure and two specimens were loaded and unloaded several times in an interrupted testing scheme. Interrupted testing results are discussed further in Section 252.4. Successful non-interrupted CAI tests experienced a brooming-style compression failure at the center of the specimen such as seen for specimen TC-24-31-1 in Figure 2.9. Force-displacement curves as calculated from DIC measurement of the boundary conditions and the load cell output is shown in Figure 2.10 for the successful non-interrupted testing results. The post-peak linear load-dropping behavior is likely due to the release of energy following failure leading to a displacement jump. This behavior is not indicative of actual load relaxation following failure. Peak compression load versus impact energy is shown in Figure 2.10 with a nearly linear relationship between impact energy and strength reduction for the non-interrupted test specimens. The interrupted specimens exhibited a slightly lower peak force compared to specimens of similar impact energy. This may indicate that the reloading process influenced the failure behavior.

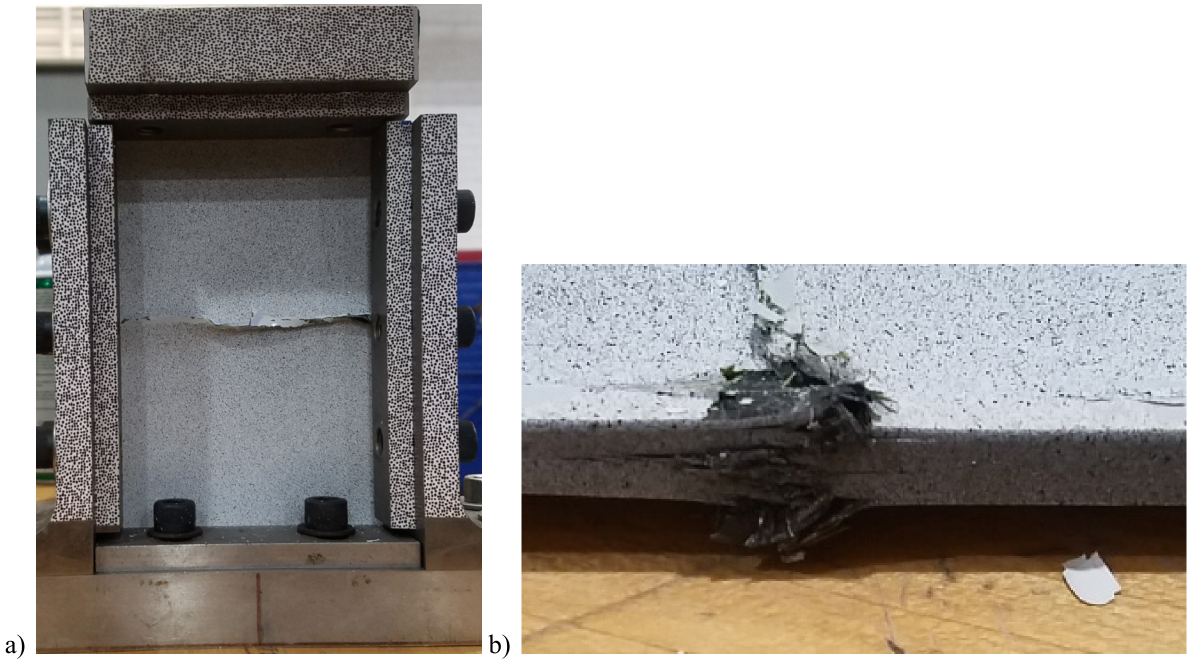

Figure 2.8. a) Specimen TC-24-31-1 in fixture post-failure. b) Image of brooming failure.

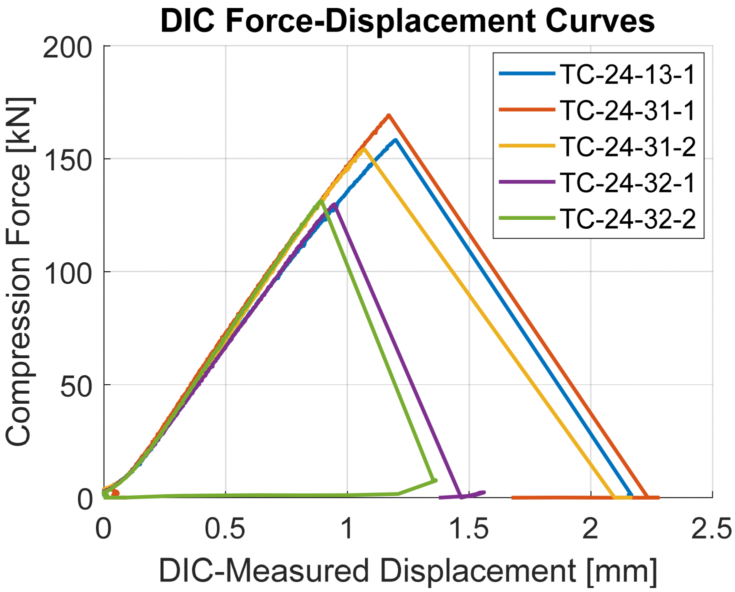

Figure 2.9. DIC based force-displacement curves for the non-interrupted successful CAI tests.

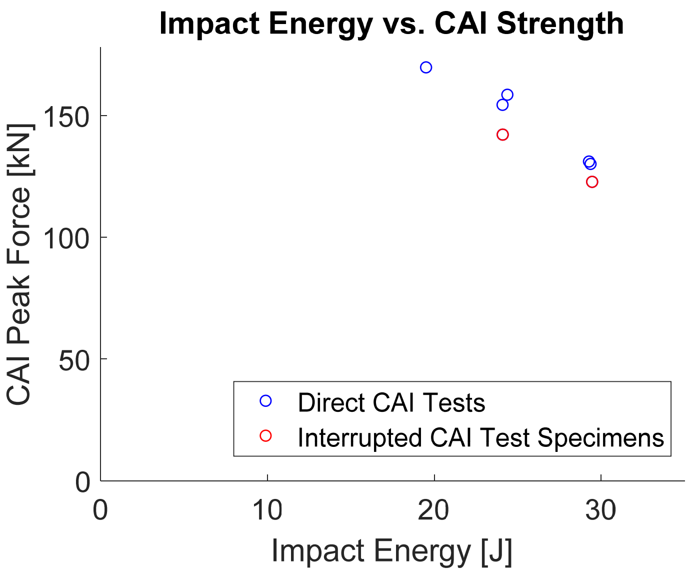

Figure 2.10. Impact force vs. residual compression strength for successful CAI tests. Interrupted test results are shown in red.

Front and back DIC results are shown for specimen TC-24-31-1 in Figure 2.12 and Figure 2.13. Displacement field results shown in Figure 2.12 show the specimen experiencing a two half-wave buckling mode with additional displacement near the impact center (Figure 2.12c). This global buckling shape was not expected, and due to the presence of a buckling node at the impact center, the interaction of the displacement field with the impact damage state may have been varied from cases involving a one half-wave buckling mode. Despite the buckling pattern, the compressive displacement field (Figure 2.12b) shows a relatively uniform compression. Lastly, the horizontal displacement field shows some slight variation in displacement caused by the buckling deformation. Strain field results (Figure 2.13) show specific strain concentrations around the impact center. Horizontal strain (ε_{xx}, Figure 2.13a) illustrates a general concentration on the front while the back/impact side shows a more concentrated strain localized around the residual indentation from the impact. Compression direction strain (ε_{yy}, Figure 2.13b) shows an equal and opposite behavior between the front and back camera systems with a strong compressive strain concentration on one side of the impact location. Additionally, the DIC characterization of the boundary condition movement is shown in Figure 2.14. This characterization of the test displacement was used to reduce the effects of machine stiffness on the measured displacement.

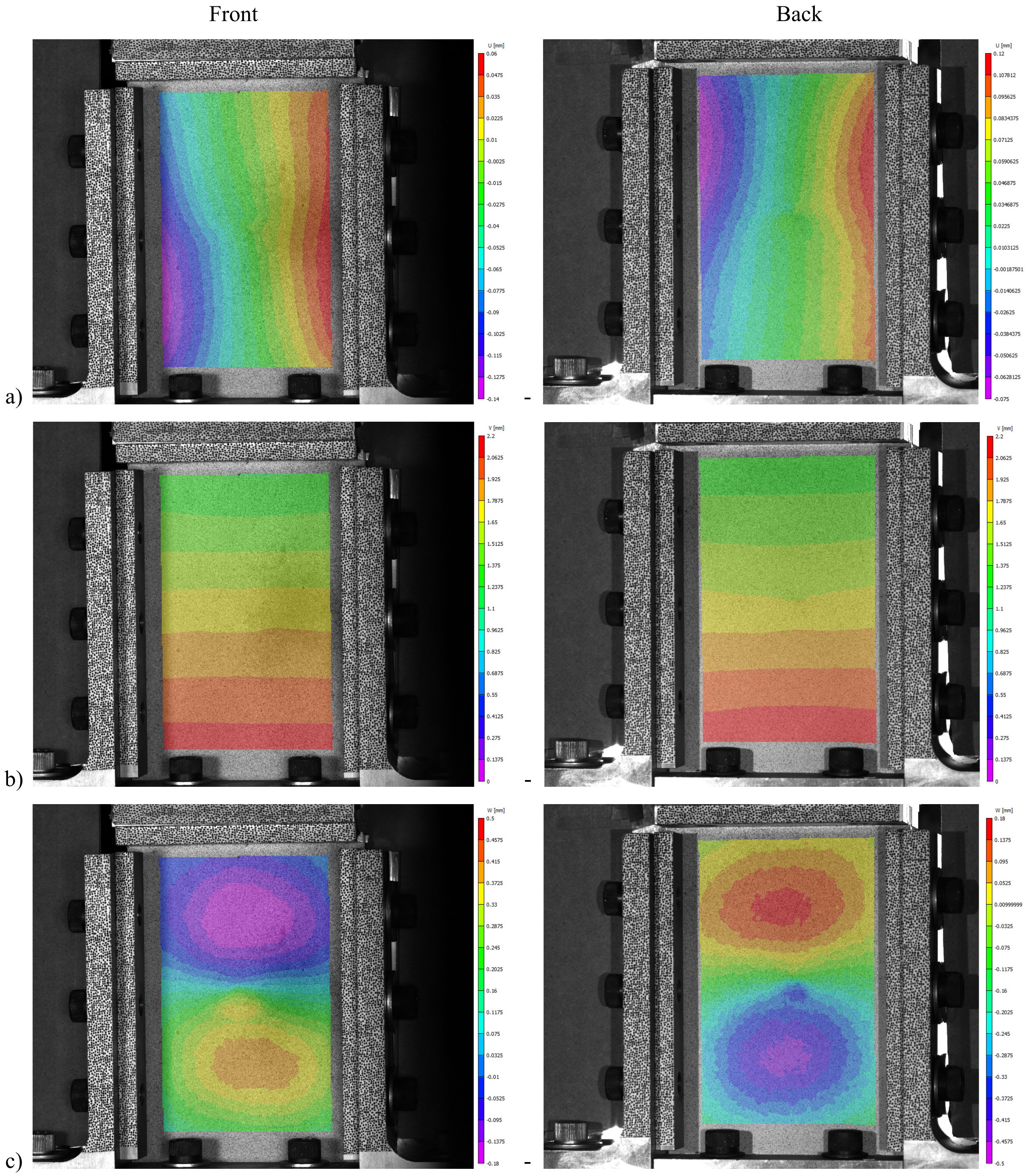

Figure 2.11. DIC displacement fields for specimen TC-24-31-1 at 5 seconds before failure. a) Horizontal displacement field. b) Vertical displacement field (compression direction) c) Out-of-plane displacement field.

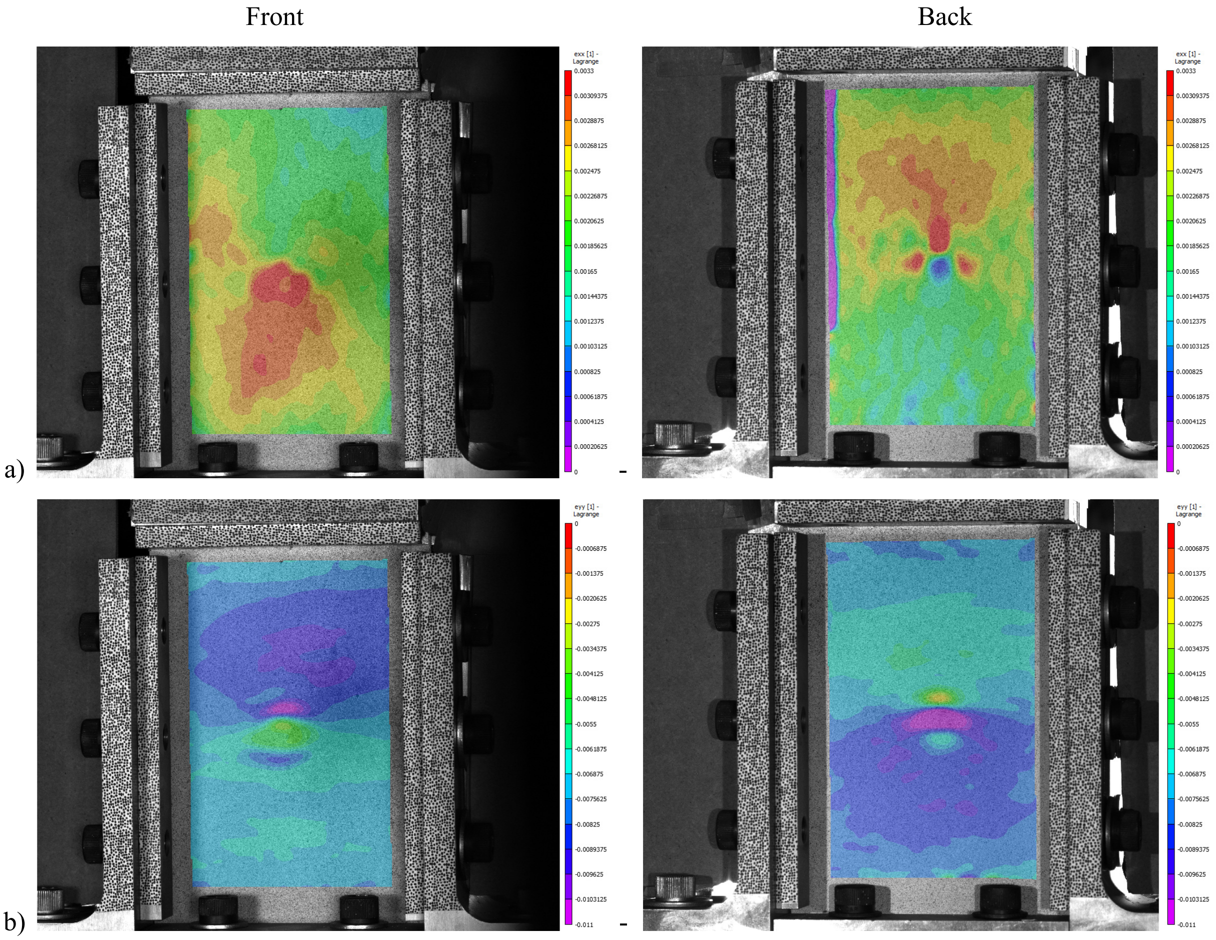

Figure 2.12. DIC strain field results for specimen TC-24-31-1 at 5 seconds before failure. a) ε_{xx} strain field (horizontal strains) b) ε_{yy} strain field (compression direction strains.

Figure 2.13. DIC characterization of displacement of loading platens.

2.4 INTERRUPTED COMPRESSION TESTING

Interrupted tests were performed for specimens TC-24-33-1 and TC-24-33-2 to observe potential progression of the damage state in subsequent CT scans. Tests were interrupted according to either audible cracking from the specimen or upon reaching designated force thresholds. Interrupted test force-histories are shown in Figure 2.15. The two interrupted test sets are summarized in Table 2.3. Interrupted testing showed no significant differences in force displacement behavior between runs indicating that there was either no damage progression or that the damage progression did not impact the specimen stiffness between runs.

After each run, specimens were CT scanned. For specimen TC-24-33-1, the only observed progression of the impact damage state between all runs was the development of fiber breakage associated with a series of matrix cracks as shown in Figure 2.16. This series of closely spaced matrix cracks may have lead to buckling of thin strips of fibers and ultimately fiber breakage in these zones. Due to some of the resolution limitations of CT scanning in capturing the edges of delaminations, it is possible that delamination progression had occurred between subsequent loading without easy detection by CT. Some of the limitations of CT scanning as a damage characterization method are discussed in Section 4.3.

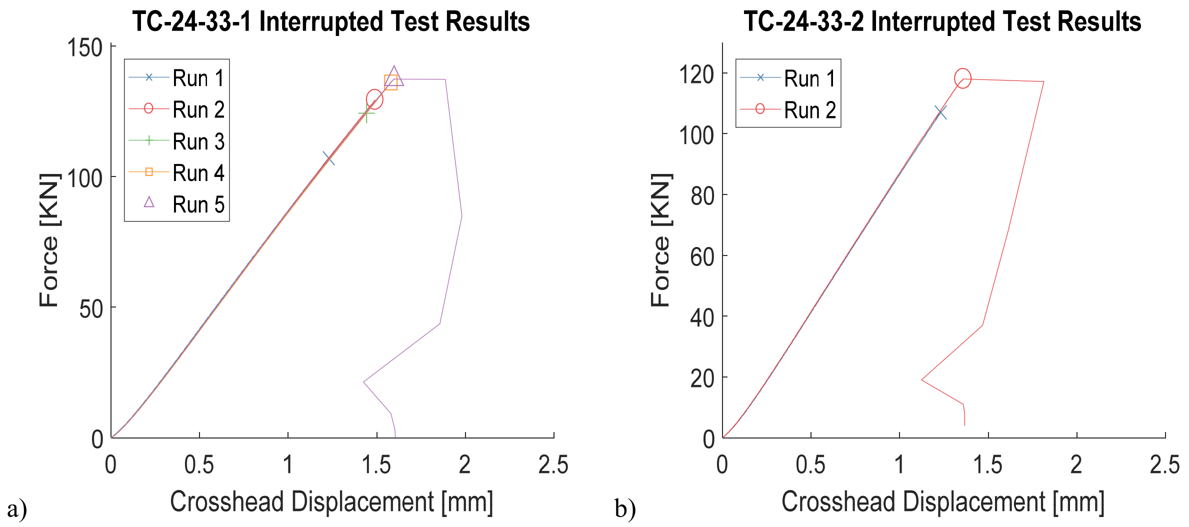

Figure 2.14. Interrupted testing force-history curves for a) specimen TC-24-33-1 and b) specimen TC-24-33-2. Plotting symbols indicate the peak load reached in each test run.

Table 2.3. Flat panel interrupted testing summary.

Test Specimen	Run Number	Peak Load [kN]	Peak Displacement [mm]
TC-24-33-1	1	107.05	1.229
	2	129.40	1.491
	3	124.28	1.443
	4	136.05	1.580
	5	137.38	1.598
TC-24-33-2	1	106.97	1.232
	2	117.97	1.359

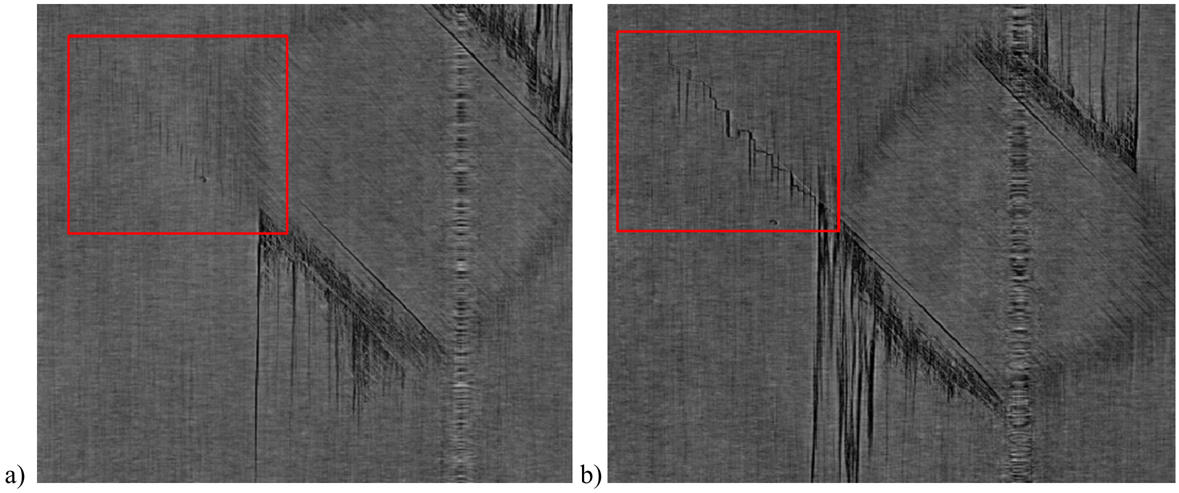

Figure 2.15. CT scan slices for specimen TC-24-33-1 after interrupted test a) run 1 and b) run 4. The major progression of a series matrix cracks into fiber breakage is highlighted.

Specimen TC-24-33-1 was CT scanned post CAI failure, but due to the complexity of the observed failure mode, only this specimen was scanned as the failed CT scans were considered difficult to interpret. An example slice showing the brooming failure mode is shown in Figure 2.16. The failure mode consists of groupings of several plies pushed into other groupings. Also, the importance of matrix cracking can be observed as several plies are split into different groupings at matrix cracking locations. These ply groupings appear to slide past each other, propping open the adjacent delaminations and creating the observed brooming behavior. This suggests that the frictional forces on the compressed matrix crack faces may be important in governing the stability of the impact damage zone.

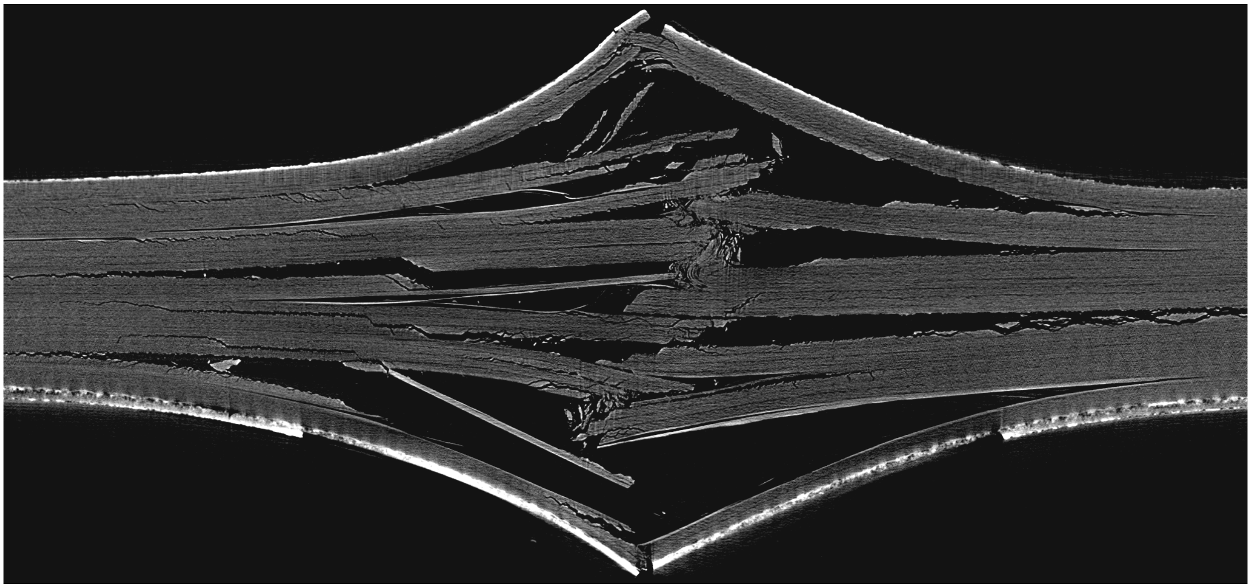

Figure 2.16. Example CT slice from CAI tested specimen TC-24-33-1.

2.5 UNSUCCESSFUL COMPRESSION TESTS

Some CAI tested specimens failed in a non-valid failure mode for CAI testing. The two pristine specimens failed at the top edge of the specimen due to buckling of the specimen and rotation at the top piece of the fixture. Edge failure is shown for the pristine specimen TC-24-30-1 in Figure 2.7a. This failure mode is likely caused by buckling before reaching the net section undamaged strength and then failure at the boundary conditions. Because of this failure mode, these tests are not considered valid CAI tests and there is a lack of un-damaged test results for comparison with the impacted tests. Additionally, specimen TC-24-13-2 (18.5 J impact) and LV-162 (Mac Delaney 48.9 J impact) also experienced edge failure instead of the desired compression failure mode. Specimen TC-24-13-2 edge failure is shown in Figure 2.7b. Specimen TC-24-13-2 may have experienced edge failure due to slipping of the supports of the compression fixture which led buckling, or the impact damage created at the relatively low impact energy for this specimen may not have been significant enough to drive the desired CAI failure mode. Specimen LV-162 from Mac Delaney's impact experiments failed at the boundaries primarily due to excess tapering of the specimen which led to non-uniform compression loading. An image of the failed edge of LV-162 is shown in Figure 2.8. This specimen was included in the tests because of the high-quality X-ray CT datasets associated with this specimen.

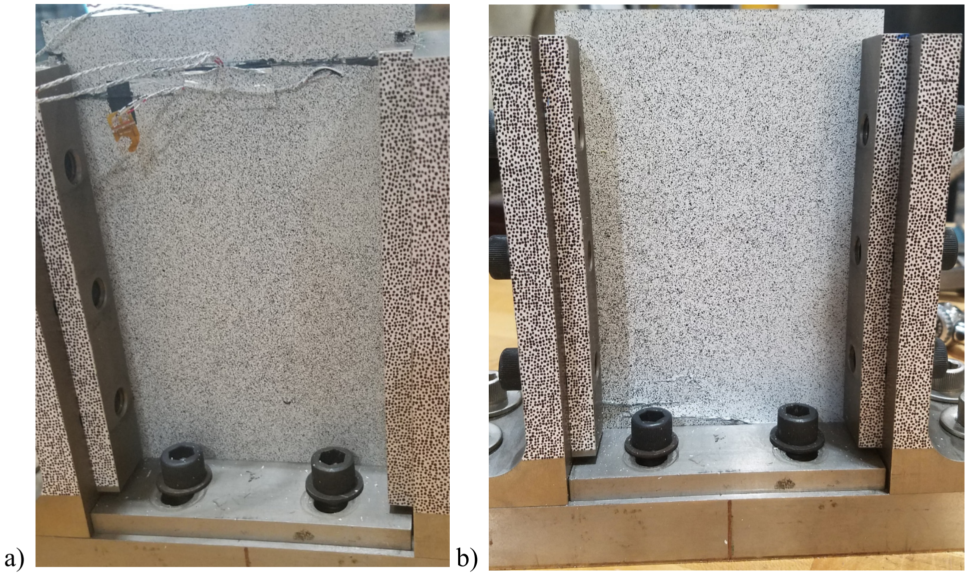

Figure 2.17. Failure of non-impacted TC-24-30-1 specimen. The failure was primarily edge-driven and lead to no significant damage in the central region.

Figure 2.18. Edge failure of specimen LV-162.

3 STIFFENED PANEL EXPERIMENTS AND NDE

This chapter presents the experimental impacts and residual strength testing of stringer stiffened composite panels. The experimental program was divided into three components: impact testing, non-destructive damage characterization, and residual strength compression testing. Additionally, stringer impact cases were split into two categories, direct stringer cap impact and skin-side flange impact. Example NDE scan results for these specimens are shown in this chapter, and further analysis of these results will be given in Chapter 4.

Experimental work presented in this chapter was conducted in collaboration with Hyungsuk Eric Kim. Design, manufacture, impact, and preparation for residual strength testing were conducted with an equal contribution.

3.1 STIFFENED PANEL IMPACT TESTING

Two CFRP omega hat stringer stiffened composite panels were manufactured with T800S/3900-2B unidirectional prepreg and a layup of $[45/-45/0/45/90/-45/0/90]_s$ in both the stringer and skin with an additional 90° ply on the skin in the region underneath the stringer and the 0° axis running parallel to the stringer. Panels were manufactured as 5 stringer panels with a spacing of 260 mm between stringers and overall panel dimensions of 990 x 1310 mm as shown in Figure 3.1a. A more detailed sketch of the stringer and skin geometry is shown in Figure 3.1b with the 0° direction coming out of the page.

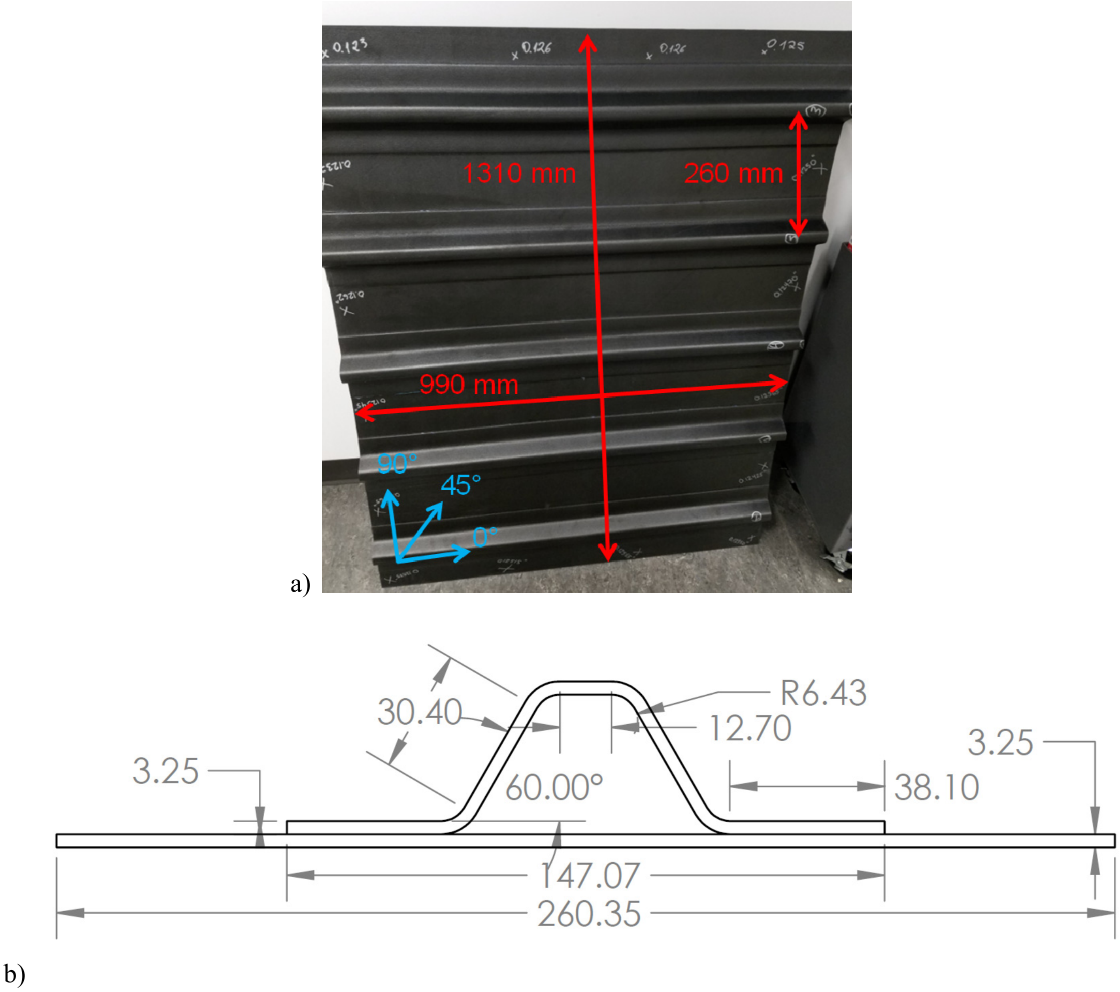

Figure 3.1. a) As manufactured five-stringer panel showing major dimensions and fiber orientation. b) Stringer and skin nominal geometry. Units are shown in millimeters. 0° fiber orientation is out of the page.

Two types of impacts were conducted on the stringer specimens, stringer cap impacts and skin-side mid-flange impacts at center of the flange as illustrated in Figure 3.2. The cap impact location was chosen to simulate internal damage events during maintenance or manufacture and cap-type specimens were designed to study strength-specific failure of a single stringer specimen. The flange impact location was chosen to simulate external damage during maintenance or tool drop and the flange-type specimens were designed to emphasize the effect of impact damage on the post-buckling behavior of the single stringer specimen. Impacts were conducted with a pendulum impactor with a 25.4 mm radius metal tip and a total mass of 5.14 kg. Desired impact energies were selected by calculating the required pendulum angle to create the desired energy at the bottom point of the pendulum swing at the point of impact. The velocity of the impactor at the time of impact and during the rebound was measured by laser photogate, and the force-history of the impact was measured by a load cell within the pendulum impactor. The velocity and mass of the impactor were then used to calculate the actual impact energy.

Impact support fixtures were designed to directly support the impacted stringers depending on the impact type as shown in Figure 3.3. Due to the curvature of the stringer caps, only the relatively flat surfaces on the stringer flange, web, and crown were in contact with the fixture. It is also important to note that for the cap impact case, the hollow interior of the specimen cap may have reduced the effective fixity of the boundary conditions. The flange type impact supports were designed to support the impacted stringer and an adjacent stringer to better simulate an impact condition in a multi-stringer structure and prevent the skin from behaving as a free-edge.

For stringer cap impacts, the span between the supports was set as 304.8 mm. The pendulum impactor setup for the cap type impacts is shown in Figure 3.4a. For stringer flange impacts the span between the supports was set at 457.2 mm. The pendulum impactor setup for the flange impacts is shown in Figure 3.4b. Cap impacts were conducted at three different energy levels, a low energy at an average of 28.5 J, a mid energy at an average of 47.5 J, and a high energy at an average of 66.0 J and flange impacts were conducted at two different energy levels, a mid energy at an average of 64.8 J and a high energy at an average of 83.5 J. A total of 12 cap-type and 4 flange type impacts were conducted. A summary of the conducted impacts is given in Table 3.1. Impact force histories are shown in Figure 3.5a for cap impacts and in Figure 3.5b for flange impacts. Cap impacts show a first load drop around 6 kN and the 66 J impact cases show a second load drop near the peak impact force (around 10 kN).

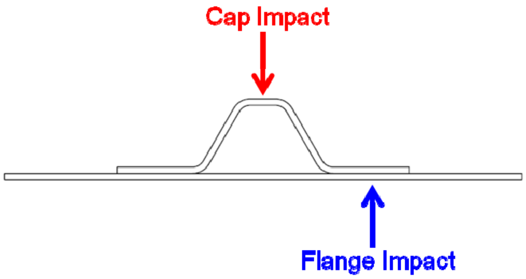

Figure 3.2. Impact types and locations for stringer panel.

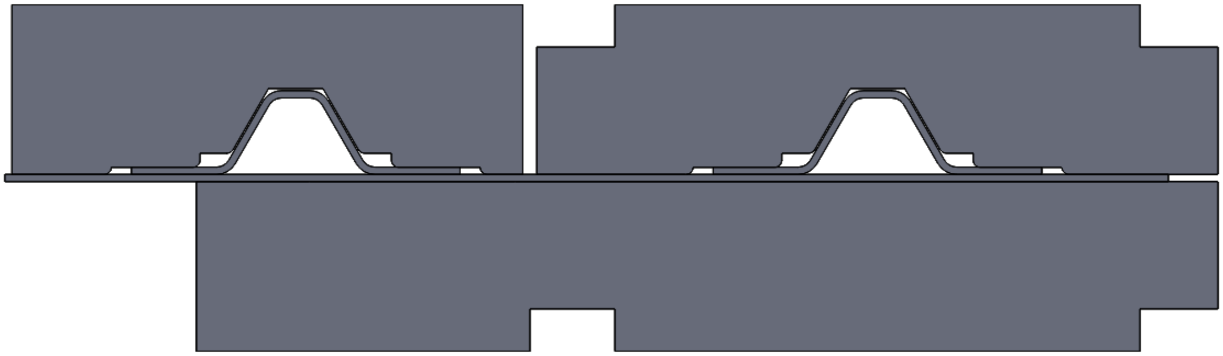

Figure 3.3. Fixture setup rendering. Two adjacent stringers are supported during flange-type impacts to prevent the mid-bay skin from acting as a free edge.

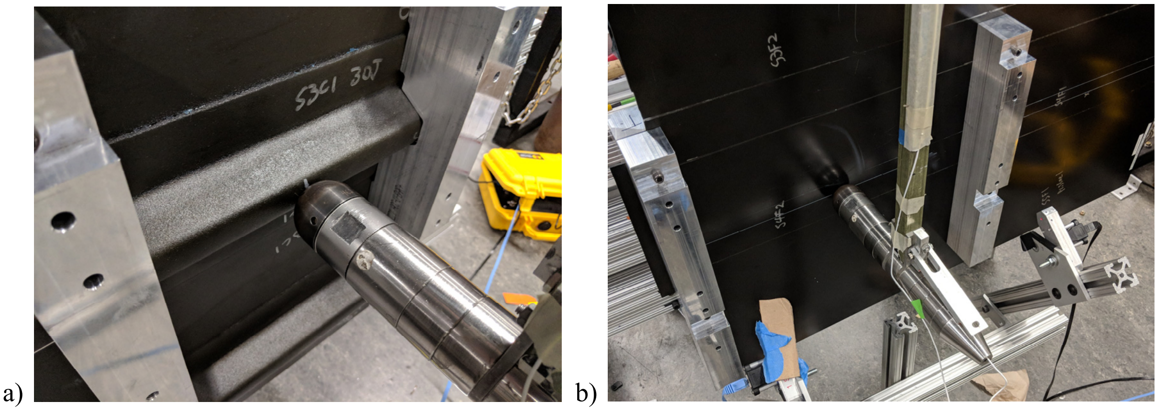

Figure 3.4. a) Pendulum impactor setup for cap impact. b) Pendulum impactor setup for flange impact.

Table 3.1. Stringer stiffened panel impact summary. Dent depth was only measured for cap-impacted compression specimens.

	Impact Name	Impact Type	Predicted KE [J]	Actual KE [J]	Inbound V [m/s]	Peak Force [kN]	Est. Damage Length [mm]	Dent Depth [mm]
Panel 1	P1SSC1	Cap	50	47.30	4.29	10.54	88.9	
	P1SSC2	Cap	30	28.85	3.35	8.40	76.2	
	P1SSC3	Cap	70	66.50	5.09	10.89	98.4	0.305
	P1S2C1	Cap	30	28.36	3.32	8.30	77.0	
	P1S2C2	Cap	50	47.58	4.30	10.71	81.0	0.457
	P1S2C3	Cap	70	65.72	5.06	11.75	88.0	
	P1S3C1	Cap	30	28.49	3.33	8.24	78.0	
	P1S3C2	Cap	50	47.58	4.30	10.56	96.0	
	P1S3C3	Cap	70	65.87	5.07	11.48	97.0	
	P1S1C3	Cap	30	28.41	3.33	8.16	68.0	
	P1S4C3	Cap	50	47.11	4.28	10.63	96.0	0.381
	P1S4C2	Cap	70	66.65	5.09	11.35	92.0	0.330
Panel 2	P2S3F1	Flange	90	84.48	5.74	16.06	88.90	
	P2S3F2	Flange	90	82.72	5.68	15.92	108.0	
	P2S4F1	Flange	70	64.81	5.02	14.73	110.2	
	P2S4F2	Flange	70	64.81	5.02	14.36	92.1	

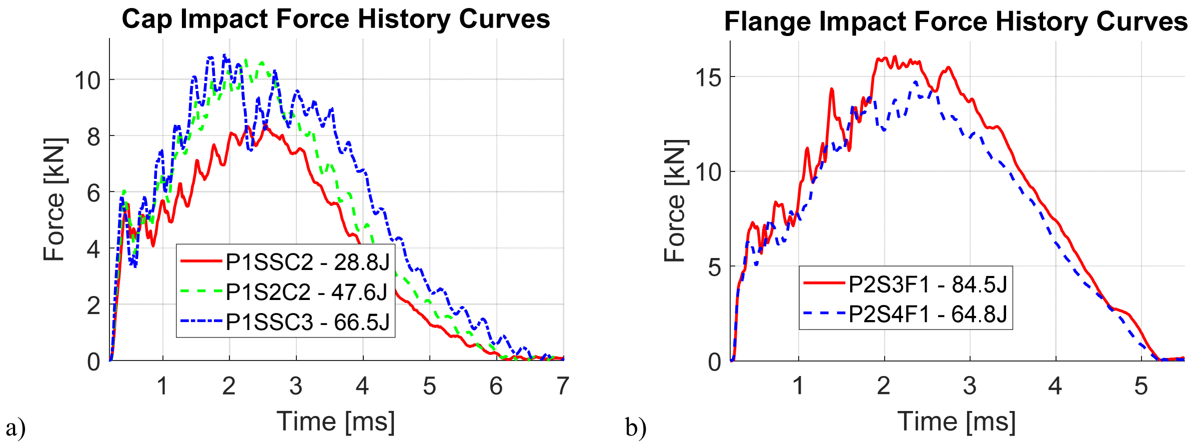

Figure 3.5. a) Example impact force histories for the three cap impact energy levels. b) Example impact force histories for the two flange impact energy levels

3.2 STIFFENED PANEL NDE

After impact, handheld A-scan mapping was performed to capture the approximate damage area such as shown for cap type impacts in Figure 3.6 and Figure 3.7 and flange type impacts in Figure 3.8. Damage length as approximated from these A-scans is given in Table 3.1. Figure 3.8 shows the impact damage for the three cap impact energy levels (~28, 47, 66 J). Impact damage for the 28 J case (Figure 3.6a) is contained within the stringer crown region, with a small amount of damage in the radius region. Impact damage for the 47 J case (Figure 3.6b) shows a similar shape for this specimen (S4C3) with damage in the crown and radius, and with somewhat more significant radius damage. However, for the 47 J case, some asymmetry of the damage state has been observed in other specimens (S2C2 and S3C2) as shown in Figure 3.7 for specimen S2C2. Figure 3.7a shows the side of the cap with damage traveling into the web and Figure 3.7b shows the side of the cap with damage contained by the radius. This asymmetry may have been caused by slight misalignment of the impact location, skewed towards one web. Impact damage for the 66 J case (Figure 3.8c) shows damage traveling down the web on both sides of the stringer cap. This damage in the stringer web has been observed as a band of fiber breakage in most plies and some delamination, and this damage is likely associated with the second load drop event observed in the 66 J impact force-histories. Flange damage for both energy levels (Figure 3.8) show a roughly trapezoidal shape where the wider base of the trapezoid is at the end of the stringer flange and the thinner base is near the inside of the stringer.

Figure 3.6. Handheld A-scan measurement of impact damage extent for cap impact case. a) Specimen S3C1, 28.5 J impact case. b) Specimen S4C3, 47.1 J impact case. c) Specimen S4C2, 66.7 J impact case.

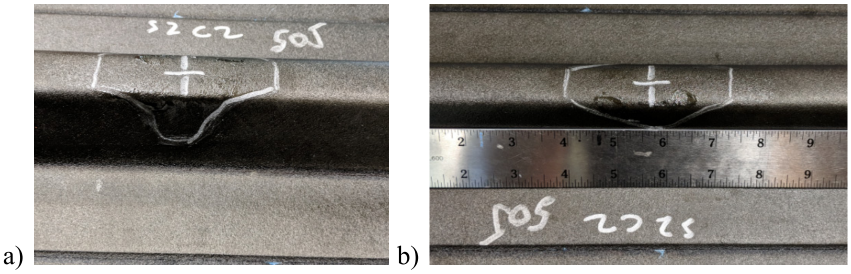

Figure 3.7. Specimen S2C2 (47 J impact case) A-scan results showing asymmetry of impact damage area. a) Side showing damage traveling into the stringer web. b) Side showing damage contained within the cap radius.

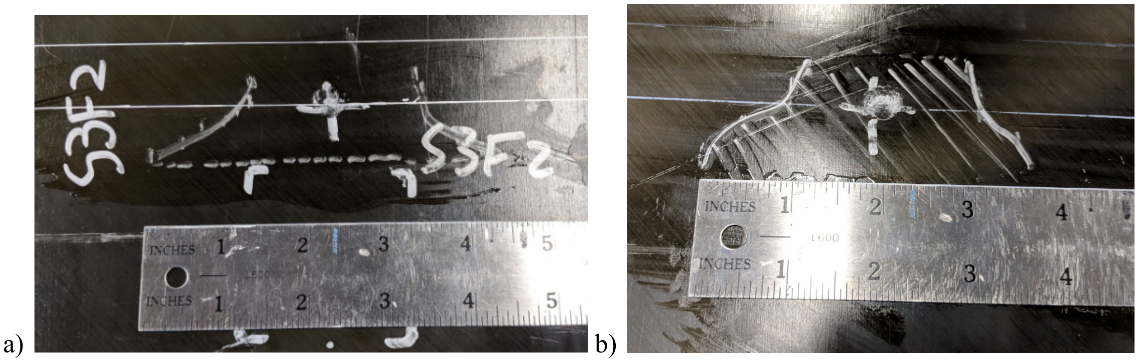

Figure 3.8. Handheld A-scan measurement of impact damage extent for flange impact case. a) Specimen S3F2, 82.7 J impact case. b) Specimen S4F2, 64.8 J impact case.

Specimens were then characterized by CT and UT C-scan. Pulse-echo UT C-scan was performed with the NASA Floating Ultrasonic System located at NASA Langley with a resolution of 0.254 mm per scan-line. Cap impacted specimens were difficult to characterize with UT scanning due to the curvature of the stringer so only part of the damage contained in the crown was captured with the scan providing no results at the radius or web regions as shown in Figure 3.9. Flange impacted specimens were easier to characterize in UT C-scan due to the flat skin and flange. Scans were taken from the skin side (example in Figure 3.10a) and from the flange side (example in Figure 3.10b). Skin side scans capture the major disbond between the skin and stringer as trapezoidal and observe damage in the skin and flange laminates as a roughly circular shape, whereas flange side scans capture major delamination damage in the flange laminate and some amount of disbond between the skin and stringer flange. Further discussion of UT results can be found in Chapter 4.9.

Figure 3.9. Example UT C-scan for cap impacted specimen S4C3 (47.1 J). Scanning captures the damage length but otherwise fails to capture many of the primary damage features due to curvature.

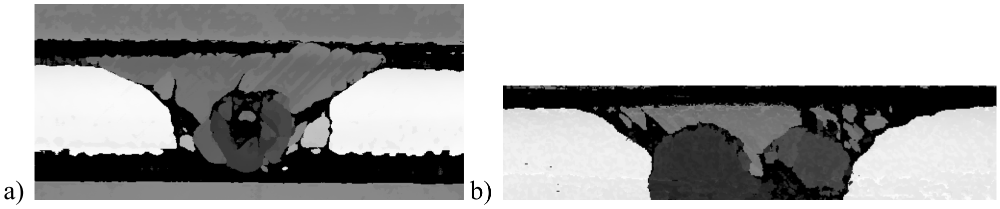

Figure 3.10. UT C-scan time-of-flight images for specimen S3F1 (84.5 J impact). a) Skin-side scan, b) Flange side scan.

CT scanning was performed with a North Star Imaging X3000 computed tomography system with a source voltage of 140 kV and current of 140 μA. Cap impacts were scanned with a resulting resolution of 32.4 μm per voxel ("volume pixel", 3D pixel), but due to the resolution/scan area trade-off inherent to CT scanning the full damage area was not captured in each scan. Example CT slices for specimen S4C3 and specimen S4C2 are shown in Figure 3.11. CT results show the internal damage state as a complex network of delaminations and ply cracking. In both example slices damage is more severe in the cap radius region with some fiber damage features visible, whereas in the crown region the damage consists primarily of delaminations and matrix cracking. A more in depth discussion of the CT results will be given in Chapter 4.1. Flange impact specimens were more difficult to scan due to their larger geometry which complicated the CT scan process. Because of the compression test preparation and potting, the overall effective compression specimen width was ~14", which prevented scanning at high resolution. An example CT slice from the compression specimen S3F1 is shown in Figure 3.12a. To characterize the flange impact damage a separate non-compression testing specimen (S4F1) was cut to fit within the scanner with a resulting resolution of 17 μm per voxel as shown in Figure 3.12b. This scan shows the major delamination between the skin and stringer flange near the center of the laminate. Further discussion of these CT scan results can be found in Chapter 4.14.

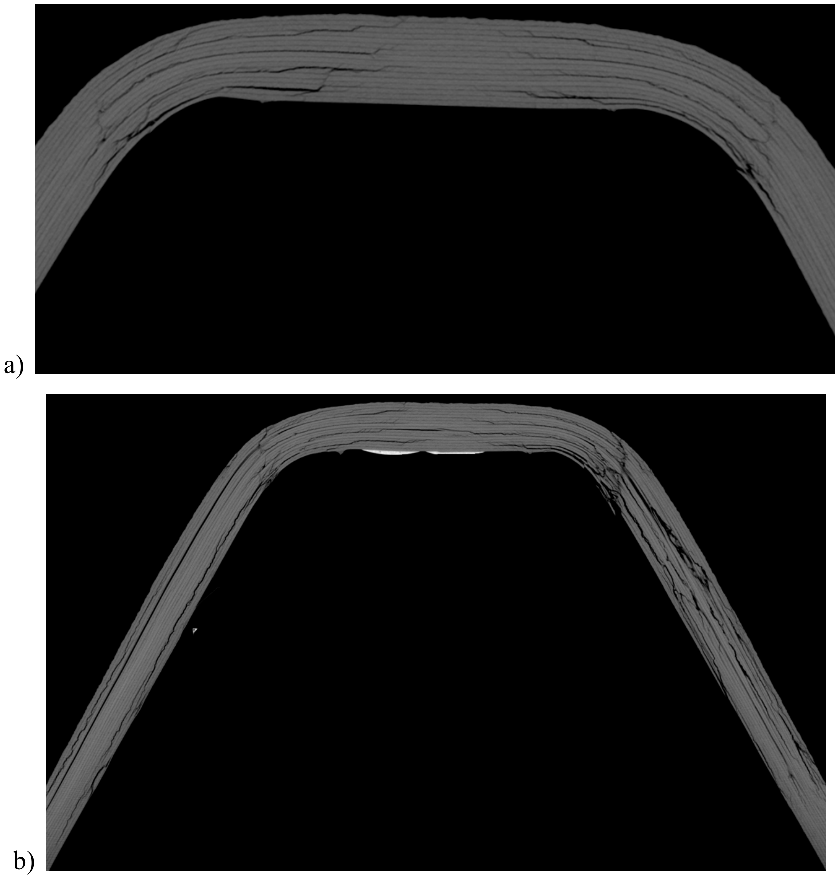

Figure 3.11. Example CT slices for a) specimen S4C3 (47.1 J impact) and b) specimen S4C2 (66.7 J impact). Damage is severe in the radius for both cases and extends into the web for the 66.7 J impact case.

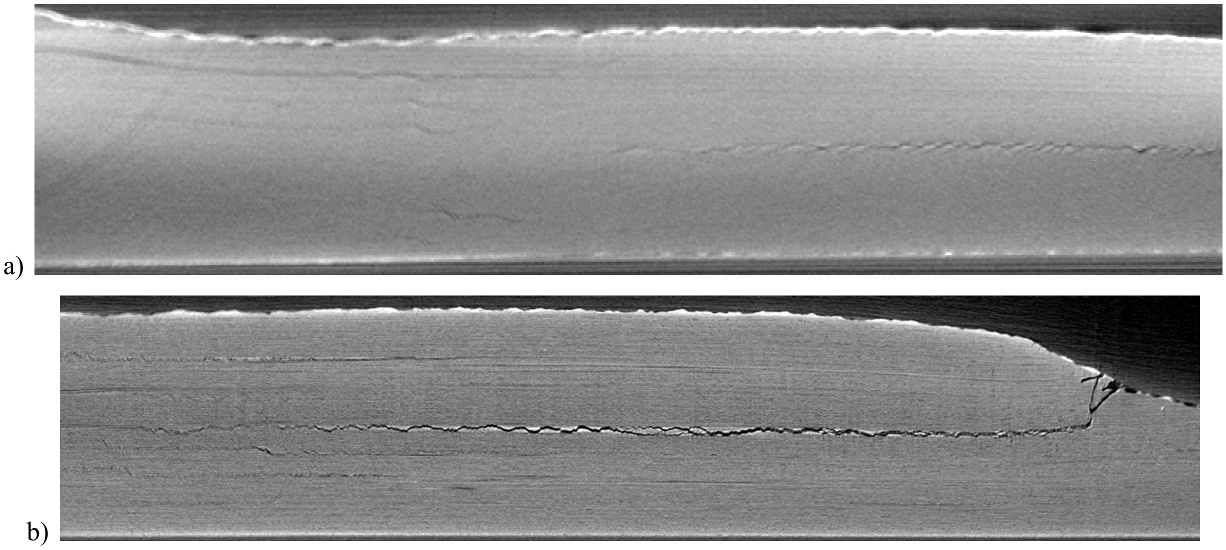

Figure 3.12. Example CT slice of a) residual strength specimen S3F1 and b) cutout specimen S4F1.

3.3 STRINGER PANEL COMPRESSION TESTING SUMMARY

Post impact, select specimens were cut out of the larger panels to prepare them for residual strength testing. Specimens were prepared for residual strength compression testing according to the type of impact to emphasize different structural behaviors. Example compression specimens are shown in Figure 3.13 and compression specimen designs are shown in Figure 3.14. Flange-impacted specimens were cut to 251 x 484 mm as shown with skin extending from underneath the stringer by about 50 mm on each side as shown in Figure 3.14a. This configuration was chosen to emphasize post-buckling driven failure of the stringer panel and to select a three half wave mode, as shown in Figure 3.14a, that would be highly interactive with the damage state created by mid-flange impact. Cap-impacted specimens were cut to 162 x 292 mm with only a small amount of skin extending beyond the stringer as shown in Figure 3.14b. This configuration was chosen to emphasize a stiffener strength failure mode that was highly interactive with the types of laminate damage created by a direct stiffener impact. Specimens were then potted in an aluminum filled epoxy (EpoxACast 655) encased in a steel frame of about 32 mm depth on each end to prevent local failure at the compressed ends. In total 6 cap specimens (S4C3, S2C2, SSC3, S4C2, S4PC1, S1PC2) and 4 flange specimens (S3F1, S3F2, S4F2, S5PF1) were prepared for residual strength testing.

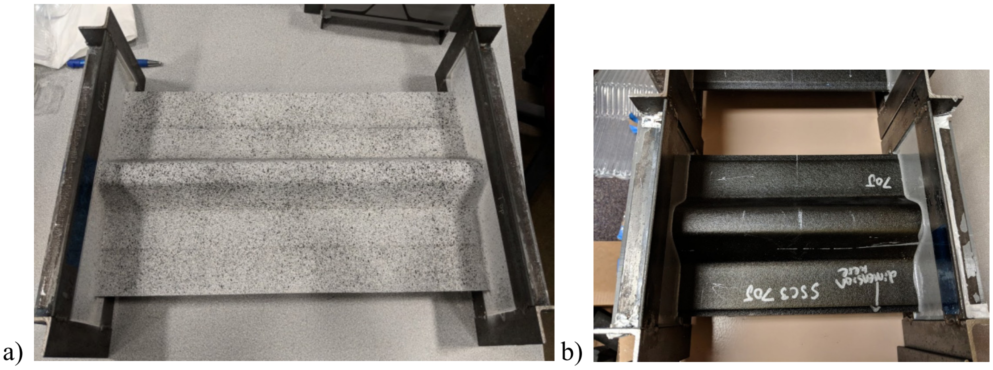

Figure 3.13. a) End-potted flange-impact type compression specimen. b) End-potted and trimmed cap-impact type compression specimen.

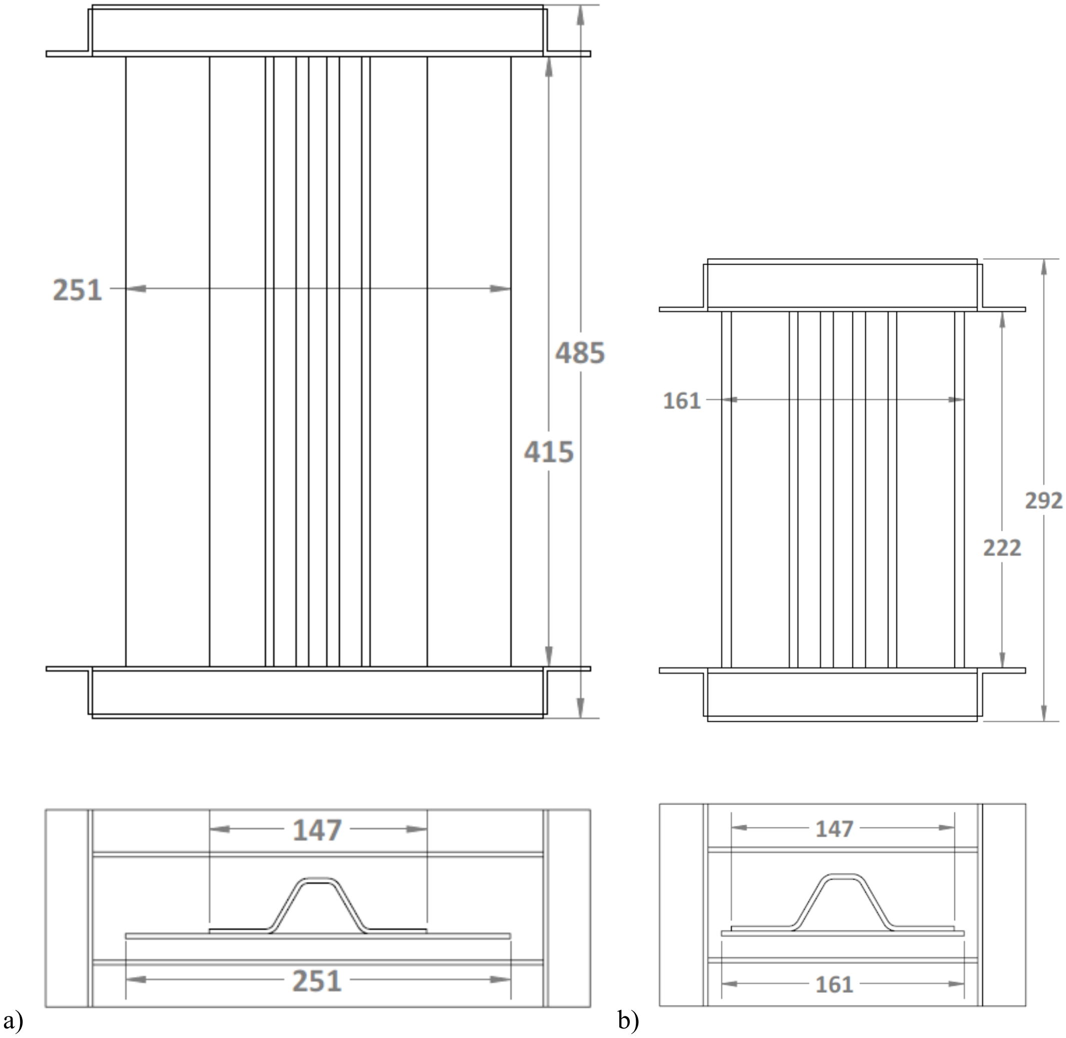

Figure 3.14. Compression specimen design. a) Flange-impacted compression specimen and b) cap-impacted compression specimen

3.4 CAP-TYPE COMPRESSION TESTING

The cap type compression setup is shown in Figure 3.14. Specimens were compression tested at an end-displacement rate of 1 mm/min. Four of the cap specimens, the two pristine specimens and one 47 and 66 J impacted specimen each, were compressively loaded quasi-statically to failure. The other two specimens were loaded initially to the first damage event and then removed from the test for NDE inspection of the first failure mode. DIC was performed for the four non-interrupted cap specimen tests and the first round of the interrupted tests with 3 camera pairs. Two of these camera pairs were placed at roughly 45° angles to capture different sides of the stringer cap. The two interrupted test specimens were then loaded to final failure with only one camera pair for the front and back each. Compression after impact test results are summarized in Table 3.2.

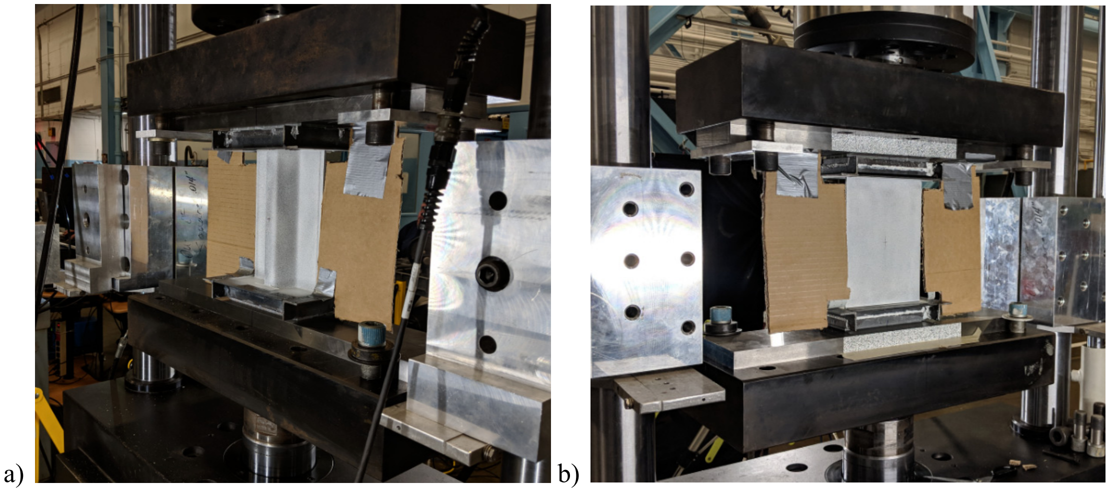

Figure 3.15. Cap-type specimen compression test setup from a) stringer-side, b) skin-side.

Table 3.2. Compression testing results summary.

Test ID	Impact Energy [J]	Peak Load [kN]	Failure Displacement [mm]
S2C2	47.58	205.15	1.670
S4C3-run1	47.11	216.63	1.462
S4C3-run2	47.11	201.98	1.704
SSC3	66.50	203.68	1.622
S4C2-run1	66.65	112.81	0.807
S4C2-run2	66.65	210.21	1.719
S4PC1	N/A	459.75	3.389
S1PC2	N/A	478.35	3.647

Residual strength test force vs. displacement results are shown for all tests in Figure 3.15. Overall, the cap impacted specimens showed a significant decrease in final compressive strength relative to the non-impacted specimens, around a ~55% reduction. Additionally, all impacted specimens experienced a first major load drop that corresponded with visible failure of the stringer cap with sustained stable loading until final total stringer failure. The forces at which this initial cap failure occurred are given with respect to the impact energy in Figure 3.16. As expected, higher impact energy corresponds with lower onset force, but there is some discrepancy observed between specimen S2C2 and S4C3 despite having very similar impact energies. This is likely due to the asymmetrical damage formation as illustrated in Figure 3.7 where damage migrated down the stringer web on one side of the cap. This feature will be discussed further when presenting the DIC results for this case. The final failure event for the impacted specimens consisted of total stringer compression failure and disbonding from the skin, with the skin suddenly buckling away from the stringer.

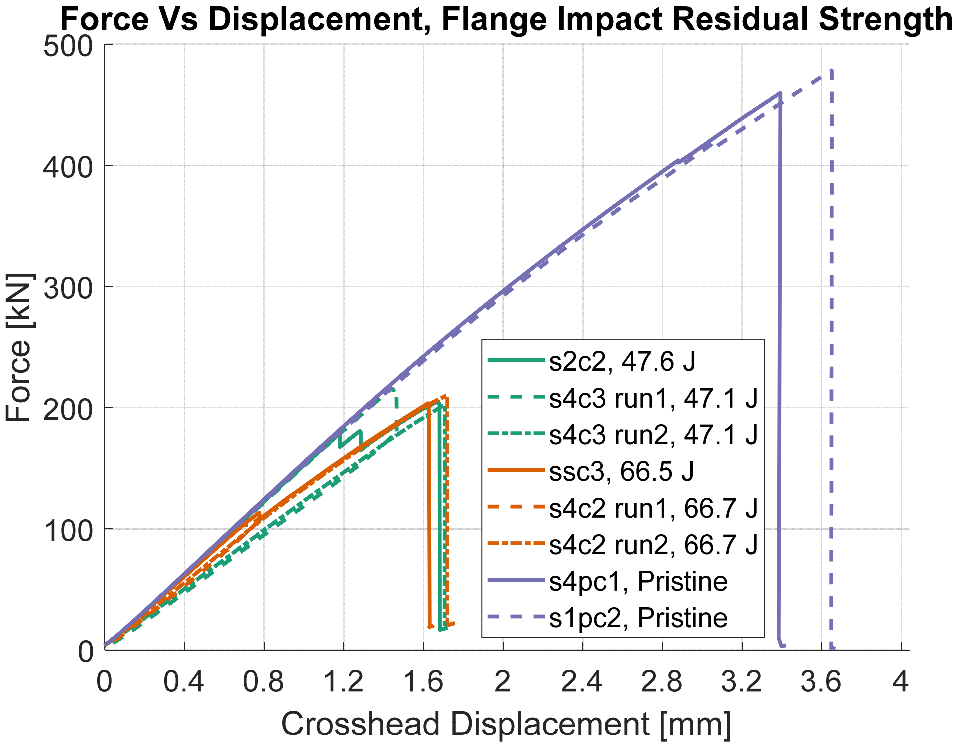

Figure 3.16. Residual strength force-displacement for all cap specimens color coded by impact energy level.

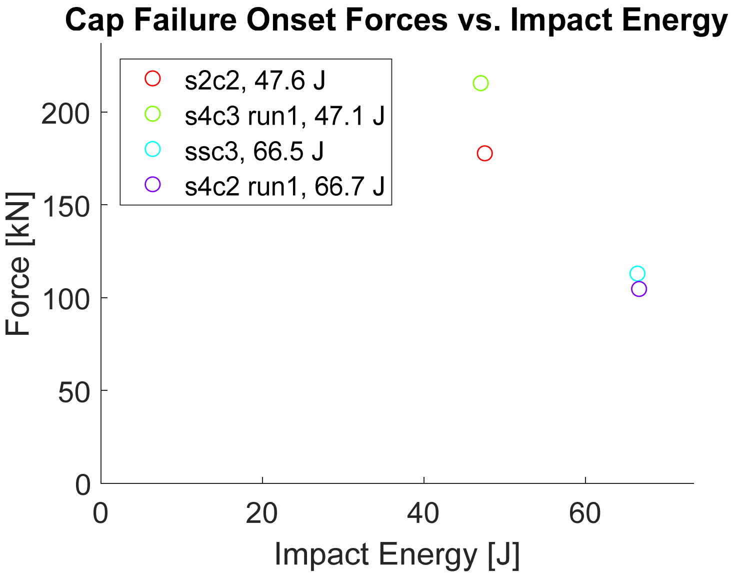

Figure 3.17. Cap failure onset forces vs. impact energy.

DIC measurements for these tests were taken with stereo camera pairs. For the stringer-side of the specimen, two sets of cameras were used angled about 45° from the plane of the specimen to better capture the behavior of each side of the stringer cap. DIC results are shown in Figure 3.17 for specimen SSC3 for the displacement field results at the frames directly before and after stringer cap failure. Sublaminate buckling can be observed on the stringer cap near the impact location and evidence of damage can be seen traveling down the web in the frame taken directly before failure (Figure 3.17a). This damage coalesces into a band of cracks through the center of the stringer cap and an overall buckled column shape as the failed cap displaces significantly (Figure 3.17b). This behavior is emphasized in Figure 3.18 that plots the progression of the out-of-plane displacement shape through the cap center across the test duration. The displacement shape starts roughly flat until some slight buckling of the cap and sublaminate buckling of the damage starts to occur. Post-cap failure the whole cap buckles inward and crack damage coalesces at the center. For this specimen (SSC3, 66 J impact), the initial cap damage was roughly symmetric, but for the S2C2 specimen, the asymmetric fiber damage as seen in the A-scan results (Figure 3.7) leads to a difference in pre-failure displacement fields.

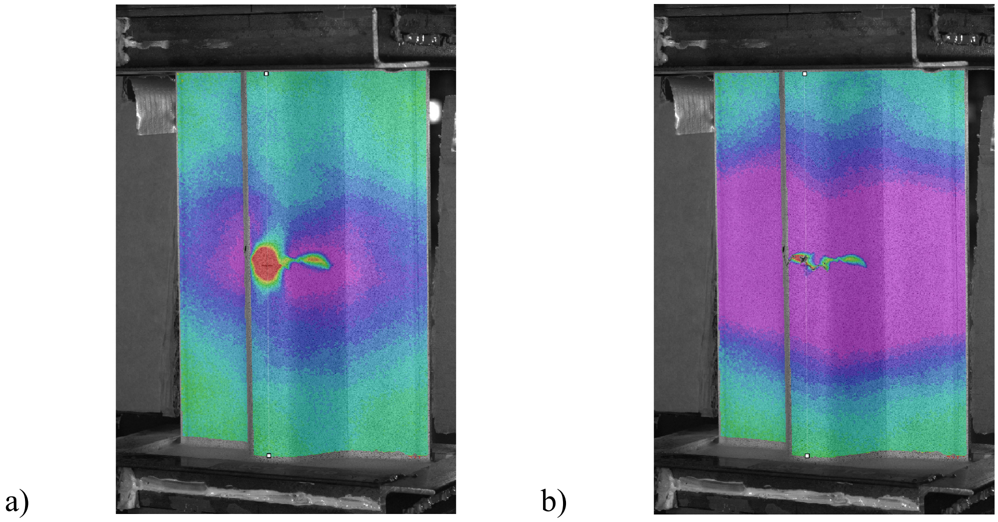

Figure 3.18. DIC out-of-plane displacement field results for specimen SSC3 at the frame a) before cap failure, b) after cap failure.

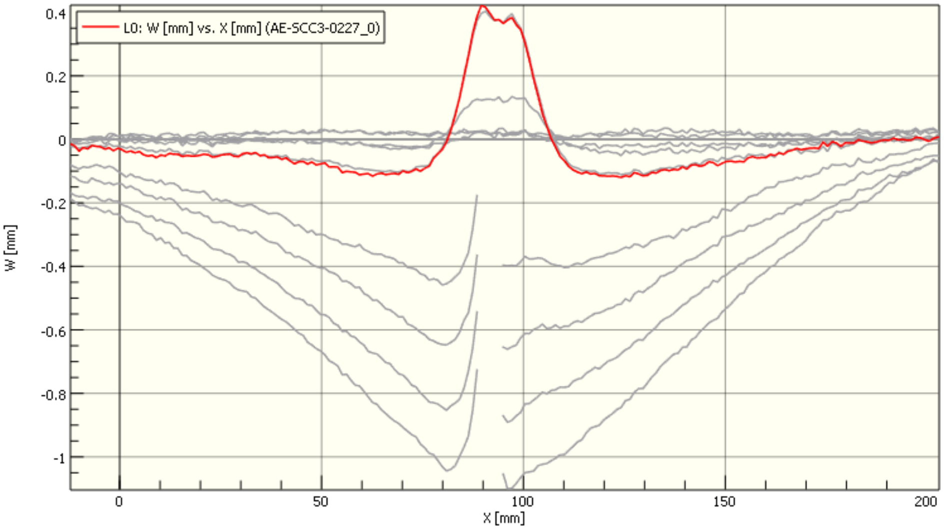

Figure 3.19. Line plot showing progression of the out-of-plane displacement shape throughout testing of specimen SSC3, Red highlights the displacement shape before failure and negative lines represent the shape after cap crippling.

Specimen S2C2 presents an interesting case because of the asymmetrical initial damage state and because it is the only specimen that exhibited a two stage progression of damage before failure. Figure 3.19 shows the loading curve for specimen S2C2 with two major load drops before the final failure event. DIC out-of-plane displacement results are shown in Figure 3.20 for the two sets of angled camera system pairs. For reference, the side of the cap captured by the left system corresponds with the A-scan results shown in Figure 3.7b (the side of the cap without web damage) and the right system corresponds with Figure 3.7a (the side of the cap with web damage). The DIC frames directly before the first load drop show a slight effect of the damage on the cap in the right system. Immediately after the first load drop, the asymmetrical damage leads to cap failure seen in the crown and right-side web, and after the second load drop the damage propagates fully across the stringer cap

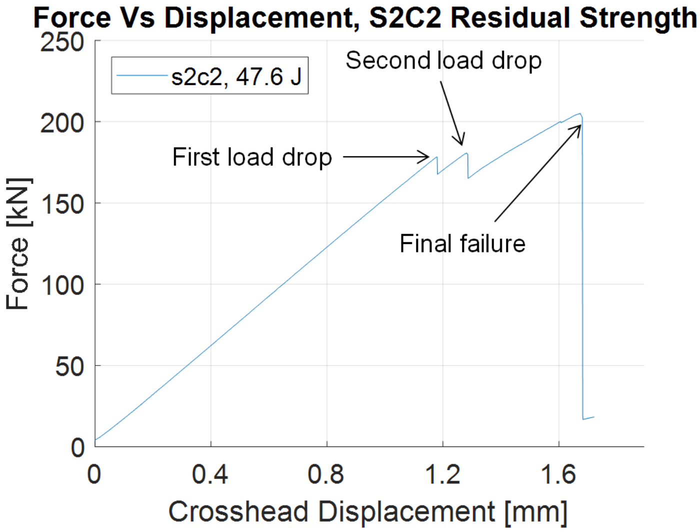

Figure 3.20. Force-displacement curve for specimen S2C2 showing two major load drops before final failure.

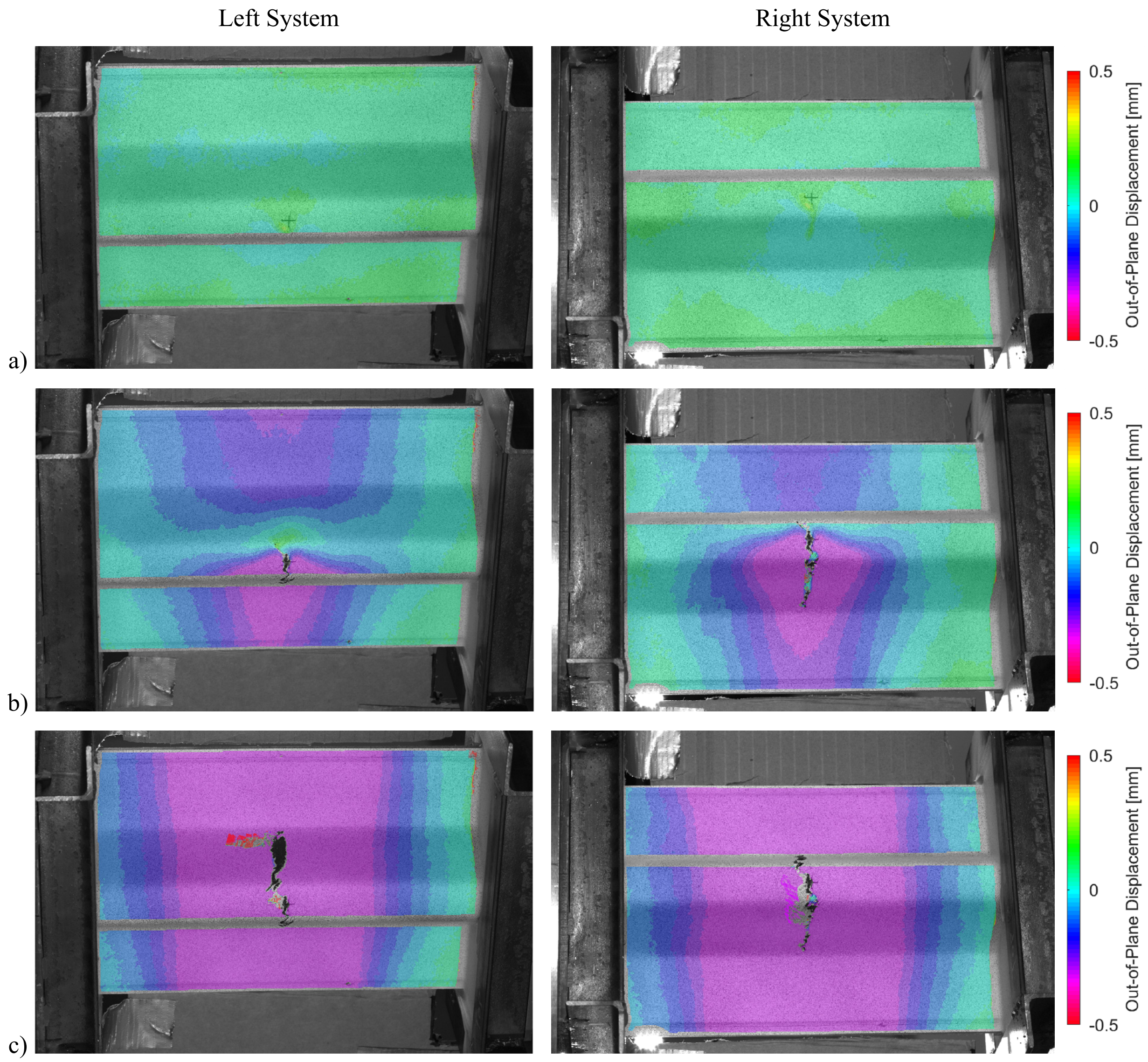

Figure 3.21. DIC results from the two camera systems for the frames immediately a) before the first load drop, b) immediately after the first load drop, and c) after the second load drop.

The first round of interrupted testing was performed up to the first major load drop (See Figure 3.22) and unloaded. Specimens were then inspected and CT scanned to investigate the progression of damage. Specimens were then reloaded to final failure. Force-displacement curves for the interrupted tests and the non-interrupted specimens at similar impact energy are shown in Figure 3.21. The reloading of the specimens appears not to have influenced the final failure behavior because the reloading stiffness follows the unloading stiffness from the first run in both cases. Both interrupted specimens (S4C3 and S4C2) are shown in Figure 3.22 after the first interruption. The damage observed in the S4C3 specimen after initial cap failure was much more severe, potentially because of the higher load attained before the onset of damage.

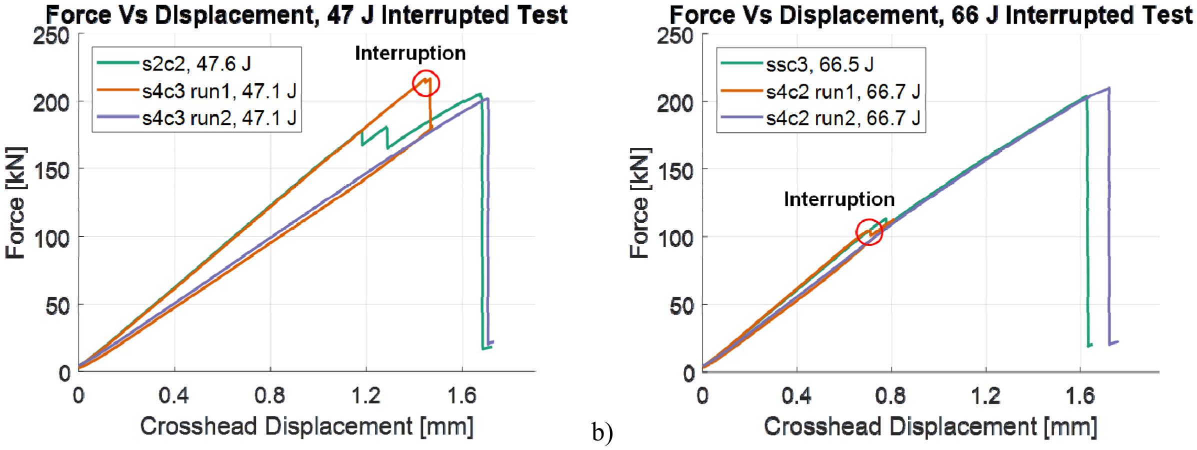

a) b)

Figure 3.22. Interrupted test results and similar impact energy non-interrupted tests for, a) specimen S4C3 and b) specimen S4C2.

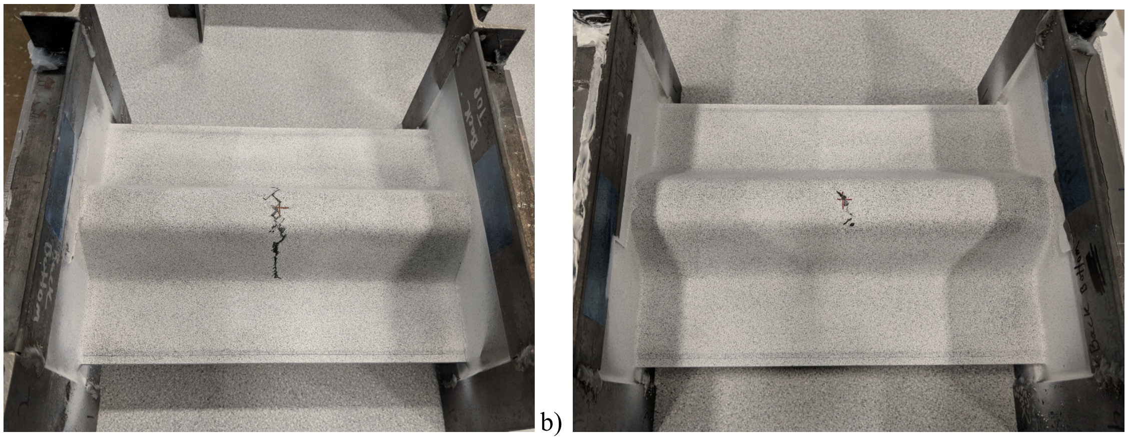

a) b)

Figure 3.23. Interrupted test specimens after the first compression test run. a) Specimen S4C3 (47 J impact energy). b) Specimen S4C2 (66 J impact energy).

Example CT scan results are shown and compared with pre-test scans in Figure 3.23. The observed damage state indicates severe ply damage and widely opened delaminations compared to the pre-test scan. Primary damage features of note are the development of severe crown damage and the migration of delaminations and ply cracks down the stringer web. The layer of white seen at the top of the specimen in Figure 3.23b is the layer of DIC paint.

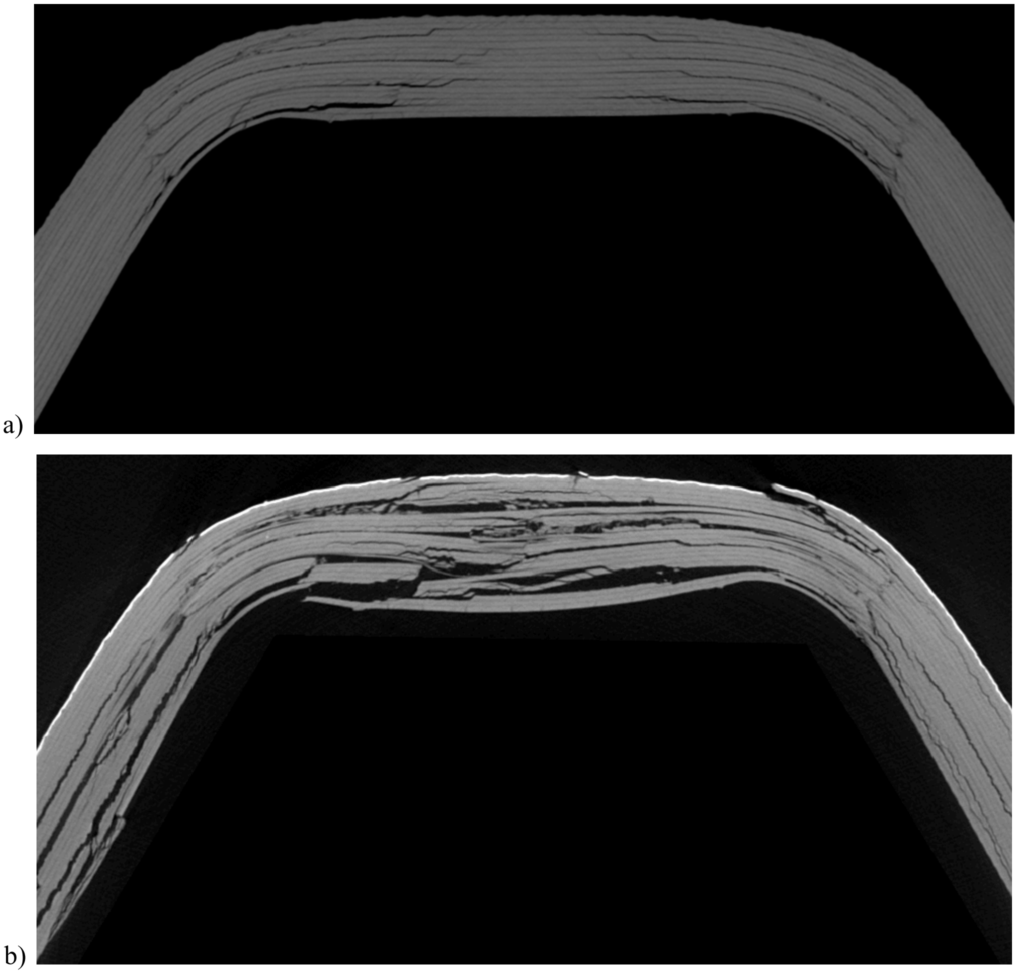

Figure 3.24. Example CT slices from specimen S4C3 showing the comparison between a) pre-compression and b) post-interrupted testing scans.

3.5 FLANGE-TYPE COMPRESSION TESTING

The flange compression testing setup is shown in Figure 3.24. Four total specimens were quasi-statically compressed until final failure. Two stereo pairs of cameras were used to collect 3D DIC data for the front and back. No interrupted tests were performed for the flange cases as no significant progressive damage behavior was observed during the tests.

Force-displacement curves are shown in Figure 3.25. The impacted specimens showed a reduction in final load of 20% and 27% for the 65 and 83 J impact cases respectively compared with the pristine specimen. Compared to the non-impacted loading curve, the impacted specimens were very slightly less stiff during the initial loading, but the primary difference in behavior was the failure displacement and peak load. Buckling of the skin occurred at around ~160 kN for all specimens and can be observed in Figure 3.26 as the inflection away from initial linear response in the load vs. displacement plot.

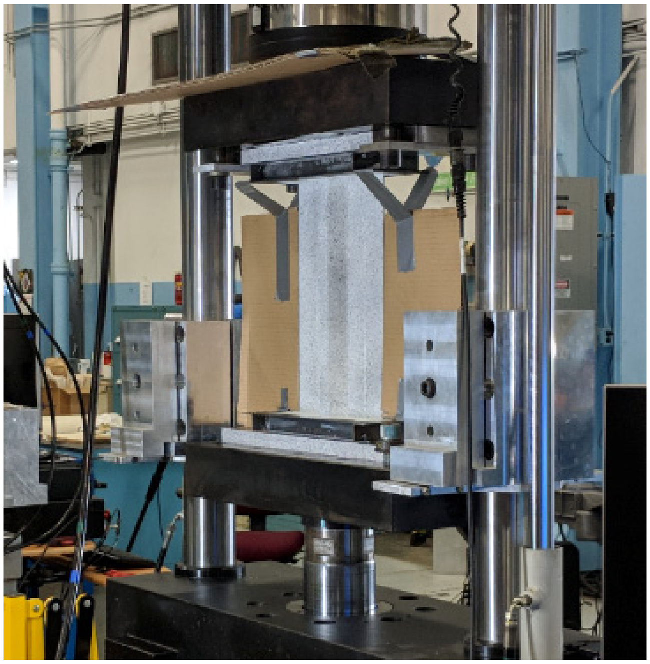

Figure 3.25. Flange compression setup.

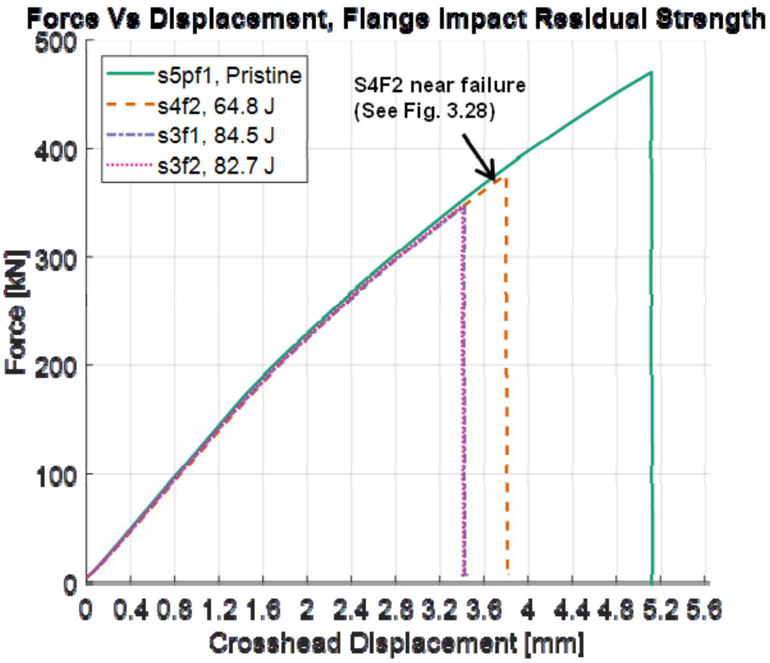

Figure 3.26. Residual strength force-displacement curves for flange type specimens. (Improve line visibility, dashing and whatnot)

DIC results establish a 3 half-wave skin buckling mode for all flange-type specimens as shown in Figure 3.26 as a 3D visual example and in Figure 3.27 in 2D for all specimens. All three of the impacted specimens had skin buckling with the middle half-wave coming towards the camera, whereas the pristine specimen had the opposite buckling shape. The stringer and flanges formed a stiffer box beam section and did not undergo large buckling deformations at the time the skin buckles. The impacted specimens also had a slight asymmetry of buckling shape with a larger displacement magnitude on the side of the stringer that sustained the impact.

Figure 3.28 shows example DIC results for the front and back of specimen S4F2 near failure. Figure 3.28a gives the displacement field from the front and back DIC results confirming the 3 half-wave buckling mode and showing that the stringer cap itself is relatively stable and does not deform with the buckling shape. Additionally, strain field results indicate a significant effect of the impact damage on the strain field. Example strain field results shown in Figure 3.28b for the strain in the loading direction illustrate strain concentrations near the middle of the specimen on the impacted side. From the back, strain concentrations in the skin are more noticeable and indicate increased compressive strain in the flange laminate as well. Shear strain results in Figure 3.28c show alternating concentrations corresponding to nodes in the buckling shape. Additionally, large concentrations in strain are observed at the end on the stringer flange on the back side. These concentrations are likely due in part to the resin rich fillet zone between the flange cut-off and the skin.

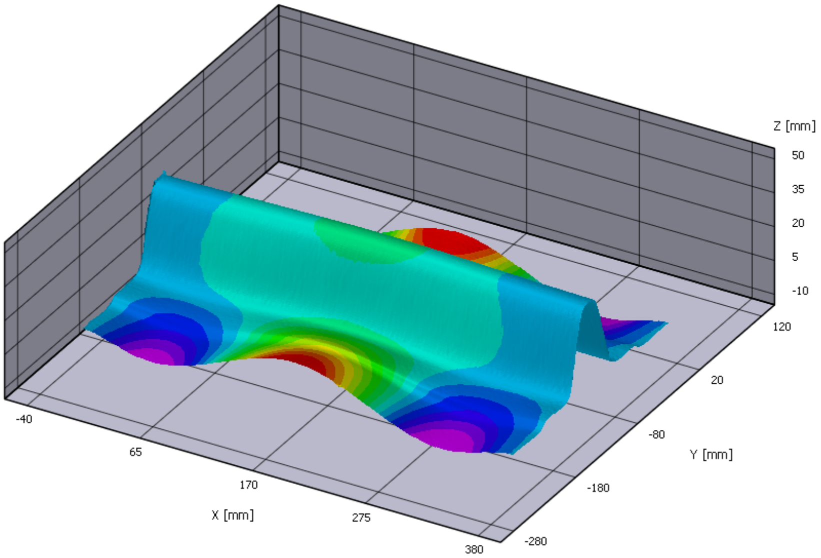

Figure 3.27. 3D view of post-buckling displacement shape for pristine specimen S5PF1 as seen from the stringer side of the panel.

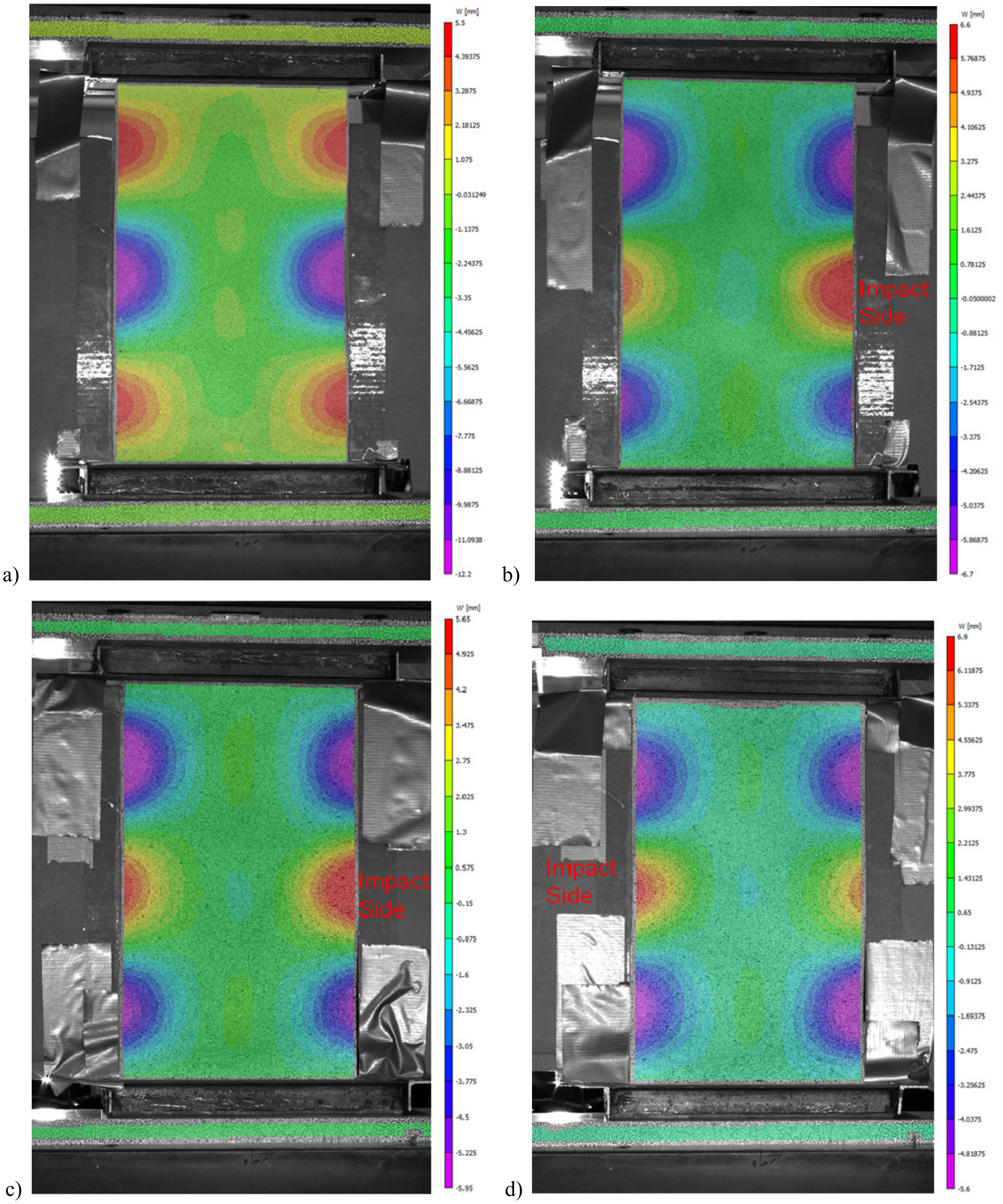

Figure 3.28. DIC out-of-plane displacement field for the skin side of the flange specimens at the frame before failure. a) Pristine specimen S5PF1. b) Specimen S4F2 (64.8 J Impact energy). c) Specimen S3F1 (84.5 J impact energy). d) Specimen S3F2 (82.7 J Impact energy).

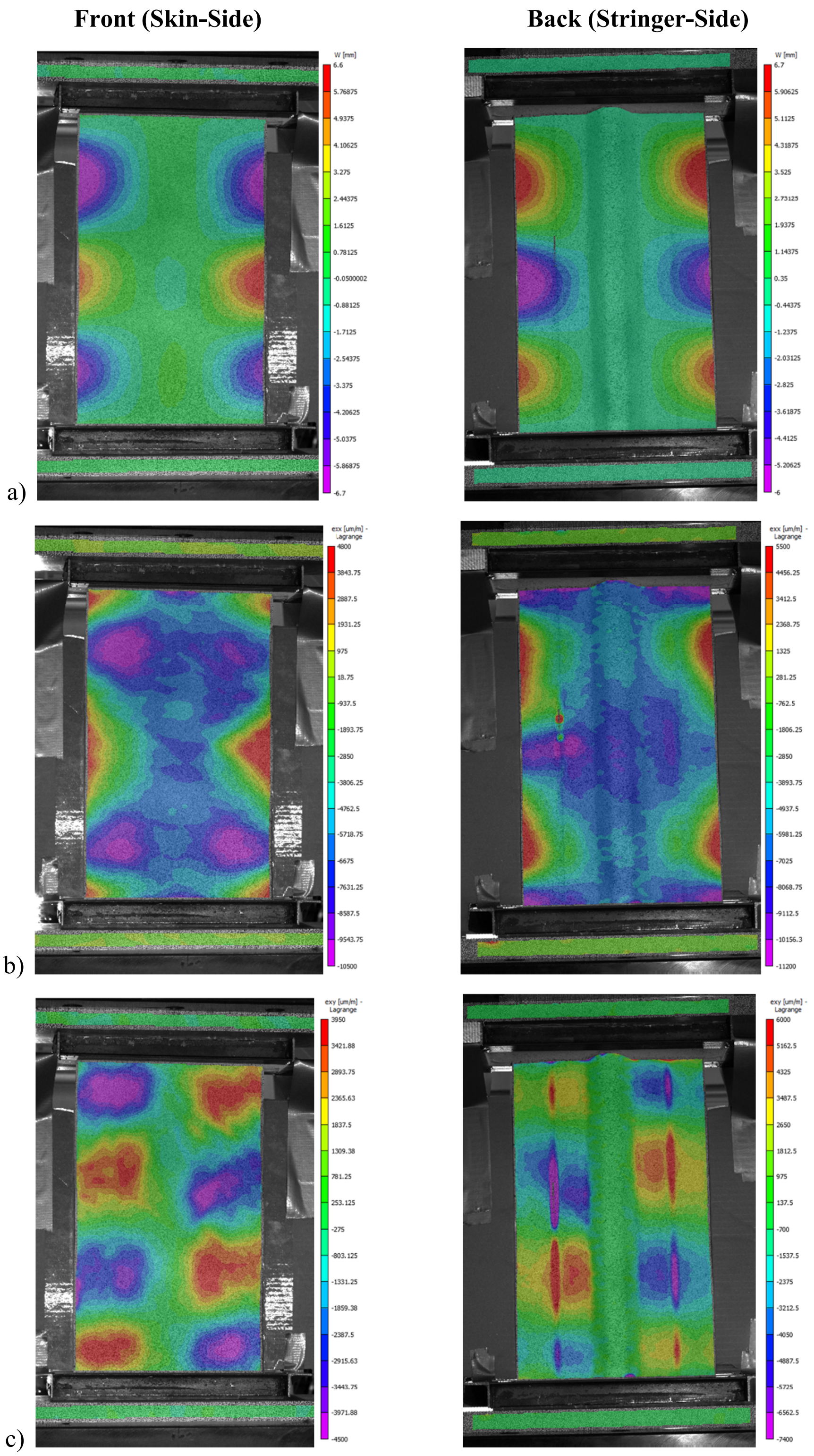

Figure 3.29. DIC displacement and strain field results near failure for specimen S4F2 (see Figure 3.26) from the front (skin-side) and back (stringer side). a) Out-of-plane displacement field. b) ε_{xx} strain (compression direction strain). c) ε_{xy} shear strain.

3.6 POST FAILURE IMAGES AND OBSERVATIONS

This section presents observations of the damage state post-failure to emphasize certain damage modes that should be captured in a residual strength model.

Various views of the damage state of specimen S2C2 are shown in Figure 3.29. The main modes of damage are seen as laminate failure in the stringer and disbonding between the stringer and skin with the skin remaining intact. This disbond was likely driven by the buckling shape that developed immediately following cap failure. The two non-impacted specimens are shown in Figure 3.30. Specimen S4PC1 (Figure 3.30a) shows a failure location slightly offset from the center with a similar, but more severe, damage state compared to the impacted cases. This severity is likely due to the much higher stored energy before failure. Specimen S1PC2 (Figure 3.30b) shows a failure location at the end potting that invalidates this test as a measure of specimen pristine strength.

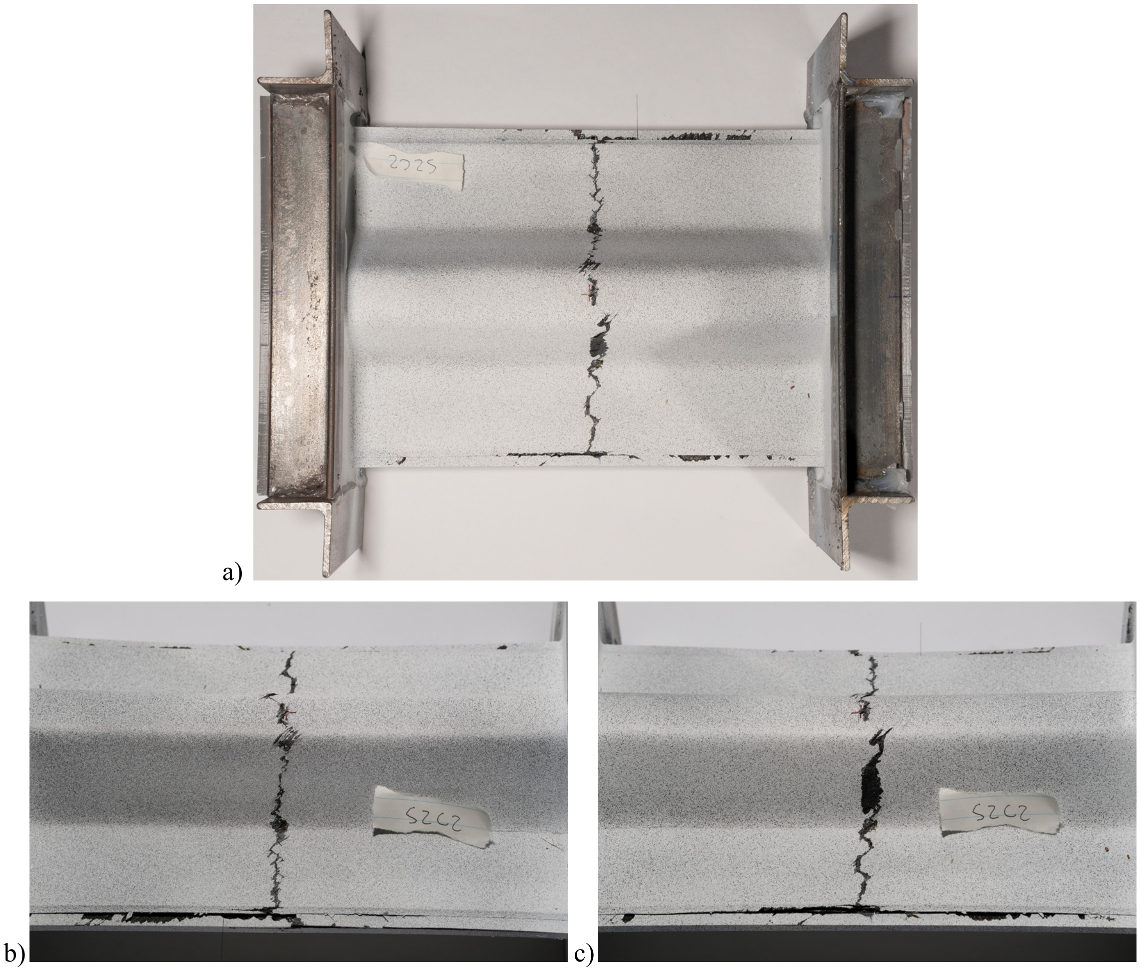

Figure 3.30. Detailed views of post-failure S2C2 specimen (47 J impact case). a) Overall specimen view, b-c) cap side views.

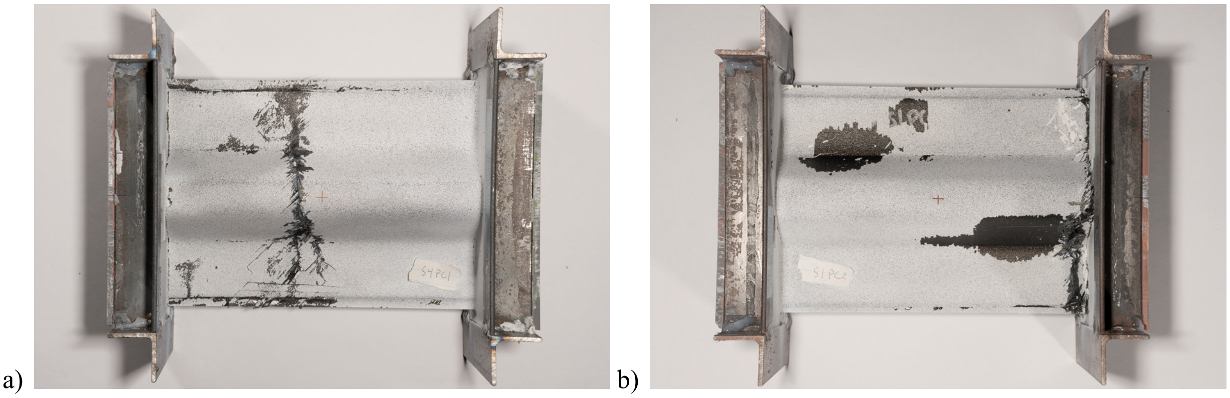

Figure 3.31. Images of non-impacted specimens after residual strength testing. a) Specimen S4PC1. b) Specimen S1PC2.

Flange-impacted specimens presented two major types of failure driven by the post-buckling behavior, laminate compression failure and disbond growth between the stringer and skin. Figure 3.31a shows an example of a failure mode driven by compressive failure of the skin and stringer laminates characterized by brooming failure. Figure 3.31b shows an example of a failure mode driven by post-buckling deformation and growth of the disbond between stringer and skin characterized by an extension of the crack between the skin and stringer flange and the residually deformed skin laminate. The difference between these failure modes may be the severity of the damage within the skin and flange relative to the size of the disbond between the skin and stringer.

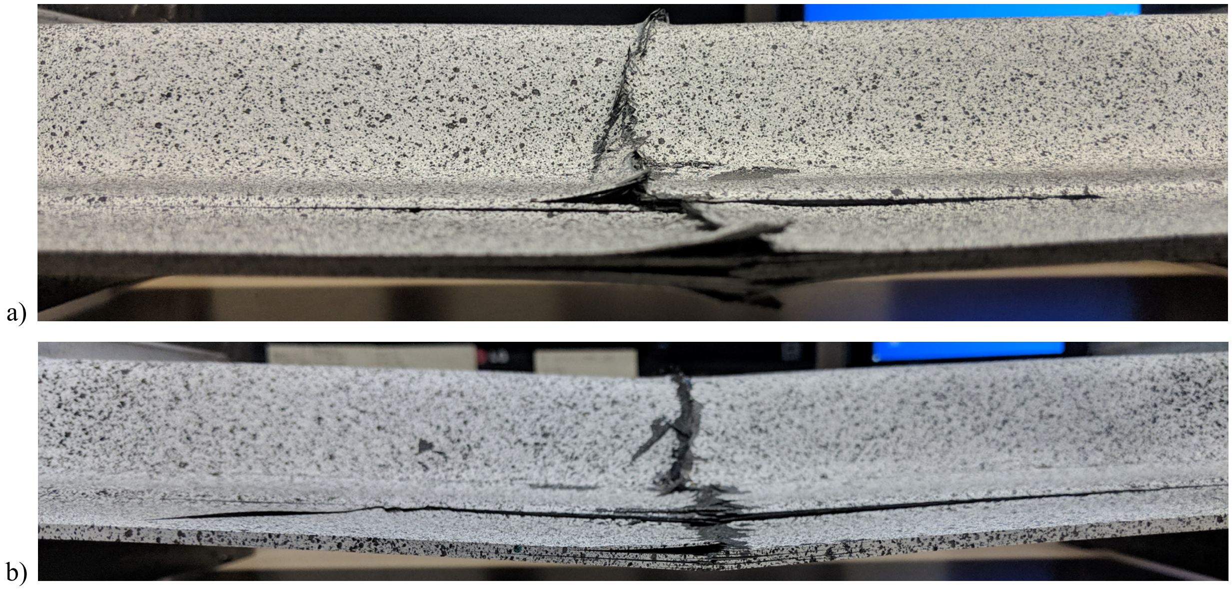

Figure 3.32. Images of flange impacted failure modes. a) Laminate failure dominated failure mode. b) Post-buckling bending and disbond growth driven failure mode.

3.7 STIFFENED PANEL TESTING DISCUSSION

Stiffened panel impact and residual strength testing demonstrated a strong dependence of the residual strength capacity of stringer panels on the location and intensity of impact. In the case of skin-side mid-flange impacts, increases in impact energy led to an overall decrease in the final load capacity, but not a significant change in the buckling response or pre-failure response. Alternatively, the residual strength testing of cap impacted specimens showed a pre-failure cap crippling event that was highly dependent on the damage severity and morphology with a final failure load that showed a weaker correlation with the impact energy. It is important to note that due to the relatively small number of samples it is difficult to make conclusions about the general residual strength trends, even though it is possible to identify damage features that likely contribute to the final response. A valuable aspect of these results, however, is to provide an abundant dataset that permits a systematic validation framework for guidance and validation of advanced NDE and residual strength simulation.

3.8 ACKNOWLEDGEMENT

Experiments and non-destructive characterization presented in this section were performed in collaboration with Hyungsuk Eric Kim, particularly the experimental impact testing and preparation of the specimens for residual strength testing. Additionally, the author would like to thank Chaiane Wiggers de Souza, Moonhee Nam, John Hamrang, and Paul Lee for their assistance in the manufacture of the composite stringer panel specimens.

Chapter 3 contains unpublished work researched together with Hyungsuk Eric Kim and Hyonny Kim.

4 ANALYSIS OF NON-DESTRUCTIVE DATA

This chapter presents analysis and segmentation procedures for X-ray CT and UT scan data as collected in the experimental programs of Chapters 2 and 3. First, Sections 4.1-4.8 present an automated CT analysis method that converts complex 3D scan data into damage maps for each composite ply and interface and quantifies damage features. This procedure is first presented for impact damage in flat composite panels and then extended to curved panels. Second, ultrasonic pulse-echo scanning analysis methods are presented, with the primary focus being a novel procedure to estimate delaminations that may have been missed in the initial scan by using an understanding of damage formation mechanisms.

4.1 COMPUTED TOMOGRAPHY BACKGROUND AND USE IN COMPOSITE ANALYSIS

X-ray computed tomography (CT) is a technique that fuses data from a series of 2D X-ray radiographs taken of a rotating specimen to calculate a 3D image of the X-ray attenuation properties of each chunk of material within a specimen by a process called filtered back-projection. A more detailed discussion of the theory of CT scanning can be found in Stock [25] and a general overview of the CT method as applied to various materials is given by Garcea et al. [26]. Additionally, Barrett and Keat [27] summarize and discuss the various CT scanning artifacts that become relevant during CT analysis. Several authors have applied CT to the study of damage in composite structures [28–36], but due to the complex nature of CT data sets, relatively few studies have approached automatic quantification of CT data into damage state information relevant to composites structures, such as delamination. McCombe et al. [35] presented a method for CT segmentation based on the depth of damage as a method to separate damage into delaminations based on peaks in the damage distribution. Léonard et al. [36] extended this segmentation approach to consider depth from a reference surface in order to account for the effects of laminate curvature and load induced non-planarity.

An alternative CT segmentation approach is presented in this chapter that instead divides a distinguishable specimen interior into plies and interfaces, accounts for various size interior gaps such as large delaminations, and projects both intraply and interply damage states to 2D maps at each layer. The results of this automated procedure are then used to create quantitative analyses of the impact damage state and enhanced visualizations. These results are then utilized further in Chapter 5 to validate impact damage predictions from finite element models and to generate CT informed residual strength models.

4.2 AUTOMATED SEGMENTATION OF X-RAY CT RESULTS

Although CT scanning can provide high fidelity internal damage information, issues such as non-planarity, fiber breakage, and data set misalignment complicate interpretation of the damage state. For example, Figure 4.1a shows a planar image of an impacted composite panel where the transition between plies is visible in the orthogonal slice due to residual indentation, fiber breakage, and dataset misalignment. An alternative view in Figure 4.1b shows a slice taken orthogonal to this planar slice that highlights the non-planarity of features such as permanent deformation resulting from fiber damage and large indentation. This characteristic limitation of orthogonal slices of impacted composite CT datasets prevents an accurate characterization of a total delamination/intraply damage state by viewing orthogonal slices alone because damage features from adjacent layers are visible in each slice and difficult to distinguish.

a)
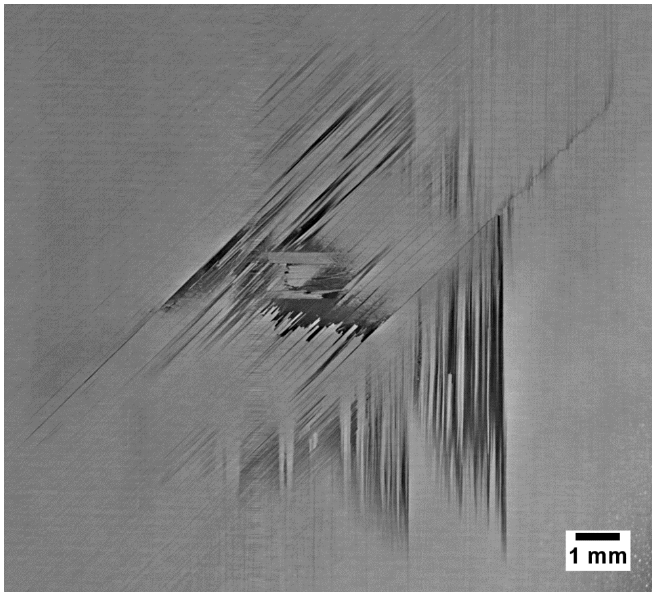

b)
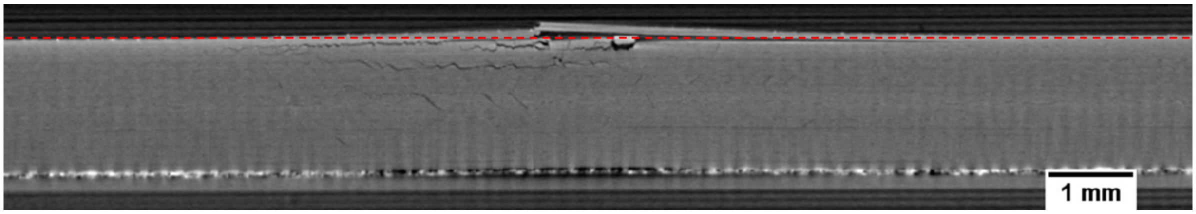

Figure 4.1. a) Example planar CT slice showing non-planarity as visible ply transitions within a single orthogonal slice. b) Through-thickness slice with the location of the planar slice in a) marked in red. Fiber breakage appears as a sharp discontinuity in the specimen near the top of the slice.

In order to address this issue and process CT data into a more comprehensible format, a segmentation routine was developed and implemented in MATLAB 2017a. The key steps of this routine take a series of through-thickness orthogonal slices (e.g., as in Figure 4.1b) of the CT dataset and: (i) produce a fit of the top and bottom exterior surfaces, (ii) divide the interior into a known number of plies and interfaces, (iii) detect damage based on a threshold pixel brightness, and (iv) project the damage within each ply and at each interface to a separate 2D map of damage. A detailed walkthrough of this procedure follows.

Figure 4.2 orients the CT dataset and how is it processed during segmentation. For these specimens, the CT dataset is a 35 x 25 mm sub region of the overall 102 x 152 mm specimen. Orthogonal slices are taken so that the vertical direction is oriented through the laminate thickness. In this description the term "pixel column" will be used to refer to a single pixel wide strip of pixels taken in the vertical (through-thickness) direction as illustrated in Figure 4.2. The general workflow for this procedure is summarized in Figure 4.3. Starting with a raw through-thickness slice as shown in Figure 4.3a, the exterior of the laminate is first determined. To separate the specimen from the surrounding void (dark regions above and below) and to handle the curvature of the specimen, the data set is fit by a vertical search procedure that finds the top and bottom of the laminate as the first and last pixels in each pixel column above a certain threshold luminosity. This threshold luminosity can be determined by studying a pixel luminosity curve through the thickness as shown in Figure 4.4. The threshold should be chosen to be below the average luminosity of the specimen but above the luminosity of surface X-ray echoes (see Section 4.8 for a detailed explanation of common CT features and artifacts). To alleviate the effects of surface imperfections, the exterior fit generated by this column-by-column approach is then used to create a piecewise linear fit of the entire 3D dataset as shown in Figure 4.3b, where the red outline highlights the exterior as determined by this procedure.

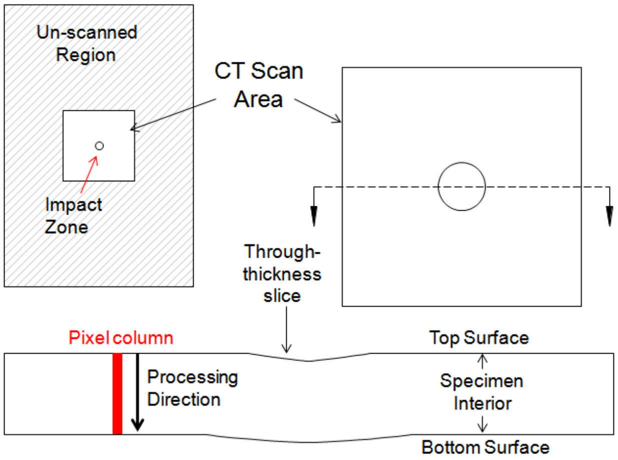

Figure 4.2. CT orientation. CT scanning of the impact zone was performed and then permuted into a series of through-thickness slices. In general, processing of the scan data into plies and interfaces domains takes place in each pixel column as represented in red.

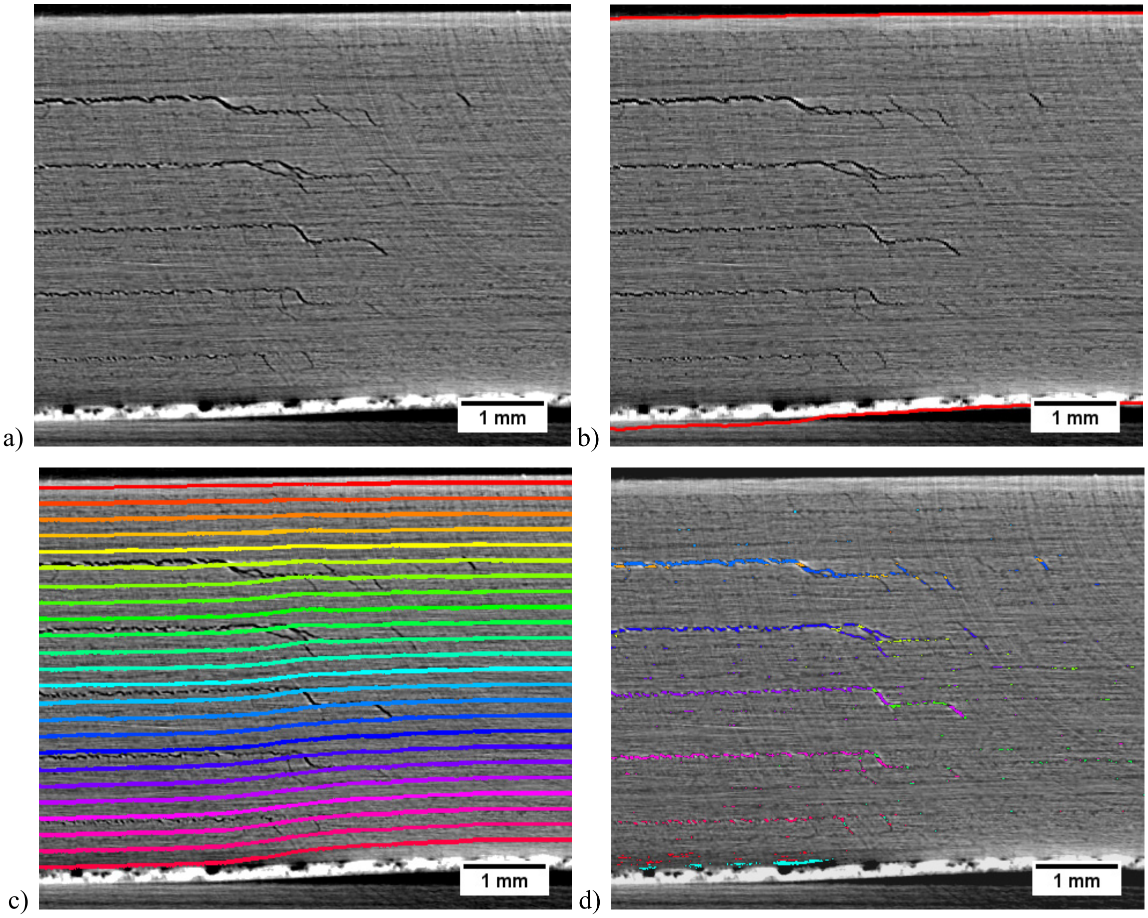

Figure 4.3. a) Raw through-thickness slice of a CT dataset, b) calculated exterior fit marked in red, c) ply locations after gap search and smoothing shown as bands of color, whereas interply regions are the gaps between color bands, and d) detected damage color coded as either ply (orange through teal) or interface damage (blue through red).

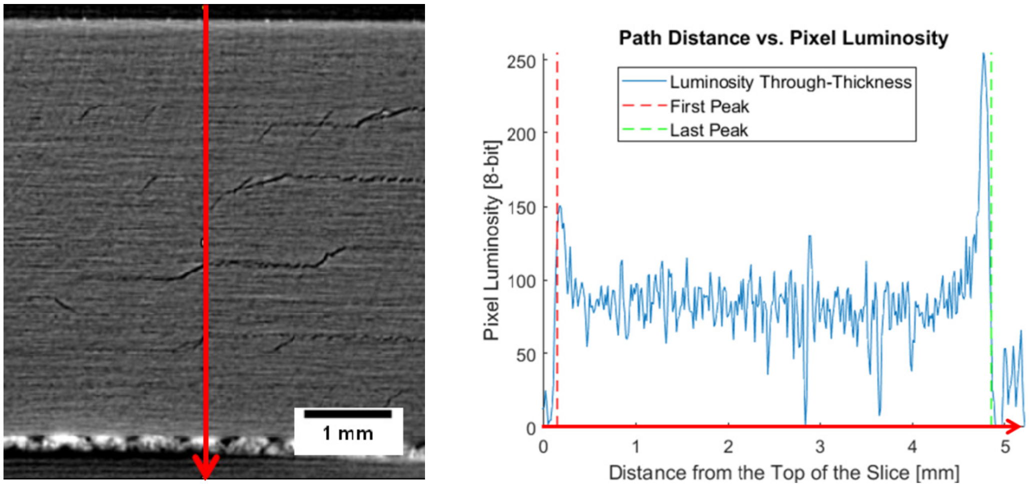

Figure 4.4. Luminosity through a sample through-thickness slice of the TC-24-31-1 specimen along the indicated red path. First and last peak results are shown for a threshold luminosity of 100 pixel brightness. Minor fluctuations in the luminosity within the laminate can be attributed to the variance in X-ray attenuation between matrix and fiber and noise (see the Discussion for a description of noise source in CT), whereas major drops in the pixel luminosity can be attributed to the presence of voids due to cracking or delamination.

After the exterior panel surfaces have been defined, segmentation is performed on the interior pixel columns in each individual slice to define ply locations and assess damage. First, a damage threshold is determined as the pixel luminosity value below which pixels will be considered damaged. One possible procedure to select the most effective damage threshold is by examining the luminosity curves through sets of damage features such as shown in Figure 4.5. The threshold should be chosen so that most of the damage features, but not the surrounding material, fall below this threshold. Because of variations in the material luminosity throughout the specimen, some of the undamaged material will likely fall under the damage threshold, causing the selection of the damage threshold to be a compromise between capturing damage versus indicating undamaged material as damage. An important feature to note is that for cracks with a smaller opening than the CT resolution pixels representing these voids will be reported as the volume averaged luminosity of the crack and the additional undamaged material that comprise the pixel. The resulting effect of this is that the smaller cracks generally located at the edges of the damage area are difficult to detect and can be lost within the general material fluctuations in luminosity.

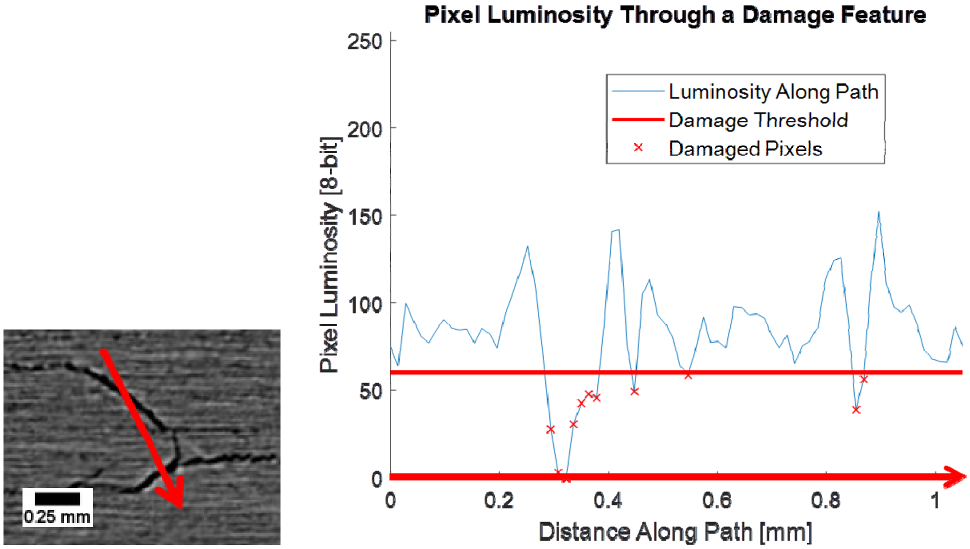

Figure 4.5. Analysis of damage luminosity, with a user determined threshold to check if visual damage features are appropriately detected. The red damage threshold line represents the luminosity value below which pixels will be marked as damaged. The path shown was chosen so that a variety of visible cracks and undamaged material would be spanned.

Next, because gaps existing due to delaminations may complicate the calculation of ply locations, large connected regions of damaged pixels are found by checking the connectivity of the damage in each column of pixels. For this process, each pixel column is converted to a set of binary values for each pixel depending on whether that pixel falls below the damage threshold. A search for long connected sets of binary damage is conducted using a binary connectivity search. If a connected damage region of greater than a few pixels is found, the indices of these damaged locations are saved and the locations are removed from the original pixel column. Ply center locations are then calculated by distributing plies evenly across the resulting pixel column. The removed damaged pixels are then reinserted, and ply locations are smoothed across all columns of pixels in the slice (see result in Figure 4.3c where colored contours mark ply locations). With the ply centers determined, the pixels are separated into plies and interface domains with respect to these centers. This separation is defined by a user-selected parameter that determines the percentage of the interior that is considered ply or interface. Although interfaces are generally conceptualized as small relative to the size of plies, waviness observed in the delamination paths prompts a finite portion of the interior to be marked as interface domain. Figure 4.6 shows a comparison of two different values for this user-defined parameter where ply regions are marked by semi transparent bands of color and interfaces are the regions between these bands. The 90% ply internal division of Figure 4.6a mostly fails to effectively capture the waviness of the nearly horizontal delamination cracks, whereas the 50% ply division of Figure 4.6b appropriately captures delamination cracks within single interface regions. For this reason, the CT processing was performed with the interior split into 50% ply damage regions and 50% interply damage regions.

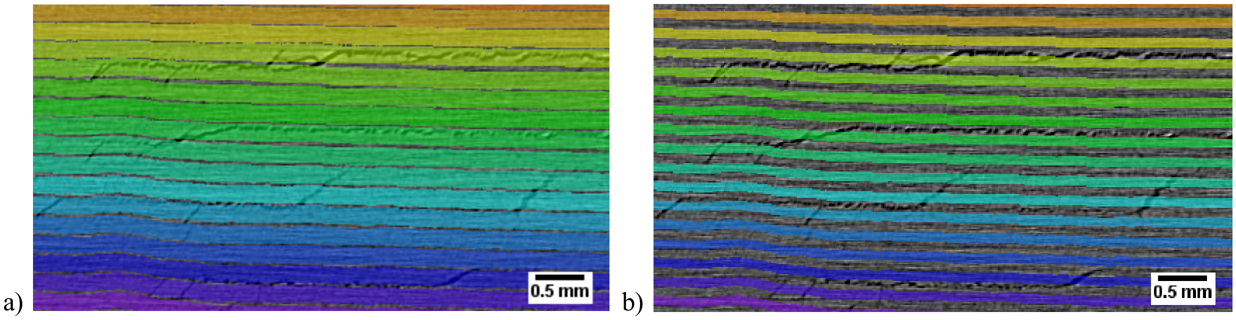

Figure 4.6. A subsection of the TC-24-31-1 CT data set showing superimposed color coded ply locations as semi-transparent bands of color with varying ply parameters. a) 90% ply and 10% interface division, b) 50% ply and 50% interface division. In these images, delamination is shown as mainly horizontal cracks, and matrix damage can be seen as slanted cracks bridging between delaminations. The 50% ply division of b) is generally better at capturing the horizontal delamination cracks within interface regions.

After plies and interfaces are determined, damage projection then consists of checking all pixels in each location and projecting a point of damage onto a 2D damage map representing each ply or interface for any pixels below the defined damage threshold luminosity. To visualize this process Figure 4.3d shows the original data slice with damage color coded as either intraply or interply as determined by the calculated plies and interfaces. The final outputs of this procedure include two sets of damage maps, one containing the projected damage information at each of the N-1 interior interfaces, and the other showing the projected intraply damage in each of the N plies.

4.3 X-RAY CT SEGMENTATION RESULTS

In order to provide qualitative validation of the developed segmentation method, the projected delamination envelope (i.e., delaminations at all interfaces combined) results from the CT segmentation were compared with conventional pulse-echo UT C-scan results to evaluate the overall segmented damage shape, as shown in Figure 4.7. Disagreements in the outer regions of damage may be due to the crack front tapering to a size smaller than the CT resolution but still causing a reflection of the ultrasonic waves. Despite some fringe disagreement between the two results, the overall damage shape is effectively captured by the projected CT segmentation delamination results.

Results from the developed segmentation procedure are shown for test specimen TC-24-31-1 in Figure 4.8 and Figure 4.9. Figure 4.8 shows the damage maps for each of the 23 interfaces in the specimen (delamination) and Figure 4.9 shows the damage maps within each of the 24 plies in the specimen (matrix and fiber cracks). These maps are created from the projection of damage from the calculated 3D ply and interface locations to a 2D representation. Each pixel in one of these damage maps represents whether a pixel luminosity value below the damage threshold was found to be located at the interface or within the ply location, with a black value representing damage, and a white value representing no damage. In the presented damage maps a few artifacts from the CT scan procedure such as a central vertical axis of noise are visible. These artifact features are explained further in the Discussion section. While damage at the interfaces is typically considered to be delamination, intraply damage can consist of both matrix and fiber cracking, and thus interpretation is needed to distinguish these two damage modes. Figure 4.10 shows two examples of intraply damage maps (for different specimens) which highlight the characteristic features of matrix cracking and fiber breakage. Figure 4.10a shows the ply damage for a -45° degree ply, where all of the damage features are parallel to the known fiber direction, whereas Figure 4.10b shows the ply damage of a 0° ply with some damage features parallel to the fiber direction and some features mostly perpendicular to the fiber direction. Given the structure of carbon/epoxy lamina, it can be concluded that the parallel damage features are representative of matrix cracking, and that perpendicular damage is likely fiber damage. Figure 4.10a thus shows a ply with only matrix cracking and Figure 4.10b shows a ply with both matrix and fiber cracking.

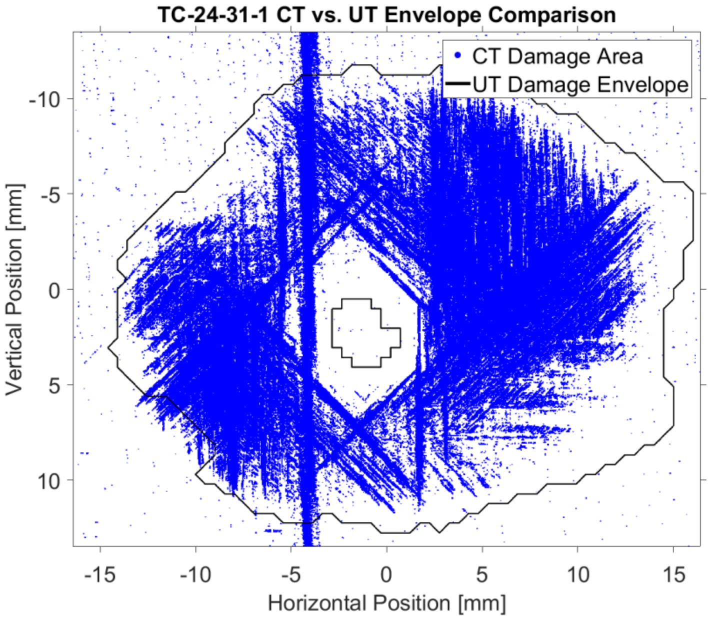

Figure 4.7. TC-24-31-1 projected CT damage with UT C-Scan damage envelope overlay.

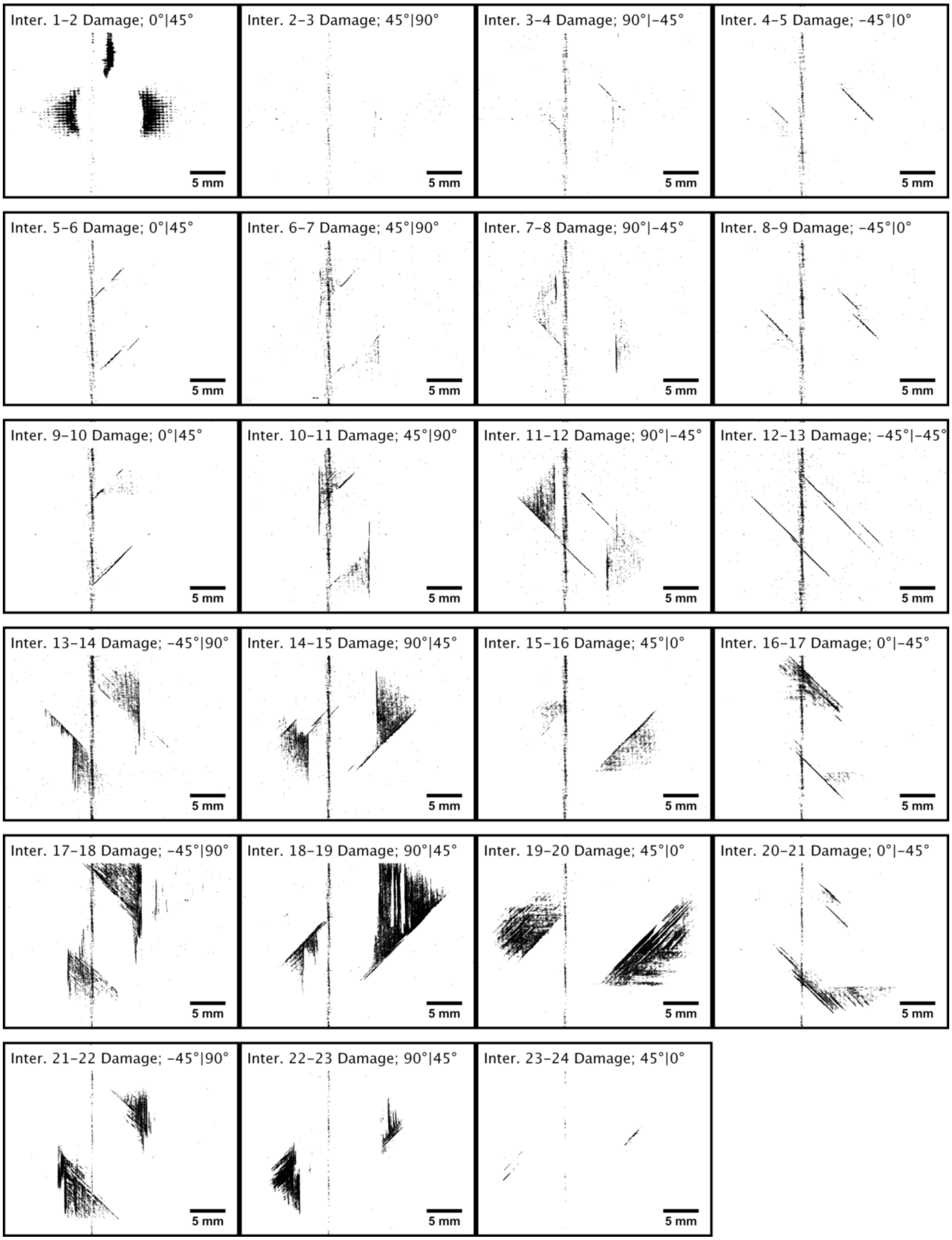

Figure 4.8. Damage maps for each interface for the TC-24-31-1 impact specimen. Each image represents the projection of damaged pixels onto a 2D damage image. Interface 1-2 denotes the interface closest to the impact side. See Section 4.8 for an explanation of CT artifact features and how these features affect the segmentation results. The 0° axis lies in the horizontal direction.

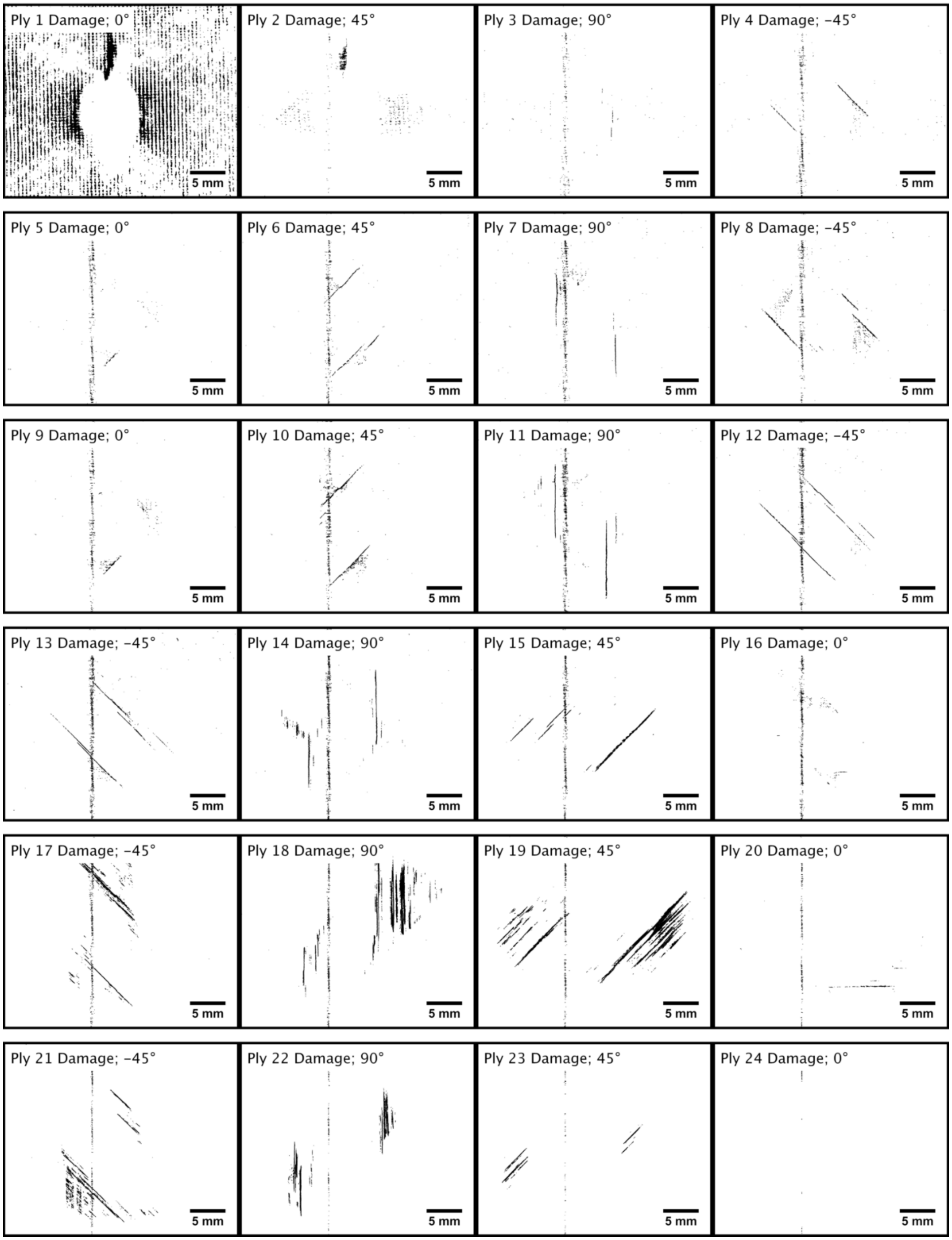

Figure 4.9. Damage maps for each ply in the TC-24-31-1 impact specimen. Each image represents the projection of damaged pixels onto a 2D damage image. Ply 1 is the ply closest to the impact side. See Section 4.8 for an explanation of CT artifact features and how these features affect the segmentation results. The 0° axis lies in the horizontal direction

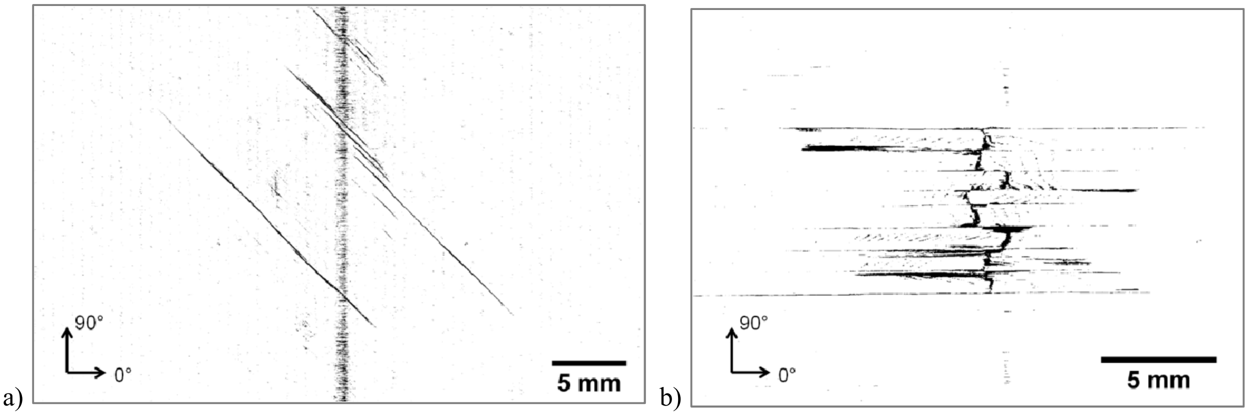

Figure 4.10. a) Ply damage map from TC-24-32-1 at ply 13 (-45°) showing only fiber direction oriented cracks and the central axis noise (see Section 4.8 for a description of general CT artifacts). b) Ply damage map from LV-071 at ply 24 (0°) showing fiber direction oriented matrix cracks and perpendicular fiber breakage.

The ply locations calculated by this segmentation procedure are shown for single orthogonal slices in Figure 4.11a for TC-24-31-1 and Figure 4.11b for LV-071. Figure 4.11a is an example of ply locations for an impacted composite laminate with no major discontinuities such as fiber breakage, and Figure 4.11b shows the effect of fiber breakage and large gaps on the ply calculation results, namely the expansion of the interface between the two ply locations nearest to the top surface due to the large separation of these plies, as visible in the CT slice.

a)
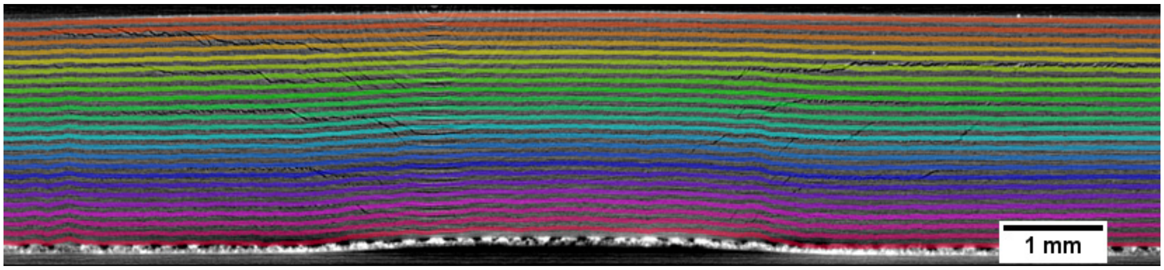

b)
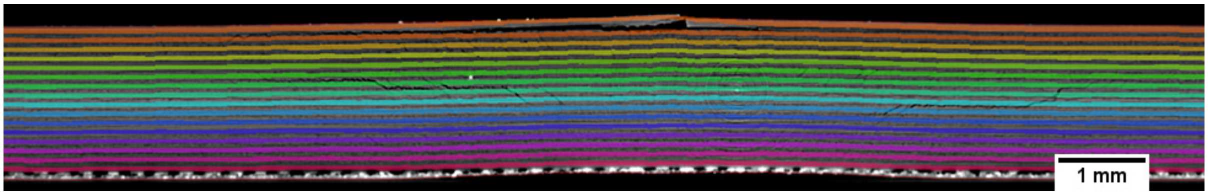

Figure 4.11. Calculated ply locations overlaid onto an orthogonal slice for a) TC-24-31-1 and b) LV-071. Slice a) presents an example of calculated ply locations without large gaps due to fiber breakage, whereas slice b) contains a sharp discontinuity and gap near the top of the slice.

From the exterior surface top and bottom fits, a map of the exterior contours on the top and bottom face of the impact zone can be extracted. The indentation depth at each point is calculated as the difference from that point's vertical position in its pixel stack and the linear interpolation between pixels taken from the edge zones significantly away from the impact zone, which are assumed to exhibit near zero indentation behavior. This procedure is illustrated in Figure 4.12. By applying this method to each pixel stack in the CT dataset, 2D maps that represent the non-planarity/indentation of the specimen can be generated for the front and back faces. Indentation maps are shown for TC-24-31-1 in Figure 4.13, where Figure 4.13a is the calculated residual deformation for the back face and Figure 4.13b is the calculated residual deformation for the impact face with brighter regions representing larger residual deformations. From the indentation maps, a dataset describing the thickness change in the impact zone can be calculated by subtracting the back face indentation map from the impact face indentation map as shown in Figure 4.13c. Generally, due to the localized indentation on the impact side and the more spread-out permanent deformation on the back face, the thickness change is negative (i.e., thinning) directly underneath the impactor but positive in the surrounding area. To simplify the input of residual deformation to modeling (e.g., for thin shell representation), the averaged front and back deformation profile is also calculated as shown in Figure 4.13d.

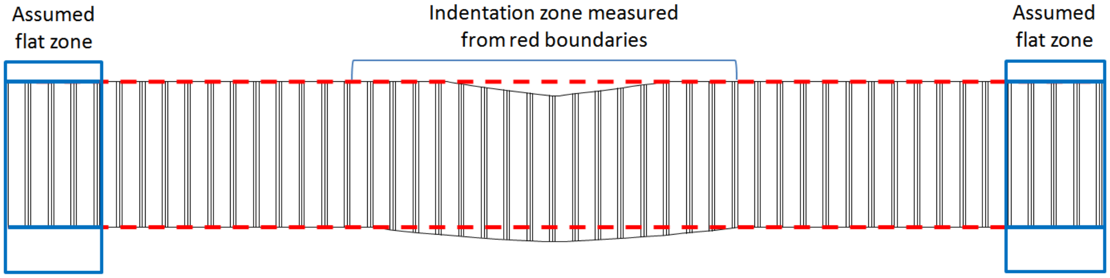

Figure 4.12. Indentation map calculation. The dotted fit line generated by interpolating between the assumed flat zones represents the plane of reference for calculation of the indentation from the surface of the specimen as fit by the segmentation.

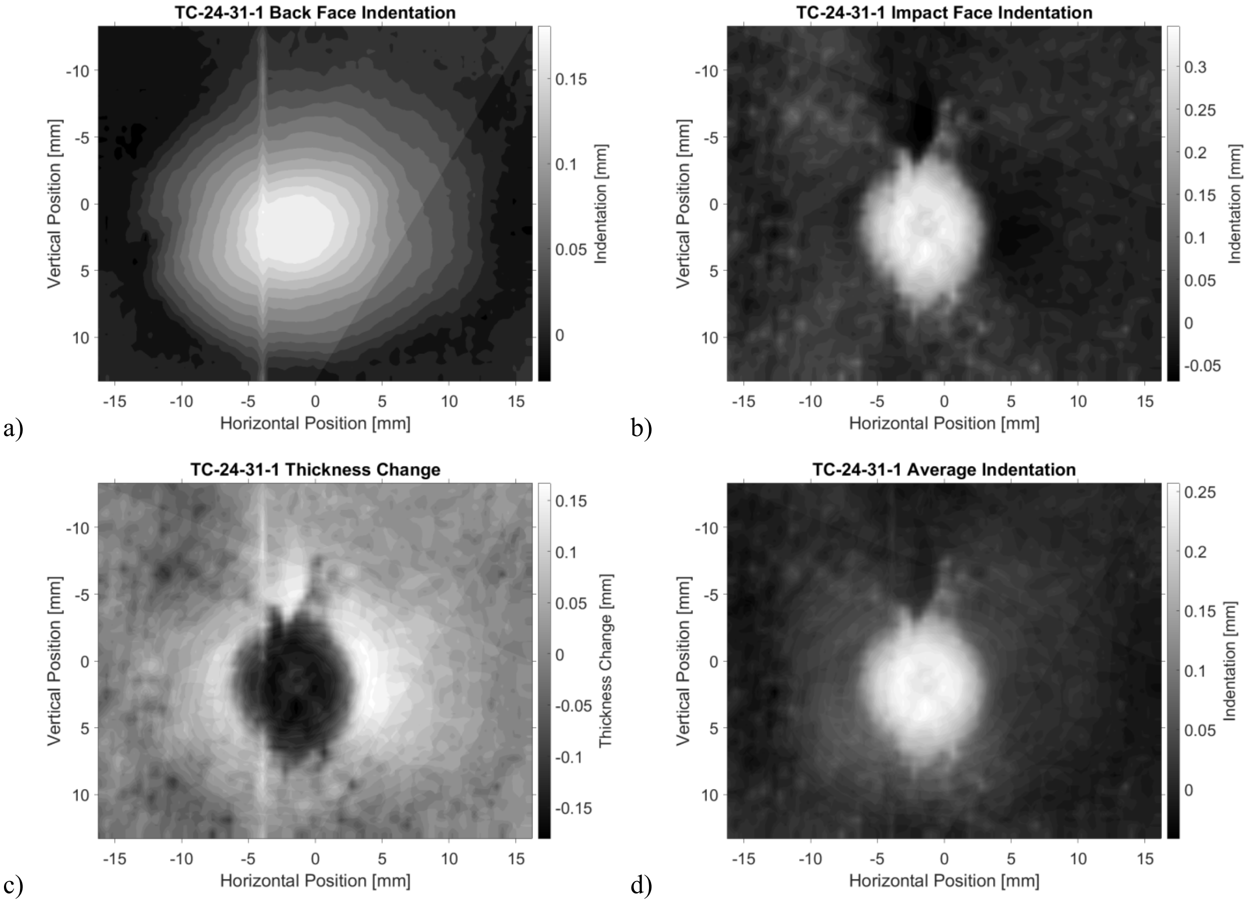

Figure 4.13. Indentation maps of the CT area calculated as distance from a reference plane. a) Indentation measured from the back face, b) indentation measured from the from impact face, c) change in thickness map calculated as the difference between the impact face indentation and the back face indentation, and d) the average of the impact and back side indentation maps.

4.4 DAMAGE FEATURE ANALYSIS AND 3D VISUALIZATION

The 3D segmentation results also enable calculation of spatial damage locations and orientation. The color coded damage dataset that marks each pixel below a certain threshold as damage within a specific layer can be interrogated to find damage features and convert them into simplified geometric interpretations. Figure 4.14a shows an example region from a slice of the color coded dataset where a specific damage feature is highlighted. This feature, portrayed here in 2D, is actually a connected region of damaged pixels that extends into and out of the page.

This connected pixel set is represented as a point cloud in 3D in Figure 4.14b where each point corresponds to a damage marked pixel in its 3D location in the CT data set. Because the marking of the pixels in the color coded dataset was based on ply and interface number, each connected set of damaged pixels can be considered a single damage feature within the respective ply or interface. The point cloud represented in Figure 4.14b thus shows a single matrix crack feature. By assuming that matrix cracks are a generally planar damage feature, it is possible to use a best linear planar fit to approximate this feature as shown in Figure 4.14c. This best planar fit then provides important crack geometry such as the crack's inclination in the ply, crack endpoints, and the overall damage size. By characterizing all matrix cracks in this way, a simplified dataset of ply damage can be developed. Similarly, delaminations can be characterized by a best planar fit.

This simplified geometric characterization also provides an important method for checking the quality of the segmentation. Based on composite structure and an understanding of composite damage features, supposed matrix cracks and delaminations can be verified based on their inclination and relative proportions. Matrix cracks should generally not be parallel to the plane of the ply and thus should have an inclination angle that is not close to zero degrees. Additionally, these damage features are usually thin compared to their length so aspect ratio can also be used to verify. Delaminations should be relatively parallel to the plane of neighboring plies and should have an inclination angle close to zero. Additionally, these features are usually not thin and should have a less dramatic aspect ratio compared to matrix cracks. These verification features can be used to filter out damage that has been incorrectly associated with plies or interfaces and also prevent noise features from being classified as damage. One more use of the inclination angle especially for matrix cracking is that certain physical models of composite damage, for example NASA Langley CompDam [37], take into account the angle of the matrix crack plane, and have seen that certain important stress effects cannot be captured without this information

These simplified damage feature datasets can then be used to create clear visuals of the damage state within an abstraction of the composite structure. Figure 4.15 shows a 3D visualization of the damage state of specimen TC-24-31-1 with planar representations of the damage features. Delaminations and matrix cracks are color coded based on ply and interface locations with delaminations as partially transparent and matrix cracks as opaque. Matrix cracks are represented with their accurate crack inclinations and can generally be seen to connect delaminations between layers. This 3D visualization allows a clear representation of the 3D nature of the damage state that allows a greater understanding of how damage features interact with each other and how they are distributed through the laminate.

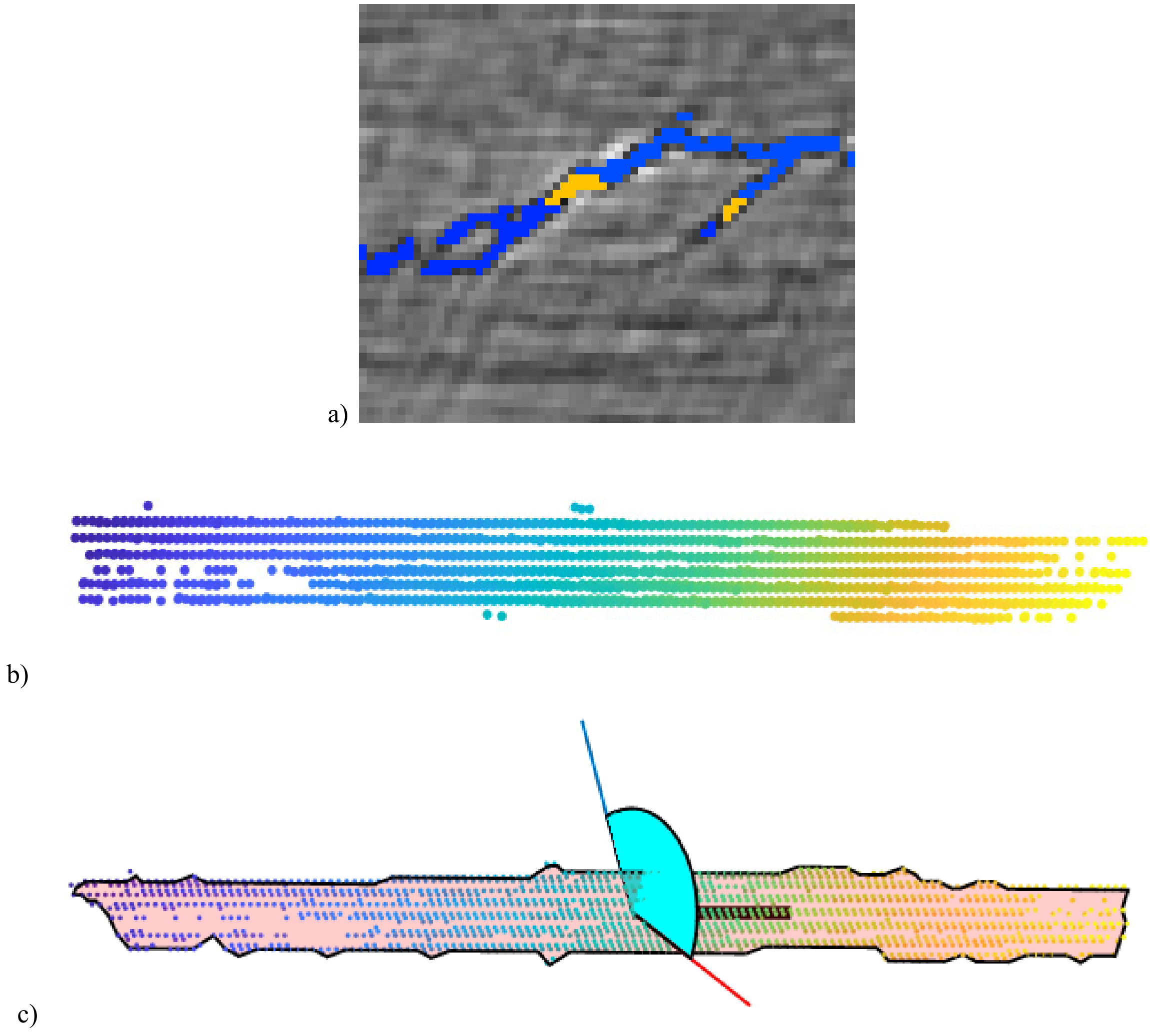

Figure 4.14. a) Example slice region in the color coded dataset. b) point cloud representation of the connected damage pixels for this matrix crack feature. c) planar fit through the connected pixels with the major axis of the crack as a black arrow, the through thickness direction as red, and the cyan plane as the crack inclination angle..

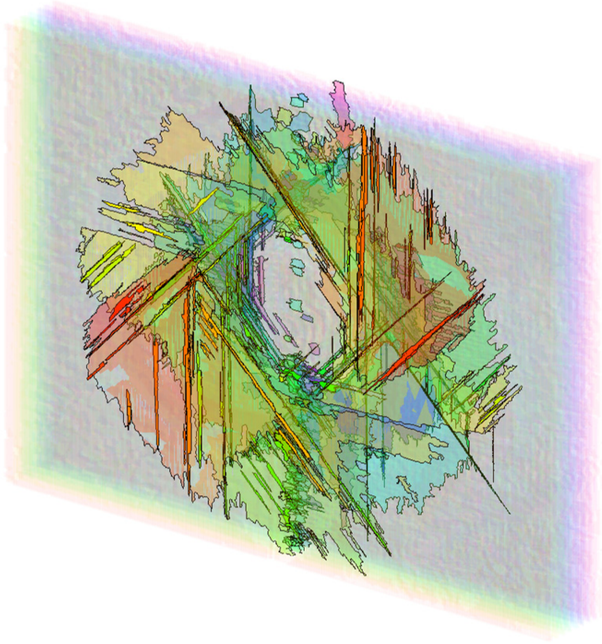

Figure 4.15. 3D visualization of damage state utilizing simplified damage planes color coded by layer. Matrix cracks are shown as opaque planes, and delaminations are transparent.

4.5 CT SEGMENTATION BASED DAMAGE INTERPRETATION

The generated CT segmentation results can provide insights into impact based composite damage mechanisms. Unlike most previously utilized evaluation techniques, which are limited in their abilities to map matrix damage and delamination together, this segmentation approach creates ply-by-ply and interface-by-interface damage maps that can be combined to enable new interpretations of damage formation. Figure 4.16 shows a combination of the intraply damage maps at plies 14 and 15 and the interface damage map at the interface between these plies. When plotted together, these damage maps highlight the interplay between ply cracks and interface damage. The domain of the delamination is bounded by the matrix and fiber cracks of the plies above and below this interface, showing a clear interdependency between these failure modes. Such interdependencies are not easily observed from the raw data (e.g. Figure 4.1) without being able to selectively overlay different layers of damage (e.g., damage in adjacent plies and the interface between), as enabled by this segmentation method. The connection between fiber direction oriented ply cracks in plies surrounding a given interface and delamination gives a clear map of the types of damage mechanisms discussed by previous authors such as Bouvet et al. [38]. In addition to the presence of two major lobes of delamination, as shown in Figure 4.16, various additional matrix cracks can be observed with smaller sub delaminations. This connection between matrix cracking and delamination will be discussed further in Section 4.11.

Beyond general qualitative interpretations, the segmentation results at each interface/ply location can be used to determine quantitative damage-describing parameters such as the distance of matrix cracks from the impact center, the lengths and spacing of matrix cracks, and the size of characteristic delamination shapes. For example, Figure 4.16 shows a quantitative measurement of the perpendicular distance between two major matrix cracks in ply 14 (fibers oriented at 90°).

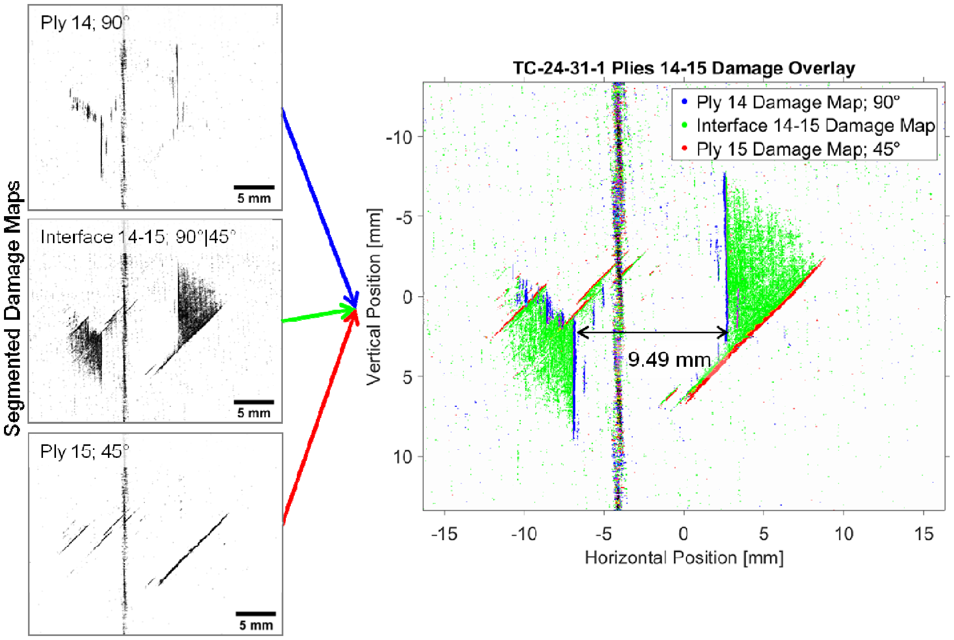

Figure 4.16. Bounding matrix cracks for the TC-24-31-1 specimen at the interface between plies 14 and 15. See Section 4.8 for a description of the vertical line noise present in this figure. A quantitative measure of the distance between two parallel 90° matrix cracks calculated using the CT resolution is shown on the overlay image.

4.6 CT SEGMENTATION OF CURVED COMPOSITE STRUCTURES

For segmenting damage states from CT scans of curved composite structures, additional features must be considered. Segmentation of curved specimen CT datasets begins in the same manner as the flat panel segmentation by aligning the stack of orthogonal slices into a through-thickness orientation where the ply structure is visible in each slice. Next, the exterior of the specimen is separated from the background by finding an exterior fit of the specimen. In each column of pixels, the first and last pixels above a minimum luminosity are detected (Figure 4.17a). Then the fit results from all columns are smoothed by applying a piecewise bilinear planar fit to the exterior to mitigate potential surface roughness. Due to the curvature presented by the radius region and the slant presented in the web region, segmentation of the specimen interior can no longer be performed by segmenting vertical stacks of pixel as was done in Section 4.2. To account for curvature, the normals of the exterior fit were calculated at each point on the specimen exterior, example normals are shown in Figure 4.17b. Next, the normals were used to connect points on the top surface to their relative points on the bottom surface. First, a reference surface was selected. In the case of concave down curvature as presented in Figure 4.17a, the top surface should be selected as the mapping of the normals from the top surface to the bottom surface will always have an output for each point on the top surface. The mapping connecting the top and bottom was calculated by intersection of the normal lines projected from the top surface to the bottom surface.

The next major step of the segmentation was to determine where each ply and interface should be found in the interior. Given that this structure was manufactured with a constant ply thickness, the ply centers were estimated by partitioning the normal line by the number of plies. Next, to determine the locations of interfaces a parameter was introduced into the segmentation to control the division of the interior into plies and interfaces by percentages. In idealized composite laminates, the thickness of the interfaces relative to the thickness of plies is assumed small, but in the case of realistic delaminations between plies, a large degree of delamination waviness is observed. This prompts us to use a close to equal ratio of thickness between plies and interfaces in our division of the interior; further information about the interior division ratio is detailed in Ellison and Kim [39]. Finally, the ratio of ply to interface and the locations of ply centers allow us to divide the normal into domains where pixels will be grouped along each normal, associated pixels were calculated by partitioning the normal into an array of coordinate locations and projecting these locations onto the nearest pixel using rounding. Pixels were then grouped by distance from the top surface into plies and interfaces. An example of the division of pixels along a normal into groups for each layer is shown in Figure 4.18. To determine the damage state in each ply and interface, a binary damage threshold was determined. If pixels with luminosity below this threshold were detected in that ply or interface, that location was marked as damaged. Additionally, to account for potentially large voids due to the presence of delaminations, if large connected regions of delaminations were detected the ply and interface locations were expanded about the large gaps and recalculated. To record the damage state for each location, damage was recorded to a series of 2D maps for each ply/interface and marking the location on the 2D map as damaged or undamaged according to the location of the reference point on the reference surface. The result is a mapping onto the 3D reference surface of the damage for each ply/interface, and accordingly the damage in the 2D map is stretched by the local normal and distance from the reference surface for each ply. Additionally, datasets were output for the locations of plies and interfaces in the interior as color coded regions, and the location of damage color coded by ply and interface as shown in Figure 4.19.

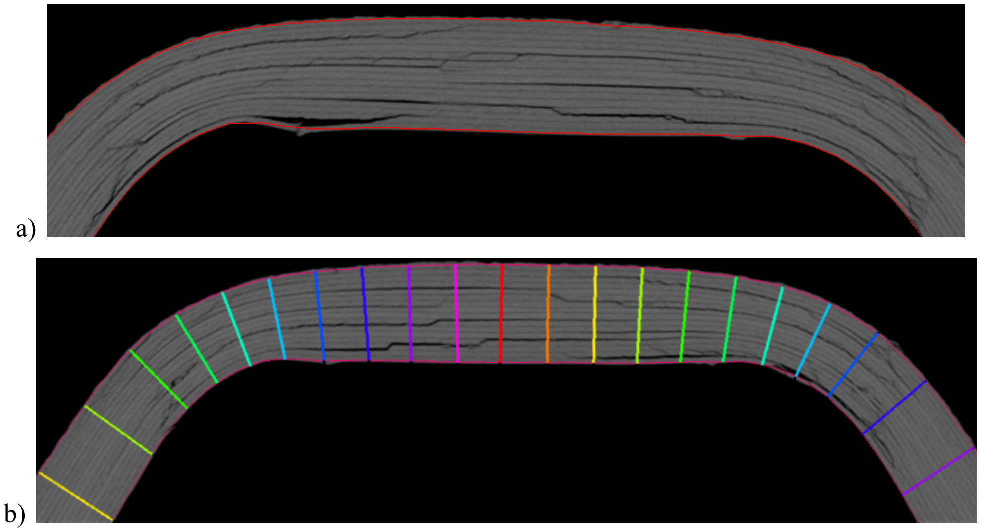

Figure 4.17. a) Stringer cap CT slice with the exterior fit shown in red. b) Example normals shown connecting the top and bottom fit.

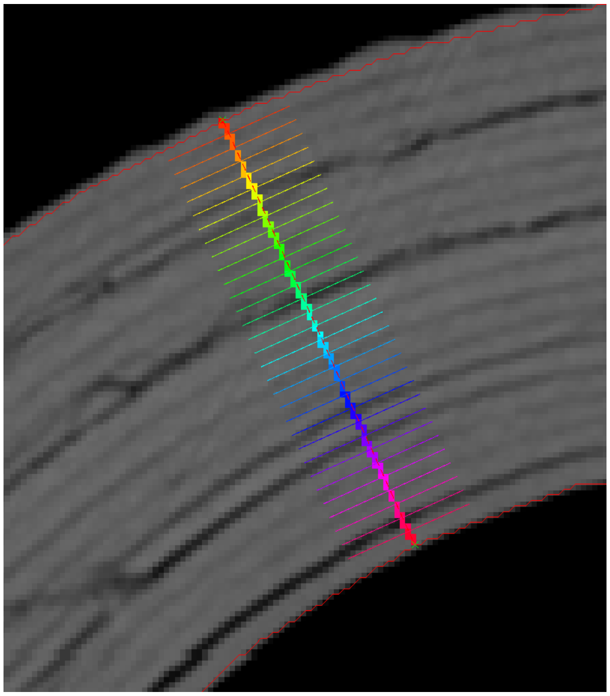

Figure 4.18. Division of a normal into pixel domains for each interface and ply layer. Colored lines represent the boundaries of pixel domains for each grouping.

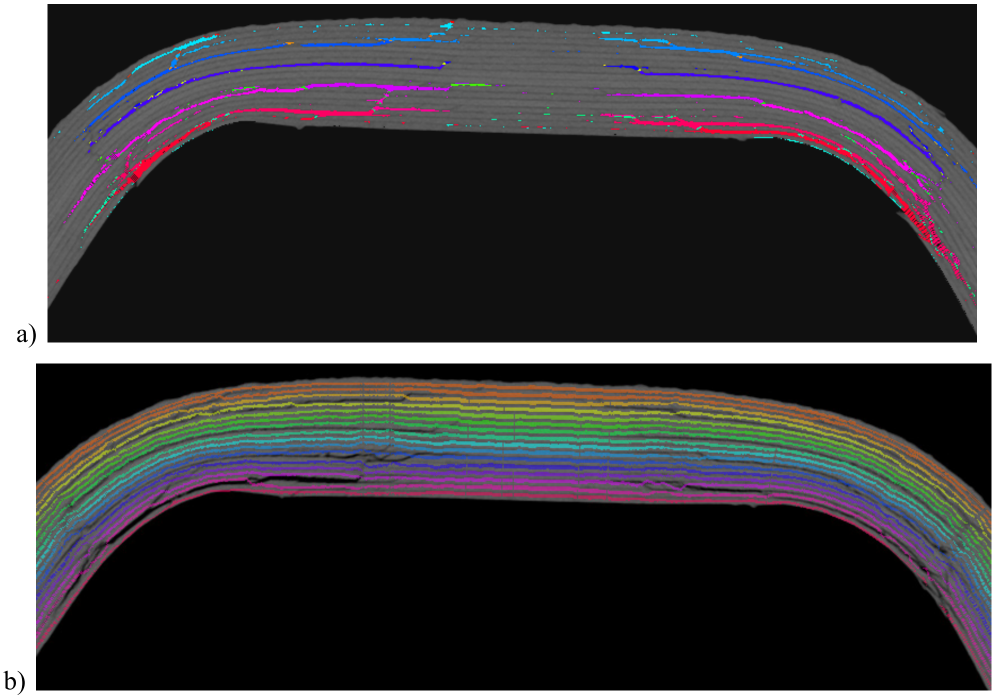

Figure 4.19. Example slices from 3D color coded datasets. a) Damaged pixel locations color coded by ply and interface number. b) Transparent color coded overlay of ply locations.

4.7 CT SEGMENTATION RESULTS FOR CURVED COMPOSITES

To clarify the definition and location of the 2D damage maps output by this procedure, Figure 4.20 illustrates how the 2D damage maps are related to the 3D specimen geometry. 2D damage maps are shown for specimen S4C3 in Figure 4.21 and Figure 4.22. To aid in the interpretation of Figure 4.21 and Figure 4.22, colored lines have been added that reference the normal lines plotted on an example CT slice in Figure 4.23. Interply damage maps (Figure 4.21) show strong dependence of the delamination shape at each interface on the directions of plies surrounding that interface. For example, interface 10-11 between a 0° ply and a -45° shows that the borders of the two delamination lobes are in the 0 and 45 directions with the delaminations seemingly swept out between these two boundaries. Based on the specimen geometry where the 0° direction is along the stiffener cap and the 90° is in the curvature direction, the 0° bounded delaminations tend to be very long and the 90° delaminations tend to be arrested within the radius region. Overall delamination behavior shows a spiral pattern of delaminations through the thickness. Additionally, delamination damage is generally contained within the lines that represent the end of the cap radius, indicating a strong effect of the curvature on damage formation. Intraply damage maps (Figure 4.22) generally show thin damage features, except where the segmentation procedure has erroneously grouped some delamination into the ply which may be due to delamination waviness. These thin crack features are usually located near the boundaries of surrounding delaminations.

Additionally, using the datasets of ply locations and damaged pixels, 3D visualizations of the damage state can be created as shown in Figure 4.23. To create this visualization, damage in each layer was searched for connected damaged pixels. These connected damaged pixels were then converted into best fit planes to approximate the locations of delaminations and matrix cracks. These best fit planes were then inserted into a color coded rendering of the ply locations.

As with any automated method, this segmentation procedure presents some key difficulties. Because this segmentation relies on the exterior surfaces and the normals connecting the top and bottom surfaces, discontinuities of this surface geometry created by very severe damage may make the interior definition ill-defined. To alleviate this issue, the surface fitting parameter that controls the smoothing of the defined exterior surface can be increased to smooth over discontinuities, but increased smoothing needs to be carefully chosen to avoid smoothing over the curvature of the structure.

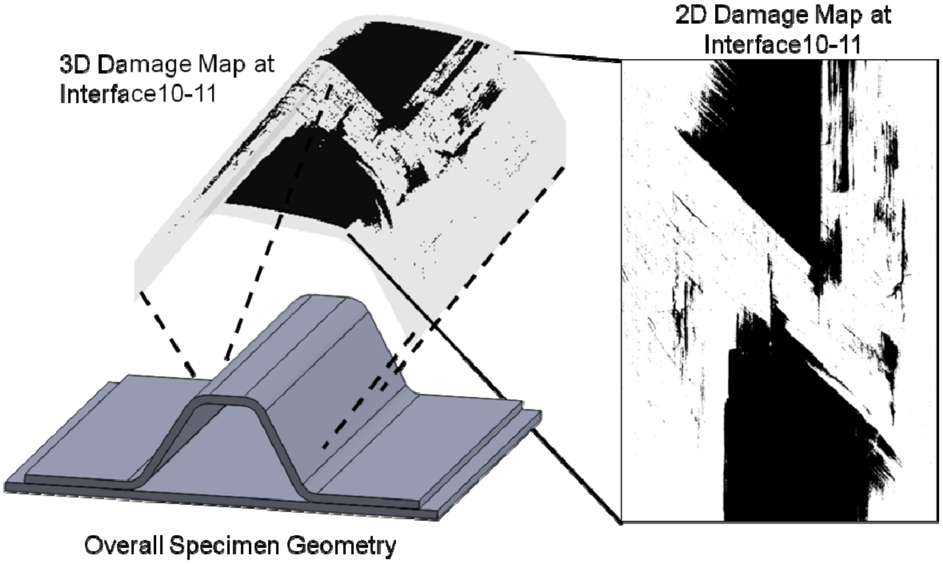

Figure 4.20. 2D damage map relationship with the 3D specimen geometry. 2D damage maps represent the flattened damage along the cap at each ply and interface.

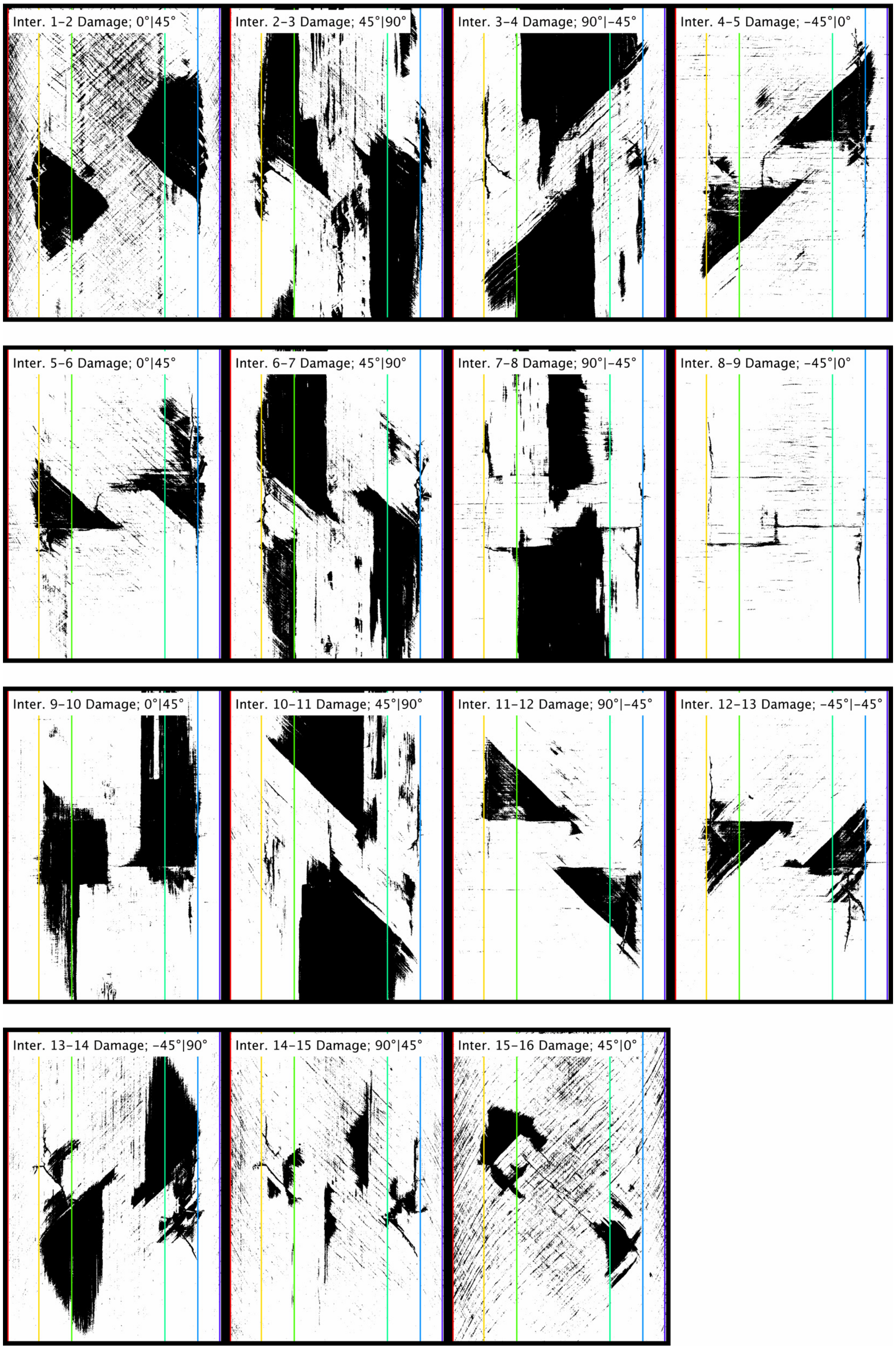

Figure 4.21. All interface damage maps for specimen S4C3. 0° ply direction is shown vertically. Colored lines reference stringer cap locations as shown in Figure 4.23.

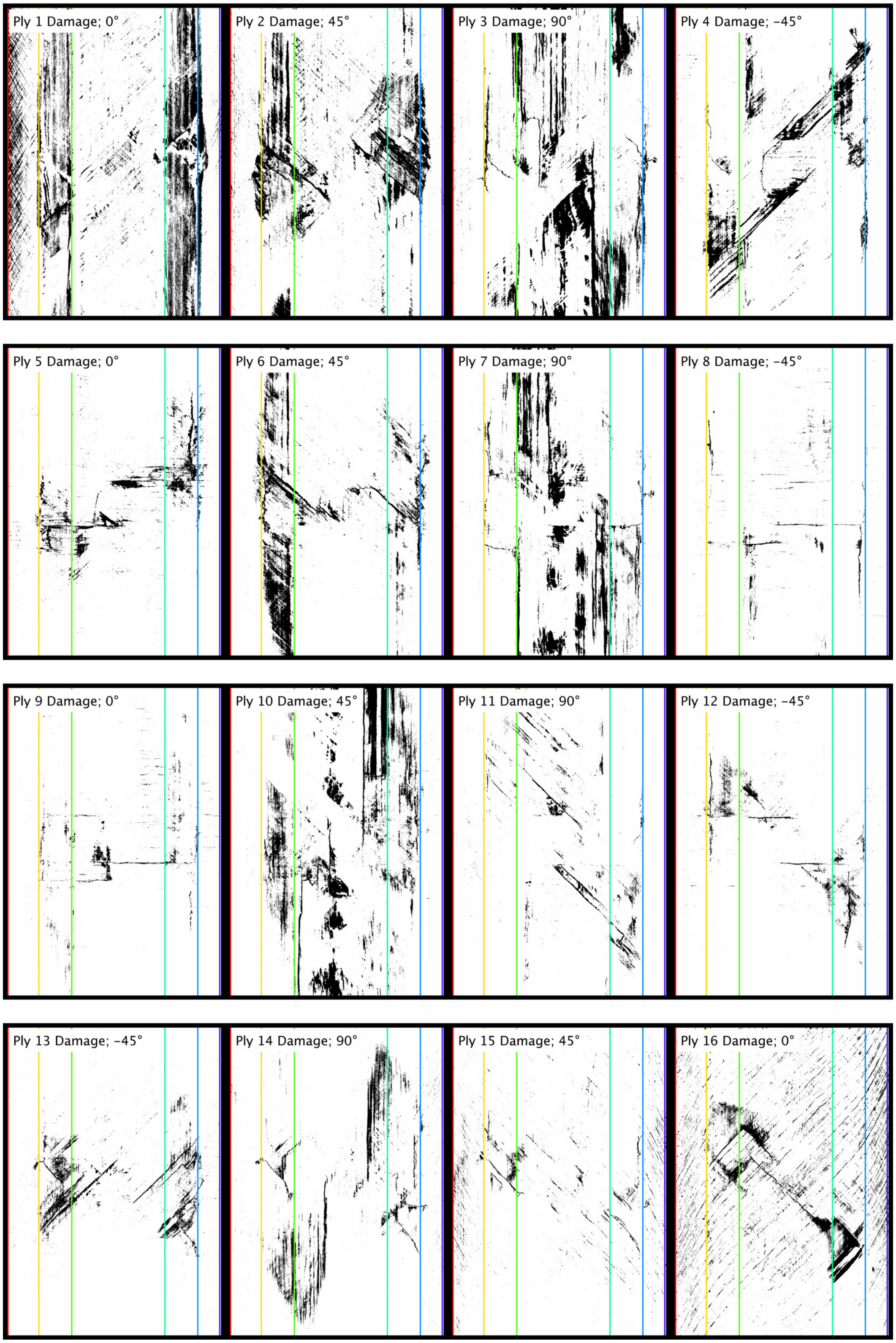

Figure 4.22. All intraply damage maps for specimen S4C3. 0° ply direction is shown vertically. Colored lines reference stringer cap locations as shown in Figure 4.23.

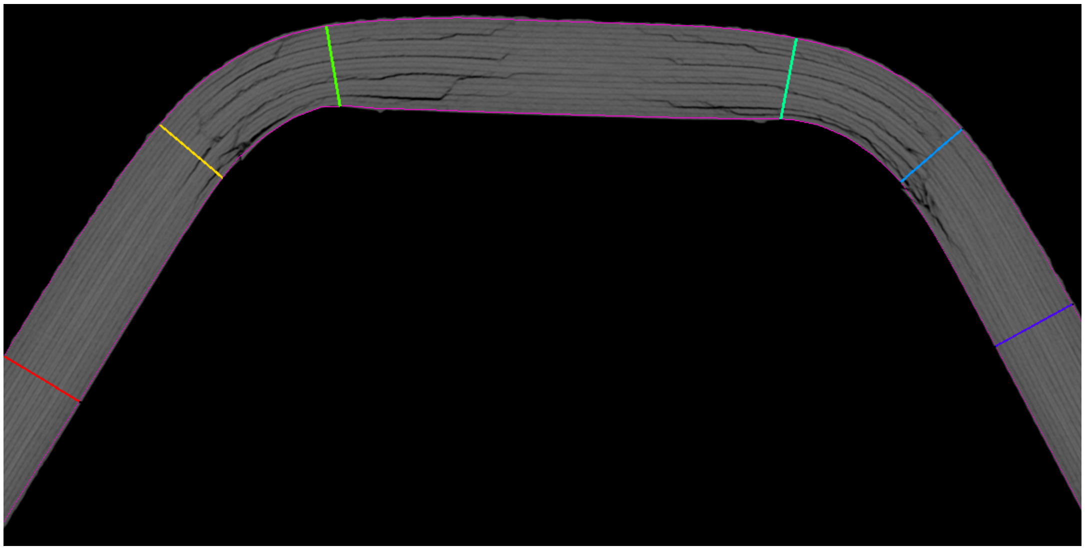

Figure 4.23. CT slice showing color coded normals for reference to Figures 8 and 9.

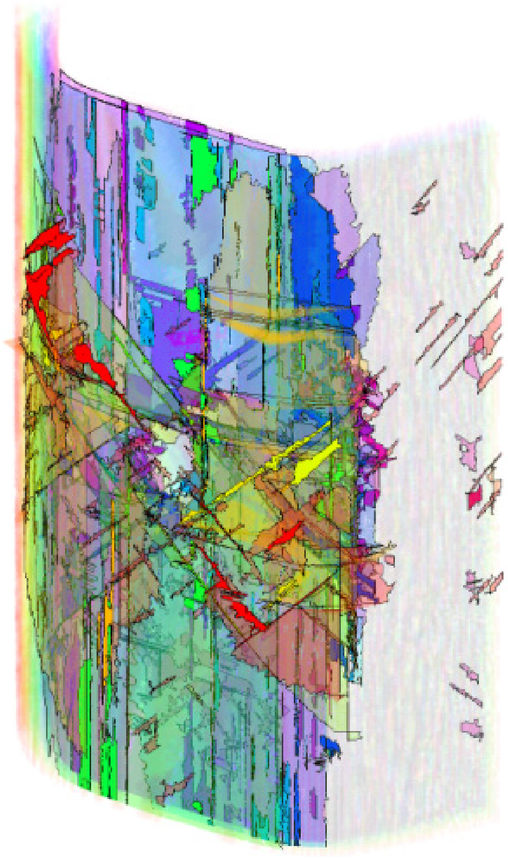

Figure 4.24. 3D visualization of color coded damage state based on the segmented damage state. Damage has been converted to representative planes of delamination and matrix cracking with delaminations shown as transparent and matrix cracking as opaque.

Additionally, this segmentation procedure can characterize the as-manufactured geometry in terms of the thickening and thinning that usually occurs during manufacture of curved components. The distance between the top and bottom surface along the connecting normal lines can be used to calculate the local thickness. Figure 4.25 shows a characterization of the variation of the laminate thickness across the stringer cap. Relative to the average thickness of the stringer laminate, the radius reduces in thickness by about 10% while the crown region increases in thickness by about 10%. This thickening and thinning behavior may have significant effects on the fiber volume fraction and resulting bending stiffness and modulus of the stringer cap. In the thickened region, the fiber volume fraction may be lower than the base composite, but due to the geometric effects of thickening, the actual bending stiffness may be increased in that region.

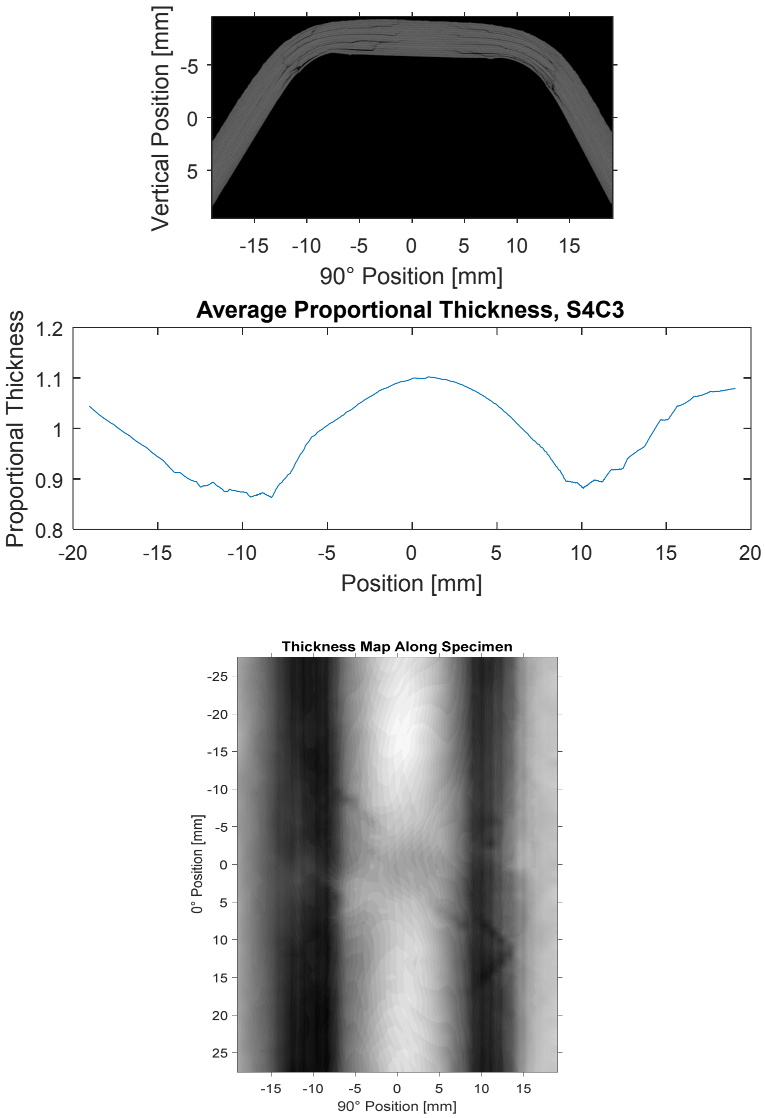

Figure 4.25. a) Example CT slice for geometry reference. b) Average thickness as calculated from the distance between top and bottom along normal lines. Position is calcuated as distance along the top surface. c) 2D map of thickness of the specimen in the scan region. Thickness tapers at the radii and increases in the center.

4.8 DISCUSSION OF CT ARTIFACTS

Some features of CT scanning artifacts and noise may be noted in the damage maps presented in this work, so a brief discussion of these formations and how to deal with such formations will be presented. The most notable artifact seen in these data sets is the presence of a dark vertical axis in most damage maps (e.g., see Figure 1a vertical line through the image). This artifact is a common feature of CT scanning systems that have out of calibration detectors [27]. Other features include a cross-hatch dark pattern on ply 1 and between plies 1 and 2 (e.g., see bottom surface of images in Figure 3). This feature is largely a result of the thin fiberglass surface ply which causes higher attenuation than the neighboring carbon fiber material, thereby resulting in beam-hardening artifacts [27]. From a visual perspective, these artifacts are quite easy to distinguish from the damage maps for both delamination and ply damage. However, because automatic processing of these damage maps to create damage sets for modeling would erroneously interpret these features as damage, erosion and dilation were applied to these features before processing the dataset into modeling information.

Additionally, some features of the CT scan process can have important effects on the processing parameters used for the segmentation. For the selection of the exterior fit luminosity, Figure 18 highlights the presence of a surface echo near the bottom surface. This feature may be created due to beam-hardening artifacts from the high attenuation fiberglass, resulting in an echo of material being reported by the CT reconstruction that is not representative of the real material exterior. This effect creates some difficulties for the selection of an exterior fit luminosity threshold parameter.

In terms of actual damage formations, as seen in the delamination results for interface 12-13 in Figure 8, damage is indicated at the interface between two adjacent -45° plies but is visibly matrix damage-like cracking. Although this automatic segmentation interprets this matrix crack as delamination, this interface result can be manually removed in accordance with other researchers' findings of a lack of delamination between like plies [2, 3, 38].

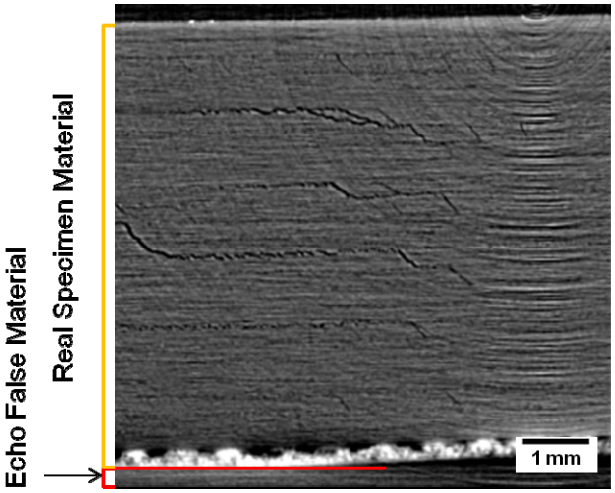

Figure 4.26. CT through-thickness slice showing the presence of an erroneous material echo from the bottom surface.

4.9 BACKGROUND ON ULTRASONIC SCANNING IN COMPOSITES MATERIALS

Ultrasonic scanning (UT) is a technique where an ultrasonic wave is excited and measured in a material or structure. One of the most common methods of measurement and excitation is through the use of piezoelectric transducers that create electrical signals in response to deformation. UT pulse-echo scanning where a single transducer sends and receives an ultrasonic signal is popular in field applications because it can rapidly identify the extent of damage with only single sided access. However, pulse-echo scanning is not generally able to characterize delaminations located beneath shallower-depth delaminations due to the majority of energy reflecting off of the first delamination in a phenomenon referred to as shadowing [40, 41]. Additionally, because pulse-echo scanning is most sensitive only to damage that lies perpendicular to the scanning direction, matrix cracking is hard to identify in normal-incidence scanning [42].

The following sections present a method to extend the ability of UT pulse-echo scanning to more fully characterize a complex 3D damage state in an impacted composite by using a conceptual understanding of damage mechanisms in composite impacts to reconstruct damage information that is missed by this scanning. Several authors have identified composite damage mechanisms that connect matrix cracking in plies with delaminations at interfaces, most notably that fiber-parallel matrix cracking creates boundaries for delamination and bridge between delaminations in neighboring interfaces [9, 10, 39, 43]. Previous UT research has focused on developing models and abstractions of the damage state to avoid this limitation. Craven et al. [18] presented a peanut shaped delamination model based on the ply directions in each layer. Suemasu et al. [17, 44] presented a double spiral damage model based on interactions of fiber cracking and delaminations and the regularity of most quasi-isotropic layups. Long [46] presented a model based on the directions of plies adjacent to an interface. As an alternative approach, this paper seeks to limit damage model assumptions by using information about delamination and matrix crack information with partial UT data. By combining the ply-by-ply layup orientation, partial data from shadowed UT pulse-echo scans can be extended by assumptions of the relationship between delamination shapes and matrix crack locations and directions. This extension method is compared with segmented 3D X-ray computed tomography (CT) results [39] which provide a 3D characterization of the damage structure without suffering from shadowing effects, but which requires more elaborate equipment that prevents field application [25].

4.10 UT SCAN SEGMENTATION

UT C-scans were segmented into interface-by-interface delaminations using precise gating of each single-point A-scan. The initial reflection seen in every point scan was carefully fit so that it could be distinguished from reflections off of very shallow delaminations, and the resulting time-of-flight (TOF) difference from this first reflection's peak and the peak of the second reflection was used to determine the depth of damage compared to the reflection off the back face in an undamaged region. Point A-scans from the LV-162 specimen at an undamaged and damaged location are shown in Figure 4.27. Figure 4.27a shows the full UT TOF C-scan with the location of the undamaged and damaged point scan locations marked (see Figure 4.27b and Figure 4.27c respectively). The results were then segmented into interface-by-interface damage maps by dividing the depth into the known number of interfaces and grouping reflections by their closest interface. The results of this segmentation are color coded and shown for the LV-162 specimen in Figure 4.28a and for the LV-059 specimen in Figure 4.28c. For each interface, the segmented damage map is represented as a grid of pixels that indicate at each scan location whether damage was detected at each interface. It is important to note that at each location only one delamination can accurately be detected due to the aforementioned shadowing. The projected delamination from this segmentation is compared with projected delamination from the CT segmentation [39] in Figure 4.28b for specimen LV162 and Figure 4.28d for specimen LV-059, and the overall delamination areas are compared in Figure 4.29. Figure 4.28a and Figure 4.28c results are much smoother than Figure 4.28b and Figure 4.28d due to the large difference in scan resolution (CT results are much finer).

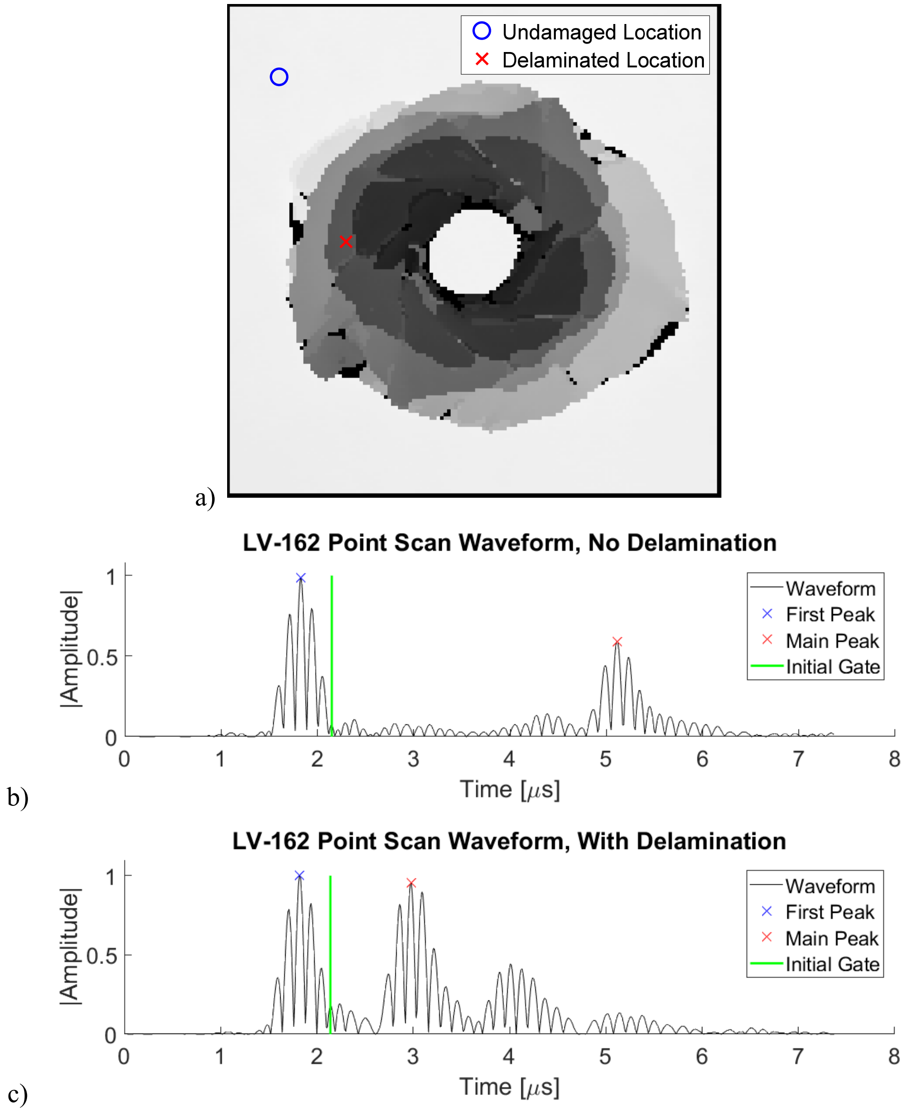

Figure 4.27. a) UT scan showing TOF at each location and markers for the point scan locations in b) and c). b) Point scan results at a location with no delamination damage showing a reflection from the back surface. c) Point scan results at a location with delamination damage. Both scans show the gating selections to distinguish the always present first peak and the peak corresponding to reflection from the back face or damage.

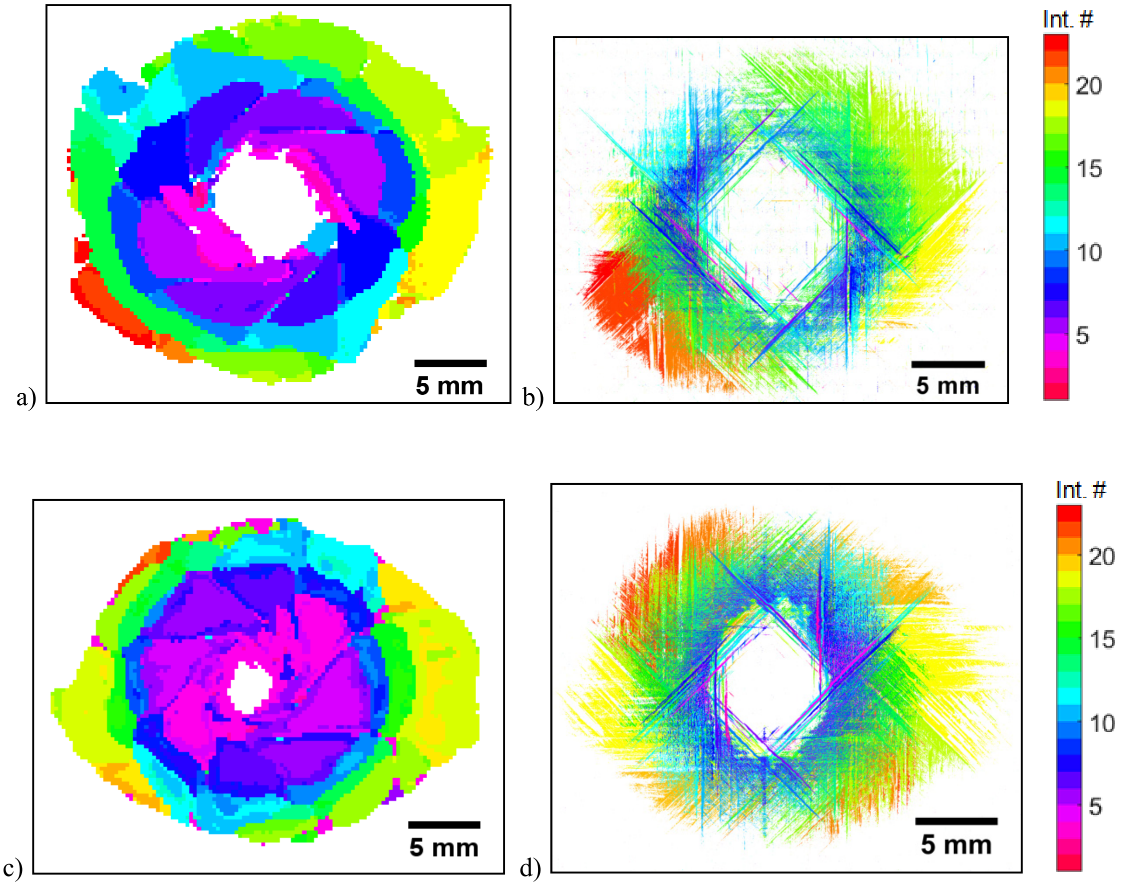

Figure 4.28. Projected color coded delaminations from the segmentations of: a) the UT segmentation for specimen LV-162, b) the CT segmentation for specimen LV-162, c) the UT segmentation for specimen LV-059, and d) the CT segmentation for specimen LV-059. UT scan resolution is 0.25 mm per pixel and CT scan resolution is 0.014 mm per pixel. Lower interface numbers refer to interfaces closer to the impact side.

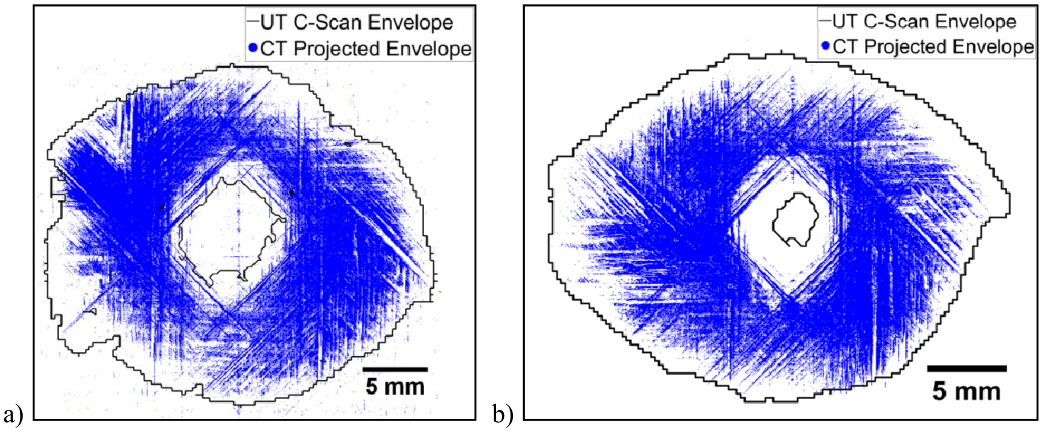

Figure 4.29. Comparison of overall delamination between the CT and UT scan results a) for specimen LV-162 and b) for specimen LV-059. CT results are shown as blue pixels and the UT results are shown as an overall black envelope. The CT delamination extent is slightly smaller than the UT envelope due to potential CT resolution limitations [39].

Overall comparison in Figure 4.29 shows that the results of both methods agree on the shape of the combined multiple planes of delamination damage for the two specimens, but that the CT results predict a slightly smaller delamination area due to potential CT resolution constraints [39]. Direct comparisons of delamination results from UT and CT segmentations are shown for a shallow interface in Figure 4.30a and for a deeper interface in Figure 4.30b for specimen LV-162 (increasing interface number is located further from impact-side). UT results from the shallower interface generally agree well with CT scan results in shape and size. However, for the deeper interface, the UT results only capture a portion of the damage found in the CT results due to shadowing of deep delaminations under shallower delaminations. For a visual interpretation of shadowing, Figure 4.31 shows UT segmentations for individual interfaces in the LV-162 specimen with dark regions indicating the potential areas in which the UT results have been shadowed by shallower-depth delaminations (i.e., black regions are the projection of all shallower-depth delaminations above this current interface). These dark regions compose the maximum envelope in which the shadowed delamination area can exist. In this section, lower ply numbers indicate plies closer to the impact face.

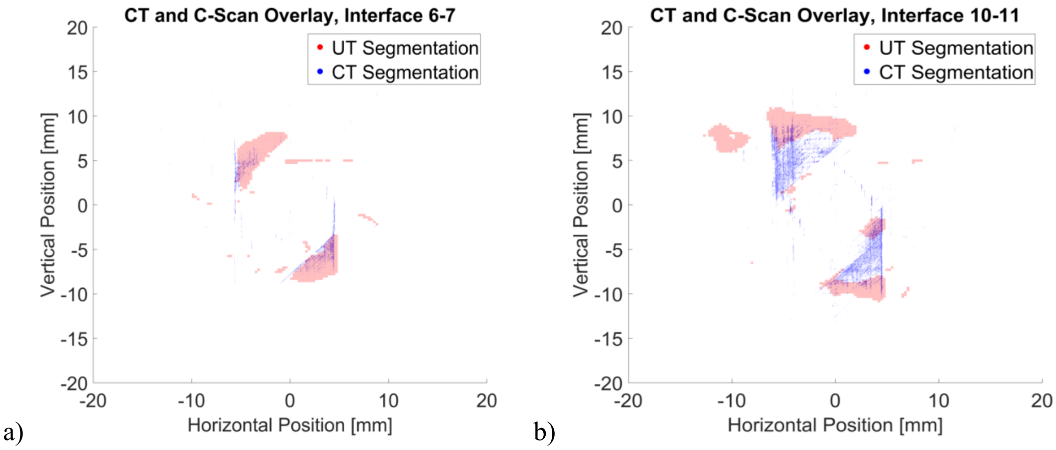

Figure 4.30. a) Shallow interface showing a good agreement between the CT and UT delamination extents b) Deep interface showing a loss of delamination information in the UT segmentation due to shadowing. Lower ply numbers are closer to the impact side.

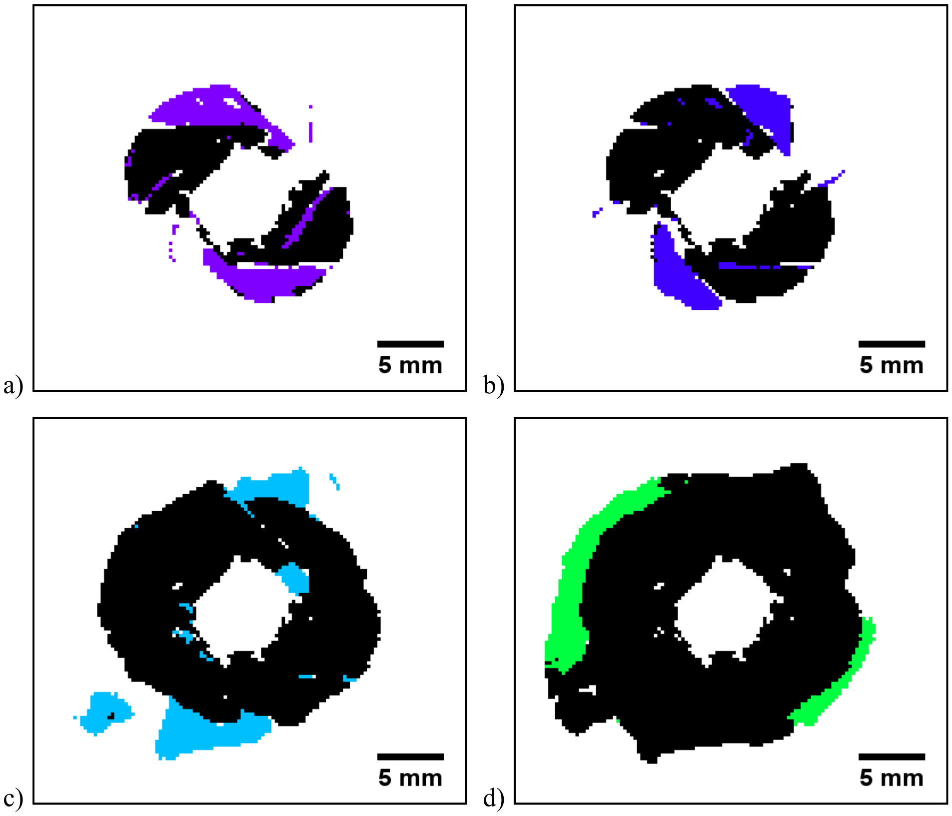

Figure 4.31. Potential shadowed regions shown in black and UT results shown in color for the interfaces between a) plies 5-6, b) plies 6-7, c) plies 10-11, d) plies 14-15.

4.11 UT Extension Method

Because UT C-scans are subjected to shadowing effects where shallow depth delaminations make detection of deeper delaminations more difficult, some information about the delamination state is lost. In order to recover this lost information, an understanding of the composite damage state can be applied to predict the missing (shadowed) delamination area. Based on previous researchers' work on composite damage under impact [9, 10, 39, 43], relationships between the ply directions at the interfaces and delaminations can be made. Figure 4.32 shows damage maps taken from a CT scan of the LV-162 specimen at two plies and the interface in between them with an overlay of these three damage maps showing the clear connection between the matrix crack locations and directions and the delaminated area. Ply damage in the 45° and 90° plies can be clearly observed as a boundary for the delamination between the plies. This suggests that information about ply directions adjacent to each interface can provide insight into the delamination state.

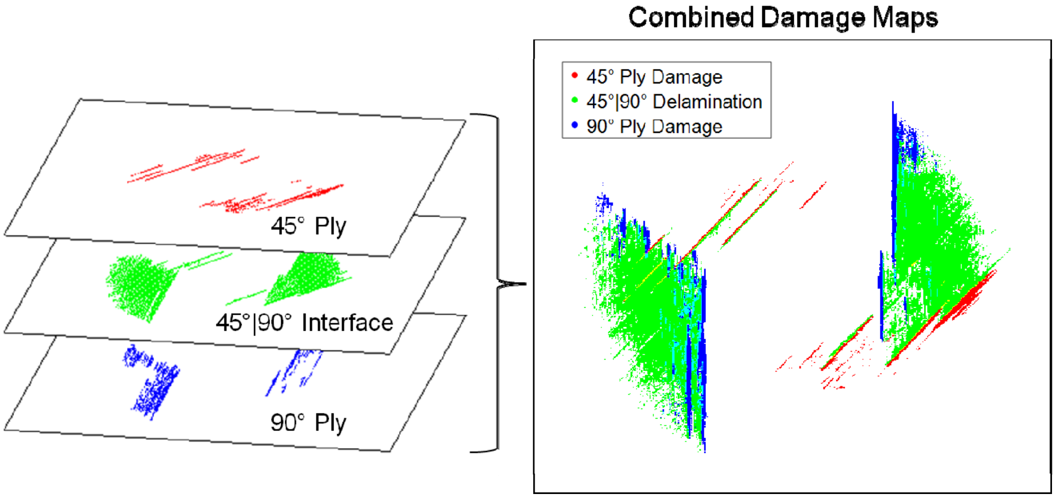

Figure 4.32. CT damage map overlay showing the bounding interaction between delaminations (green) and matrix cracking in adjacent plies (red and blue) for specimen LV-162.

To extend the interface delamination maps from the UT C-scan segmentation, a bounding line fit procedure has been developed based on the ply directions surrounding the interface. The extension procedure consists of the following main steps: a) the delamination area from the UT segmentation for the current interface is converted from areas of damage to boundaries (outlines) of connected damage as shown in Figure 4.33a. The boundaries are then filtered by size to prevent extending too small of a partial delamination area as small areas may be due to UT segmentation issues/noise and would not likely provide meaningful partial delamination information. The minimum size parameter is user selected and should be chosen based on the UT scan resolution and the expected damage area. For these scans, the minimum area to extend a partial delamination was set as 2 mm^2. The two largest boundaries are then selected because the delamination usually consists of two major delamination lobes. b) For each of the two major delamination boundaries, lines corresponding to the fiber directions of the plies surrounding the interface are fit to be tangent to the outer edges of the boundary. For example, in the case of 90° fitting lines, the two bounding lines are the furthest left and right lines that still intersect the delamination boundary as shown in Figure 4.33b for the interface between plies 11-12. c) In order to extract the desired delamination extension, the triangle that is formed by the bounding lines is selected, such as is shown in Figure 4.33c. d) The chosen triangle area is then added to the partial delamination area by combining the area within the extension triangle with the original partial area to create a new damage map for that interface (Figure 4.33d). e) The new damage map is then intersected with the potential shadowing region for that interface as shown in Figure 4.33e. This prevents the extension from falsely predicting delamination that would not have been shadowed. Because the shallower interfaces do not experience significant shadowing, the extension method was applied only to interfaces at least four plies deep as the somewhat regular delamination patterns created by the quasi-isotropic layup begin to overlap below one repeating unit of the layup (i.e., $[0/45/90/\text{-}45]_{3s}$). Additionally, because plies of the same orientation do not delaminate from each other, the extension method is not applied to the middle interface where there are two adjacent -45° plies.

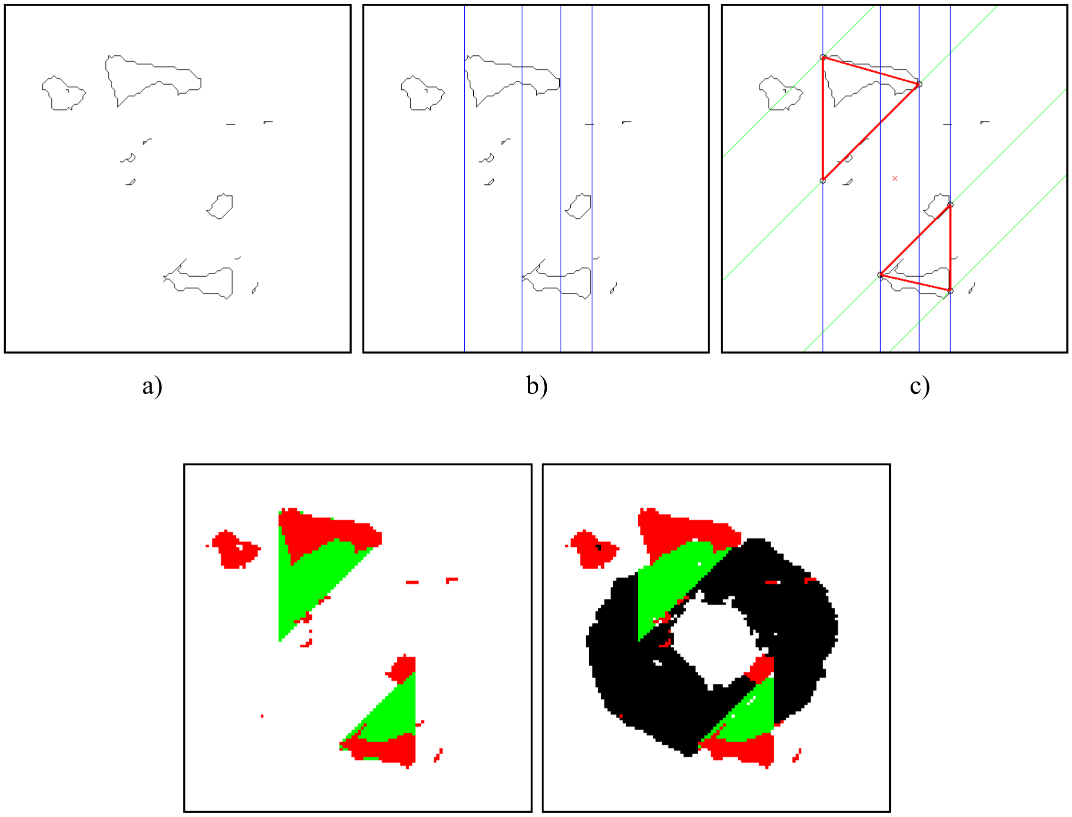

a) b) c)

d) e)

Figure 4.33. Bounding line fit of the UT segmentation area based on the directions of the plies surrounding the interface. a) Delamination area converted into connected region boundaries. b) Delamination fit with the first ply direction lines at 90° in this example. c) The closest triangle to the center of the damage is taken from the diamond formed by the bounding lines. d) The extended delamination (green) is added to the original partial delamination (red). e) The extended results are intersected with the shadow region to produce the final extension.

4.12 UT EXTENSION RESULTS

Comparisons between the delamination area from the CT segmentation and the extended UT segmentation are shown for specimen LV-162 for each extended interface in Figure 4.34. To compare the two results, the overall delamination extents are aligned and the resolutions of the two scan types (0.014 mm per point for CT and 0.25 mm per point for UT) are used to appropriately scale the results to each other. In each image, blue regions indicate damage at that interface detected by the CT segmentation, red regions indicate delamination detected at that interface in the UT segmentation, and green regions indicate new damage area that is predicted by the UT extension method. In the comparison, the red regions of the UT results generally show only a partial delamination as compared to the CT results due to shadowing of the original UT scan. Some interfaces in the extension show a recovery of most of the lost delamination information, but other interfaces may have only partial recovery or completely miss the delamination seen in the CT segmentation. This is due to a complete shadowing of the delamination information at those interfaces effectively preventing any extension of partial delamination (i.e., no starting area as in Figure 4.33a). Potential issues with this extension method are discussed further in Section 4.8 section. A summary of the damage area as calculated by the UT segmentation, the UT extension, and the CT segmentation for specimen LV-162 is illustrated by a bar chart in Figure 4.34. CT damage area was measured manually from the segmented results. Similarly, comparisons of results at each interface are also shown for specimen LV-059 in Figure 4.35. Results for this specimen show more noise in the UT segmentation, but still show good agreement with the CT delamination area after application of the extension method. A summary of the damage area as calculated by the UT segmentation, the UT extension, and the CT segmentation for specimen LV-059 is illustrated by a bar chart in

Figure 4.36. CT damage area was measured manually from the segmented results. Overall, for specimen LV-162 the original damage area from the UT scan was 512 mm^2 and the total damage area after extension was 1045 mm^2 compared with the CT total damage area of 1102 mm^2, and for specimen LV-059 the original damage area from the UT scan was 452 mm^2 and the total damage area after extension was 860 mm^2 compared with the CT total damage area of 1072 mm^2.

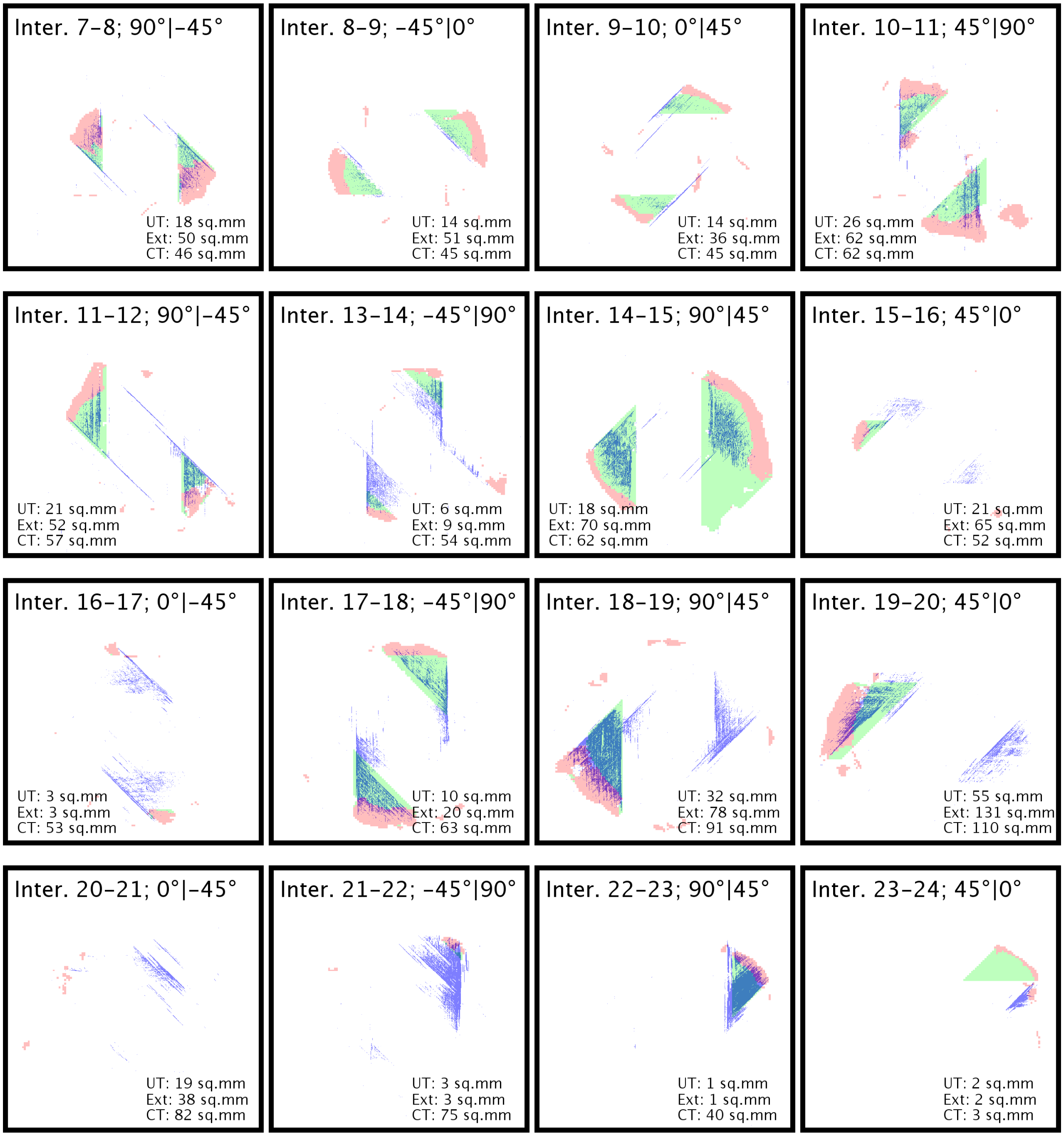

Figure 4.34. Comparison of CT detected delamination and UT extended delamination at all extended interfaces for specimen LV-162. Red regions indicate where damage was found in the original UT segmentation, green regions are damage regions that have been added by the extension method, and blue regions are regions where damage was detected in the CT segmentation. Ply angles are given with respect to a horizontal 0° axis. Damage areas are shown for each interface as measured from the UT base segmentation (UT), the UT base combined with the extension results (Ext), and the CT segmentation (CT).

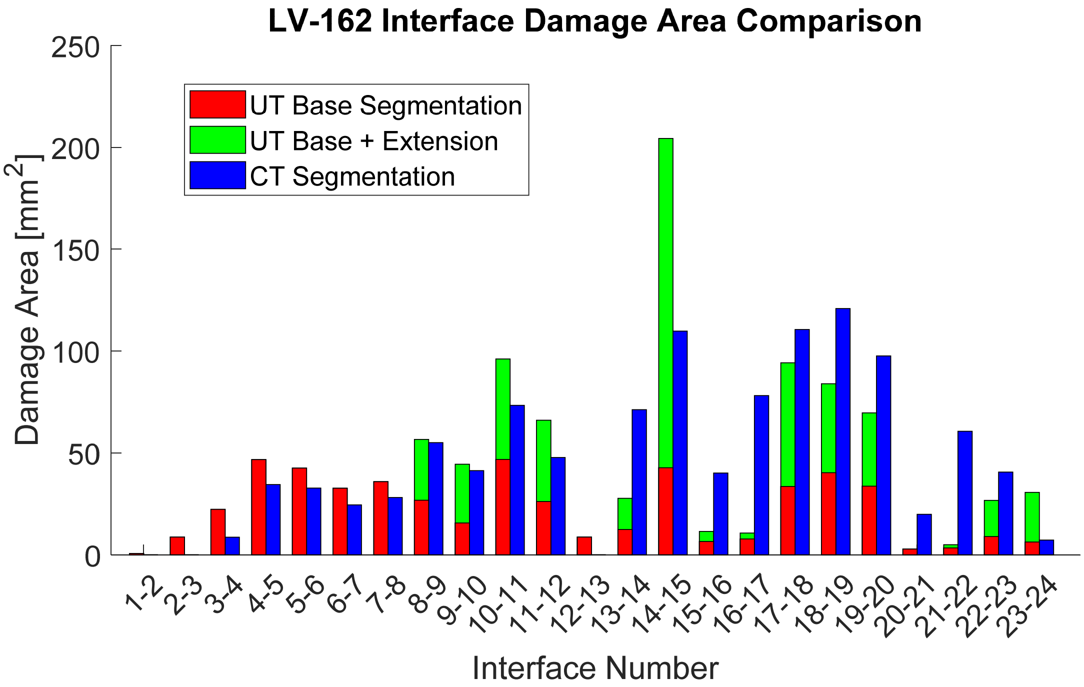

Figure 4.35. Bar chart comparison of interface-by-interface damage area for specimen LV-162 between the UT base damage area with the extended damage area and the CT segmentation damage area. Interface number refers to the ply numbers surrounding the interface with lower ply numbers being closer to the impact side.

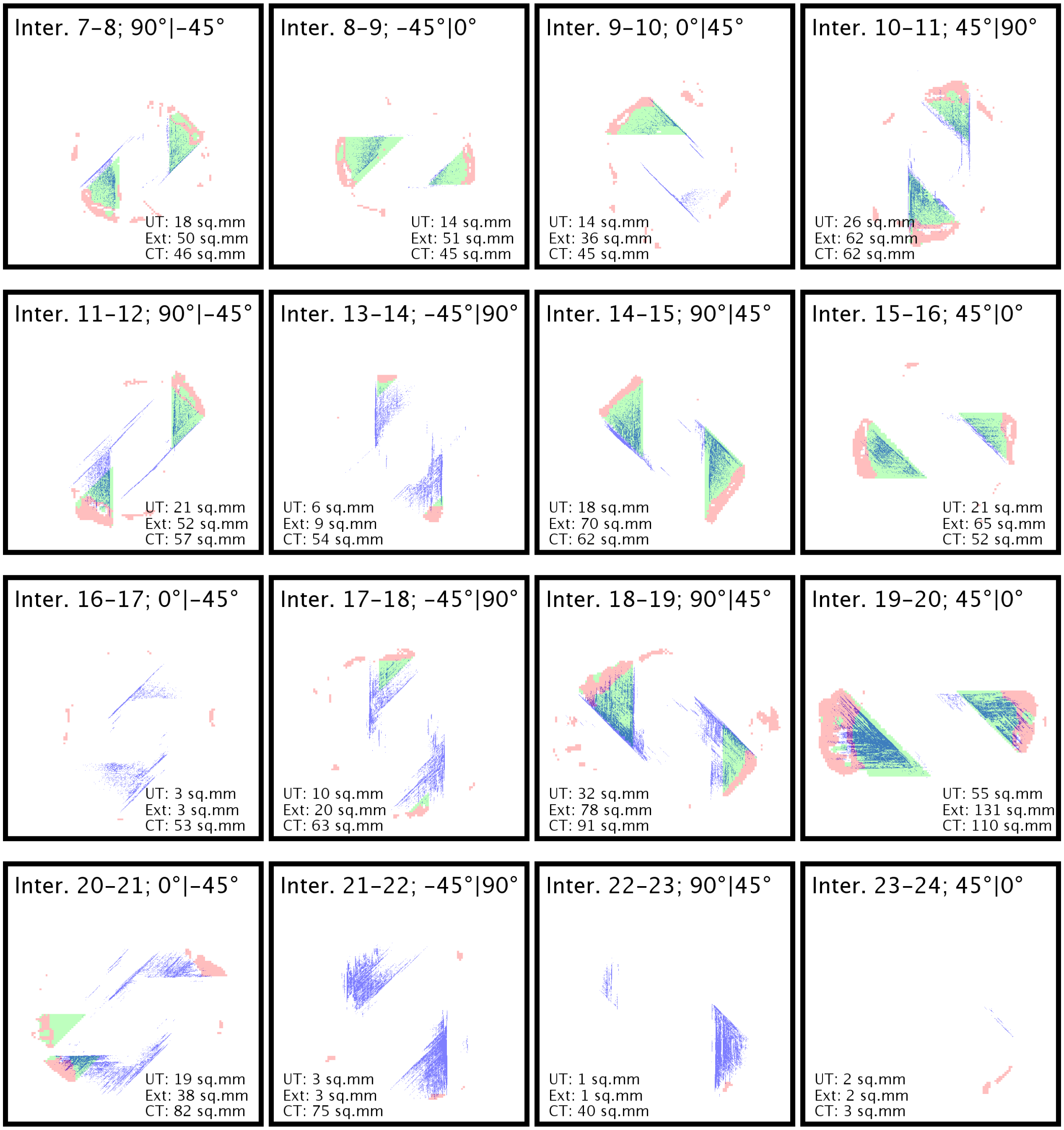

Figure 4.36. Comparison of CT detected delamination and UT extended delamination at all extended interfaces for specimen LV-059. Red regions indicate where damage was found in the original UT segmentation, green regions are damage regions that have been added by the extension method, and blue regions are regions where damage was detected in the CT segmentation. Ply angles are given with respect to a horizontal 0° axis. Damage areas are shown for each interface as measured from the UT base segmentation (UT), the UT base combined with the extension results (Ext), and the CT segmentation (CT).

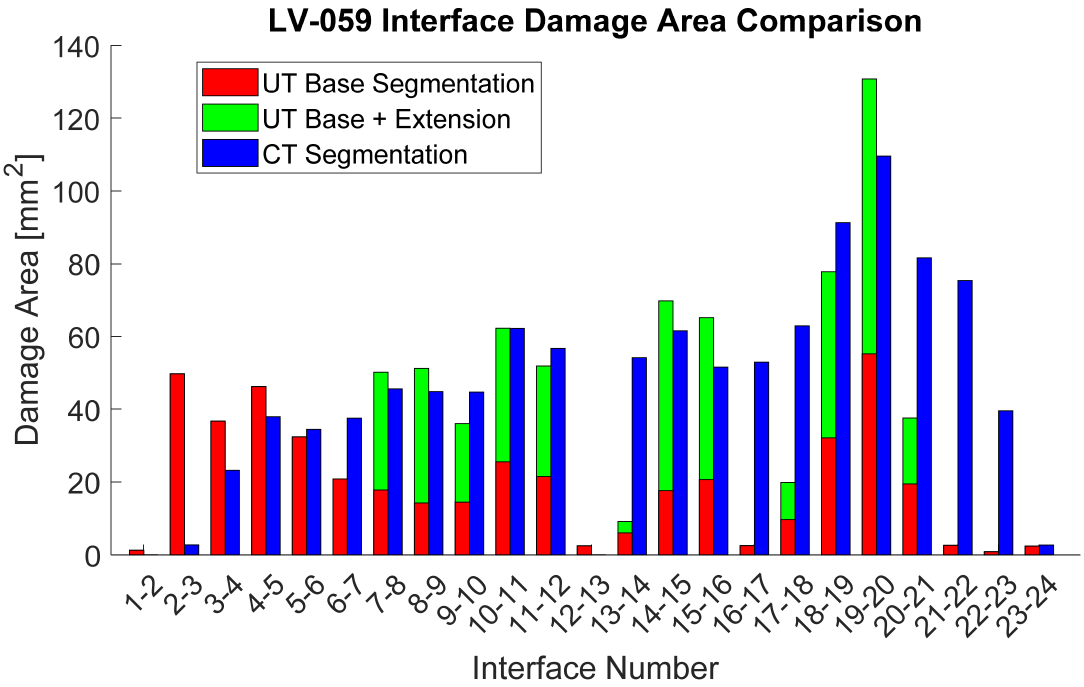

Figure 4.37. Bar chart comparison of interface-by-interface damage area for specimen LV-059 between the UT base damage area with the extended damage area and the CT segmentation damage area. Interface number refers to the ply numbers surrounding the interface with lower ply numbers being closer to the impact side.

The overlaid results from the extended UT segmentation and CT damage maps can be stacked together and re-sliced into through-thickness section views to examine how the extension method recovers hidden delaminations. Figure 4.38b shows one specific slice of the results taken from the section highlighted in Figure 4.38a with red indicating damage from the original UT segmentation, green indicating damage added by the extension, and blue indicating damage in the CT segmentation. This figure is similar to a line scan/B-scan in that it shows the variation of damage depth through the thickness. Each vertical line represents damage at some interface with the top of the figure showing shallower interfaces and the bottom showing deeper interfaces. This image shows how the originally missing distribution of damage from the UT segmentation is filled in by the extension method to more closely resemble the CT results. However, this figure also shows that for some interfaces not enough partial information was present to enable extension of the UT data.

The results can also be interpreted in 3D by visualizing the delamination distribution through the thickness. This view more clearly shows how the extension method fills in the missing interior damage information. 3D visualizations for the UT segmentation extension and the CT segmentation are shown in Figure 4.39. UT results were visualized in this way by creating a set of color coded ply layers and then inserting delaminations as planes of connected sets of interface damage. To distinguish between damage from the original UT segmentation and damage from the extension method, damage from the extension method is shown as darker regions in the 3D figure. CT results were visualized in 3D by searching for connected regions of pixels that were marked as damage and using a planar best fit to generate the simplified delamination. The extended UT segmentation in Figure 4.39a shows how the extension method fills in some of this missing information to create a more full 3D prediction of the damage state. This extension shows a generally good agreement with the CT results in Figure 4.39b, but misses some delaminations due to a lack of initial information.

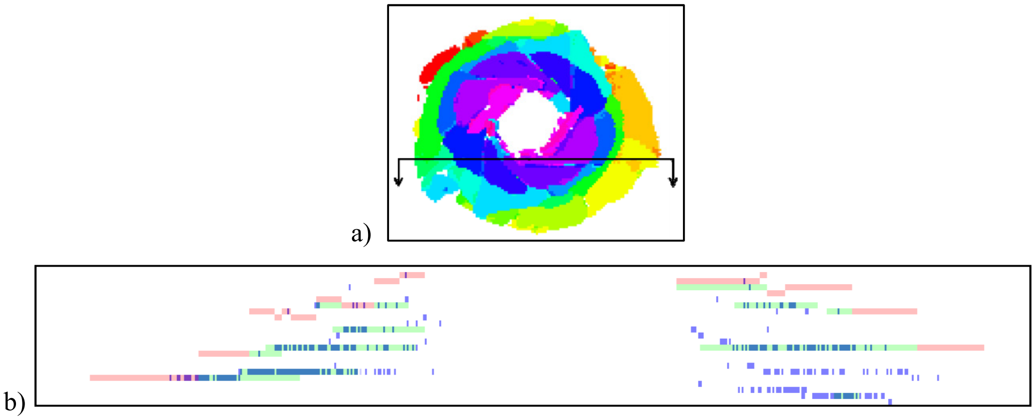

Figure 4.38. a) Full UT segmentation showing the through-thickness slice location for specimen LV-162. b) Through-thickness slice of the overlay of the UT and CT segmentations. Red regions show interfaces where delamination was detected by the original, green regions show delaminations predicted by the extension method, and blue regions show where delamination was detected in the CT segmentation.

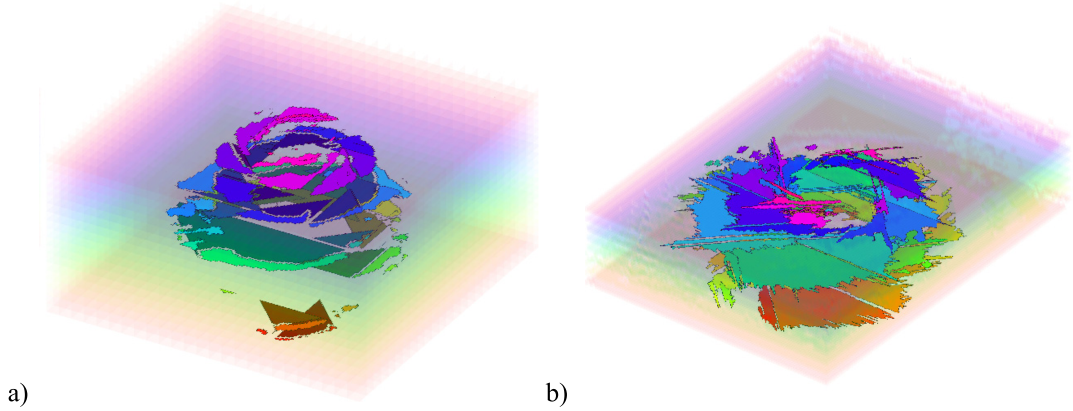

Figure 4.39. 3D comparisons for specimen LV-162 of the a) UT extended segmentation with darker colors for the extended portion, b) CT segmentation.

Matrix damage can be estimated from this extension method despite the difficulty in characterizing intraply cracks of this UT method (single transducer perpendicular incidence scanning) by taking the bounding lines of the extension and identifying these as matrix cracks in the plies above and below the interface. In each ply, the bounding lines corresponding to the ply's fiber direction in the two interfaces adjacent to the ply are converted to a series of pixels corresponding to the UT scan resolution. Figure 4.40 shows the matrix damage predicted by the extension method for three interfaces where the thin lines extended from the partial delamination indicate damage in the plies adjacent to the interface. Figure 4.41 shows matrix damage for plies 10 (Figure 4.41a) and 11 (Figure 4.41b) from this method corresponding to the matrix damage predicted in Figure 4.40. The cracks in ply 10 are taken from the extension at interfaces 9-10 and 10-11, and the cracks in ply 11 are taken from interfaces 10-11 and 11-12. The matrix cracks are shown as pairs of tightly grouped parallel cracks, which correspond to a slight offset between the delamination extensions at adjacent interfaces. However, it is easy to visually identify these close cracks as one region of ply damage. Although the matrix cracks in plies sometimes extend further than the delamination at the interfaces, this extension method is only capable of predicting the cracks connected to the delaminations, thus this matrix damage prediction captures the location and direction of matrix cracking, but may under- predict the crack length.

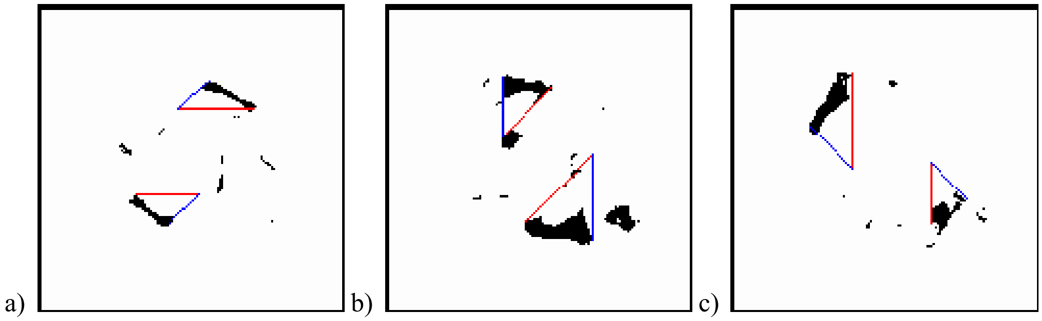

Figure 4.40. Matrix damage calculated from the extension method for specimen LV-162. a) Matrix damage predictions from the extension on interface 9-10, b) matrix damage predictions from interface 10-11, and c) matrix damage predictions from interface 11-12. Red lines indicate damage in the ply above the interface, and blue indicates damage in the ply below the interface.

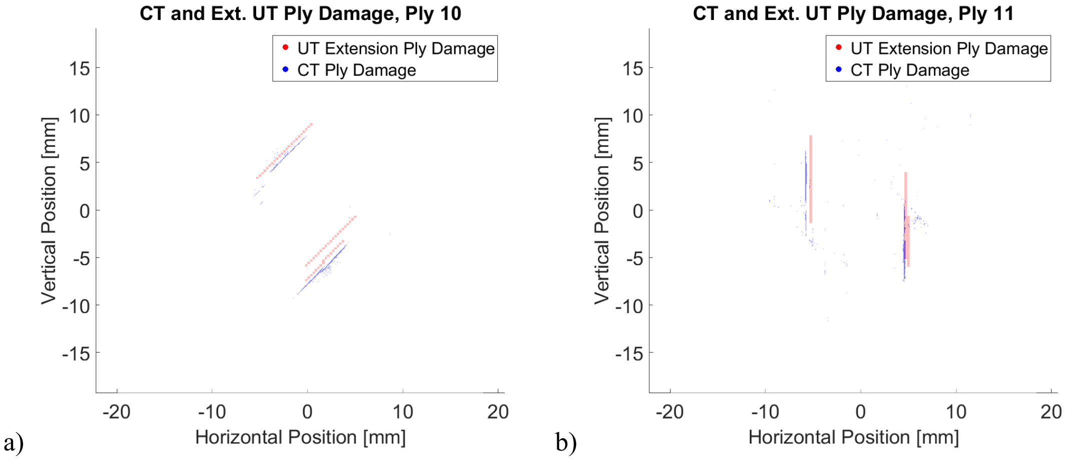

Figure 4.41. Matrix damage for specimen LV-162 for a) ply 10, b) ply 11 as determined from the bounding line fits compared with the CT damage for that ply. Results have been converted from line information to pixelated binary damage information based on the UT resolution.

4.13 UT EXTENSION DISCUSSION

Because this is an extension based on partial information, this method has a few important drawbacks and limitations. Firstly, this method cannot predict delaminations in interfaces that fall completely within the shadowed region. Figure 4.42 shows the interface between plies 18-19 in specimen LV-162 where the entire left delamination lobe is missed by the extension. Additionally, the inner portion of the right delamination lobe is missed due to a lack of information in that particular region. Quantitative comparison between the extended results and the CT segmentation, as shown in Figure 4.35, shows that for this interface the extension only provides a ~50% recovery of the shadowed interface damage. This method is also subject to compounding the errors of the UT segmentation as shown in the interface between plies 20-21 in specimen LV-059 as shown in Figure 4.43. This interface shows the extension applied to erroneous partial information, where the partial information actually fits better in the interface between plies 19-20. This issue is likely caused by a lack of through-thickness resolution of the UT transducer used because the segmentation procedure has to group damage to interfaces by the TOF of the UT wave, and without appropriate UT resolution the TOF between two adjacent interfaces cannot be effectively distinguished.

Additionally, this method cannot currently capture some of the more complicated behaviors that occur near the laminate's mid-plane due to symmetry. Figure 4.44a shows a CT damage map for interface 14-15 between 45° and 90° plies which contains a delamination that does not seem to follow the assumptions about bounding matrix cracking. The left delamination lobe contains a -45° dominant direction that is seeded by the cracking behavior in the -45° plies at the symmetry plane plies. This results in the extension method looking for 45° cracks and over-predicting the delamination as shown in the comparison in Figure 4.44b. Because this behavior does not occur symmetrically about the impact center and is not seen in the similar LV-059 specimen, it is difficult to accurately predict, but with visual inspection this extension result could be identified as anomalous due to its irregular shape and size relative to other extension results as illustrated by the anomalous area shown for the interface between 14-15 in Figure 4.35.

This method attempts to predict missing damage information by extending partial damage found by UT scanning, in contrast to other model approaches in the literature [17, 18] that approximate the damage based on an assumed pattern of delamination shapes through the thickness. Because this approach is based on segmented data at each interface, it can lead to more accurate predictions of delamination at interfaces with sufficient UT data, but may also miss delaminations entirely due to lack of data at particular shadowed interfaces, which the patterned approaches would otherwise predict. Additionally, this approach has only been applied to laminates which have 45° angle changes between adjacent plies and may not be directly applicable to laminates which contain other angles between plies (such as 60° and 90° changes).

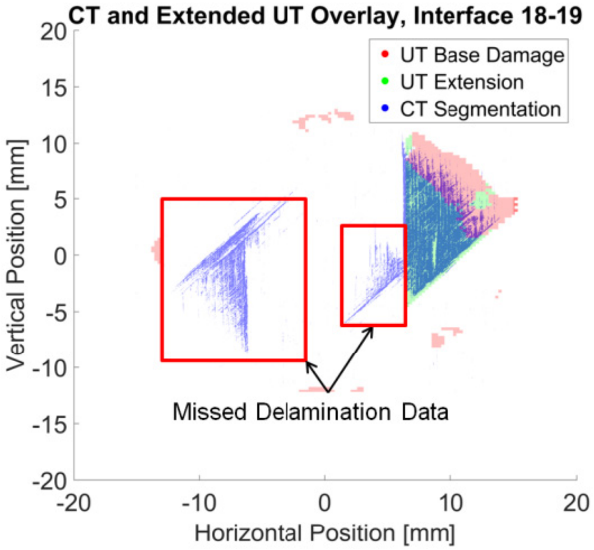

Figure 4.42. Comparison of extended UT results with CT results for LV-162 the interface between plies 18-19. Although the extension captures most of the shadowed delamination for the right delamination lobe, completely shadowed portions from the UT segmentation prevent the extension method from capturing any of the left and central delaminations.

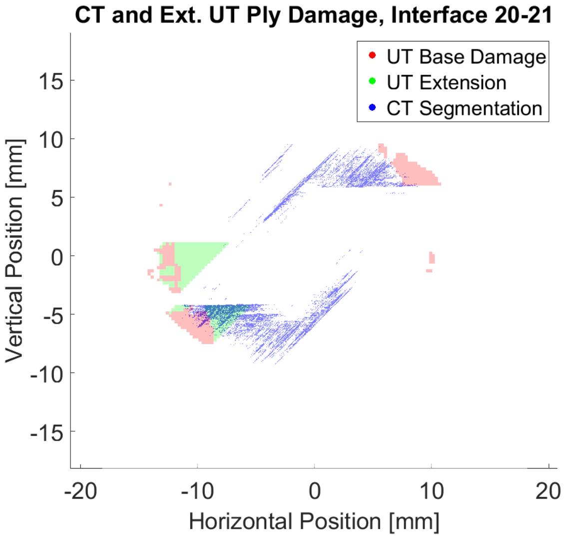

Figure 4.43. Overlay of the UT extension results and the CT results for the interface between plies 20-21 in specimen LV-059. For this result, the erroneous extension is likely due to errors in the UT segmentation that assign damage from adjacent interfaces to these interface.

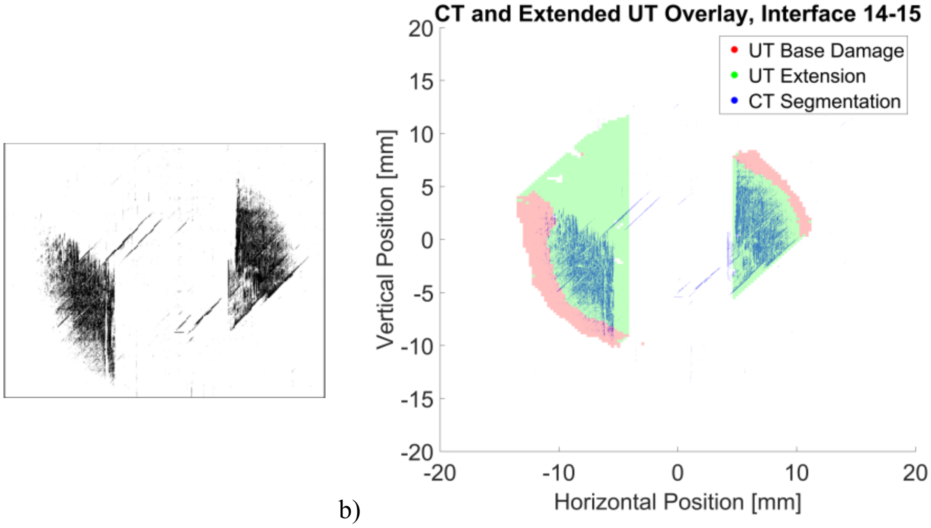

a) b)

Figure 4.44. a) CT delamination map for interface 14-15 in specimen LV-162 between a 45° and a 90° ply. b) Comparison of extended UT to CT data at this interface showing over prediction of the left delamination due to -45° dominant behavior seen in the CT data, but not predicted by the extension method.

4.14 STRINGER FLANGE IMPACT NDE ANALYSIS

Because of the relative difficulty in CT scanning of the flange impacted specimens, only one high-quality CT scan was taken for this type of specimen of the cutout damage specimen S4F1. This scan was segmented by adapting the flat panel segmentation technique and assuming that the 33 ply laminate of the skin-flange zone was the only region of interest. This provided reasonable results in this zone, but gave inaccurate results near the flange taper. Figure 4.45 shows the projected delamination as characterized by the CT segmentation for specimen S4F1. The broad colored region corresponds to the major disbond between the skin and the stringer flange and the smaller patches near the bottom of the image correspond to delamination and matrix cracking detected in the flange laminate.

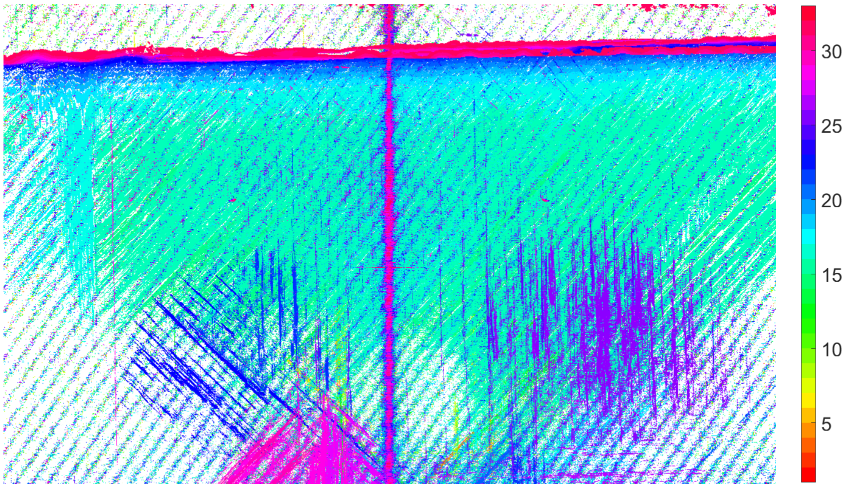

Figure 4.45. Color coded delamination map from the CT segmentation for specimen S4F1. Color bar values indicate the interface number with lower values being closer to the impact surface.

Because of the lack of clear CT data for these specimens, UT scan analysis provided the best damage characterization for these impacts. The TOF UT map for specimen S4F2 is shown in Figure 4.46a where the white region corresponds to a region of no damage in the skin, flange, or interface between them. Medium gray regions above and below the central flange region correspond to undamaged skin laminate. The total region of damage is seen as a roughly trapezoidal disbond between the skin and flange seen as medium gray in the TOF map. In order to convert this UT scan into composite laminate damage information, a basic segmentation was performed based on the TOF and the assumption that a disbond between the skin and stringer would occur at middle TOF values. The region of damage was identified and the damage state was separated into three parts as shown in Figure 4.46b. TOF values in the damaged region were compared with the average TOF observed in the white undamaged flange region. TOF values below half of the pristine TOF were marked in red and correspond to delaminations detected in the skin laminate. TOF values near half of the pristine TOF were marked in green and correspond with the disbond between the skin and stringer flange. Lastly, TOF greater than half but still less than the full pristine TOF were marked in blue and correspond with damage in the flange laminate. Because one of the primary damage modes of this type of single stringer compression specimen is disbond growth due to post-buckling deformation, this characterization of the major disbond was considered the most important aspect of the damage state. For a better geometric interpretation of the damage state as segmented here, Figure 4.47 shows the color coded UT results within a computer aided design (CAD) model of the stringer specimen geometry. The major disbond is roughly trapezoidal with the major leg along the end of the stringer flange.

a) b)

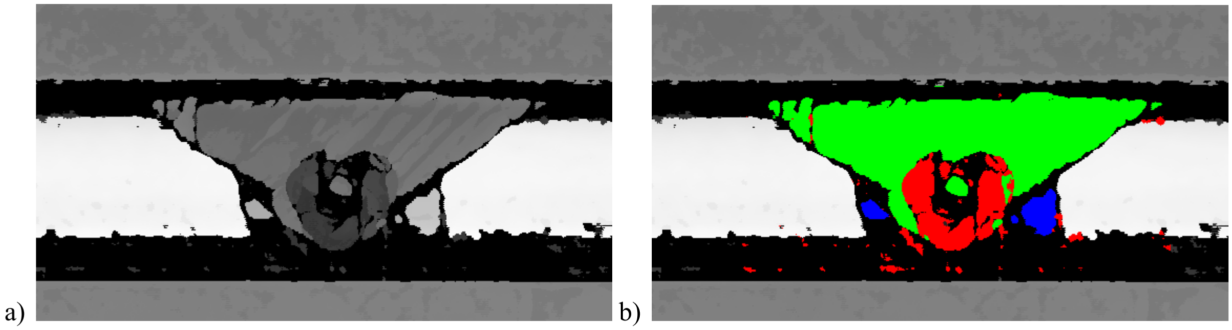

Figure 4.46. a) Time of flight UT map and b) color coded TOF UT map for specimen S4F2. Red indicates damage within the skin laminate, green indicates disbond between skin and stringer flange, and blue indicates damage in the flange laminate.

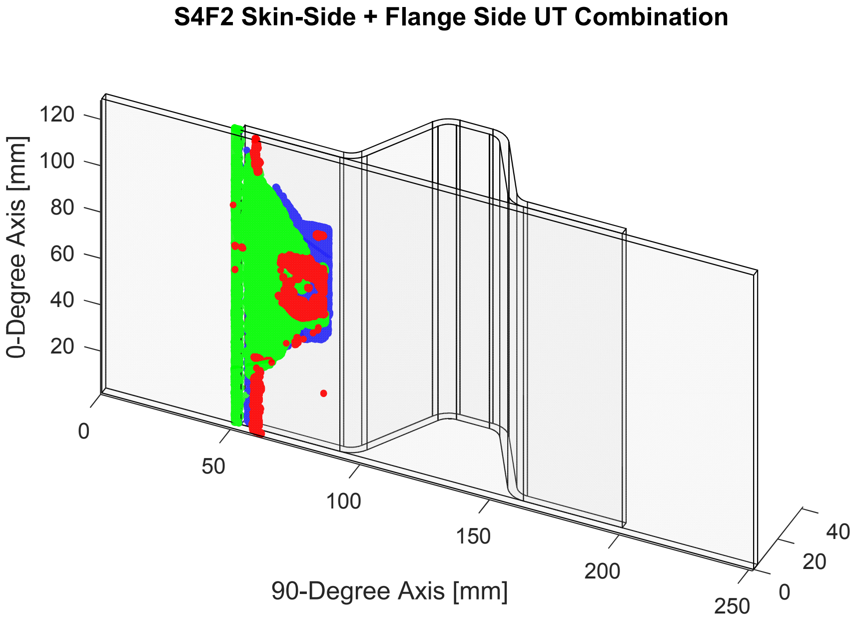

Figure 4.47. 3D visualization of the segmented UT scan damage state within a CAD representation of the stringer specimen.

4.15 NOTES/ACKNOWLEDGEMENTS

Chapter 4 is, in part, an edited version of work that had previously appeared in:

Ellison, A., & Kim, H. (2018). Computed tomography informed composite damage state model generation. *Journal of Composite Materials*, *52*(25), 3523–3538. https://doi.org/10.1177/0021998318773464. The author of this dissertation was the primary investigator and author of this study.

Ellison, A., & Kim, H. (2019). Shadowed delamination area estimation in ultrasonic C-scans of impacted composites validated by X-ray CT. *Journal of Composite Materials*. SAGE Publications Ltd. https://doi.org/10.1177/0021998319865311. The author of this dissertation was the primary investigator and author of this study.

Ellison, A., & Kim, H. (2019). Automated Computed Tomography Segmentation of Impact- Damaged Curved Composite Structures. DEStech Publications. https://doi.org/10.12783/asc34/31260. The author of this dissertation was the primary investigator and author of this study.

These works were supported under the NASA Advanced Composites Project No. 15-ACP1-0021.

5 RESIDUAL STRENGTH MODELING

This chapter presents methodologies for interpreting NDE detected damage as a tool for model validation and as a model-able damage state for residual strength analyses. The first section of this chapter presents a comparison between an impact model and CT segmented damage to verify the physical nature of the model damage predictions. The rest of the chapter then focuses on approaches to generating finite element analysis (FEA) models of residual strength behavior that incorporate an NDE damage state and comparing results with residual strength test data.

5.1 IMPACT MODEL VALIDATION

This section describes modeling of the impact event on flat panels and correlation of the modeling damage state with CT results.

Finite element models of the flat panel impact case were developed in Abaqus using ply-by-ply modeling. Damage within plies was modeled using the Hashin damage criteria whose Abaqus implementation is described by Camanho and Dávila [47]. Damage between plies was implemented using cohesive surfaces based on the cohesive zone model first proposed in [48] One of the main benefits of advanced NDE imaging such as provided by X-ray CT is the ability to quantify the quality of modeling techniques for predicting damage. With layer-by-layer damage maps it is possible to directly overlay damage results with NDE characterization. This section is focused on utilizing segmented CT results as a model validation tool. The impact modeling discussed in this section was performed by Marco Pigazzini [49].

Impact modeling results in composite materials is often difficult to quantitatively verify due to the complexity of composite damage states such as seen in those shown in Chapter 4. Often, general agreement between overall delamination extent is presented as a verification of composite impact modeling tools. The development of CT as a characterization technique enables a much more direct comparison where impact damage at each interface can be checked against a layered impact model in terms of qualitative shape and quantitative extent.

As part of this collaborative research activity, impact damage models were developed by Pigazzini using a thin-shell Isogeometric Analysis formulation (IGA) as described in [50]. This model utilized Kirchoff-Love shell theory where the shear deformable behavior of the composite laminate is recovered by the deformation of cohesive connections between individual layers. The model geometry is illustrated in Figure 5.1 where the blue zone refers to the region where ply interface cohesive damage was enabled. Each individual ply was modeled with connections between plies modeled as a damageable cohesive zone. The flat panel impact case modeled was the 25 J impact on specimen TC-24-31-2.

Comparisons of the delaminations in the model and the CT segmented results are shown in Figure 5.2. The primary features of interest in the damage comparison are the extent and shapes of the delamination features. In order to verify the performance of an impact model it is important that the model captures the correct extent and also has shapes consistent with the physical development of impact damage in a composite laminate. In particular, as described in Section 4.5, the interaction between delaminations and ply cracking imply that delamination shape be heavily influenced by surrounding ply directions. As seen in Figure 5.2, delaminations predicted by the impact model somewhat over-predict delaminations but based on the shapes of the delaminations, the model generally captures the inherent interaction between matrix cracking and delamination shape. Comparisons of the ply damage of the model and the CT characterization of the matrix damage are shown in Figure 5.3. Matrix cracking comparisons confirm that in general the model is capturing the ply damage in a way that is consistent with the delamination damage state observed.

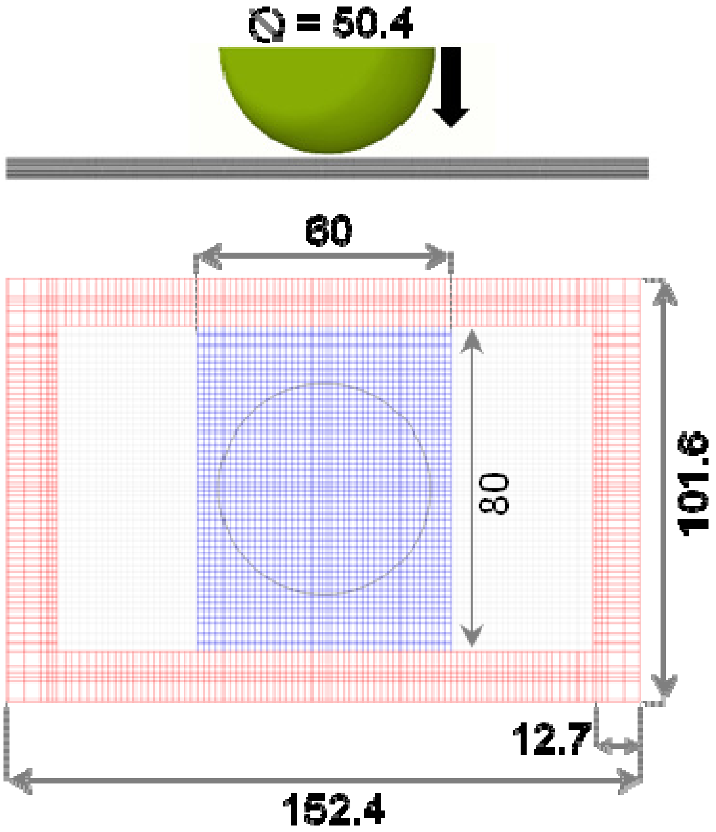

Figure 5.1. IGA model illustration. All dimensions shown are given in millimeters. A more detailed description of the IGA model is given in [50]

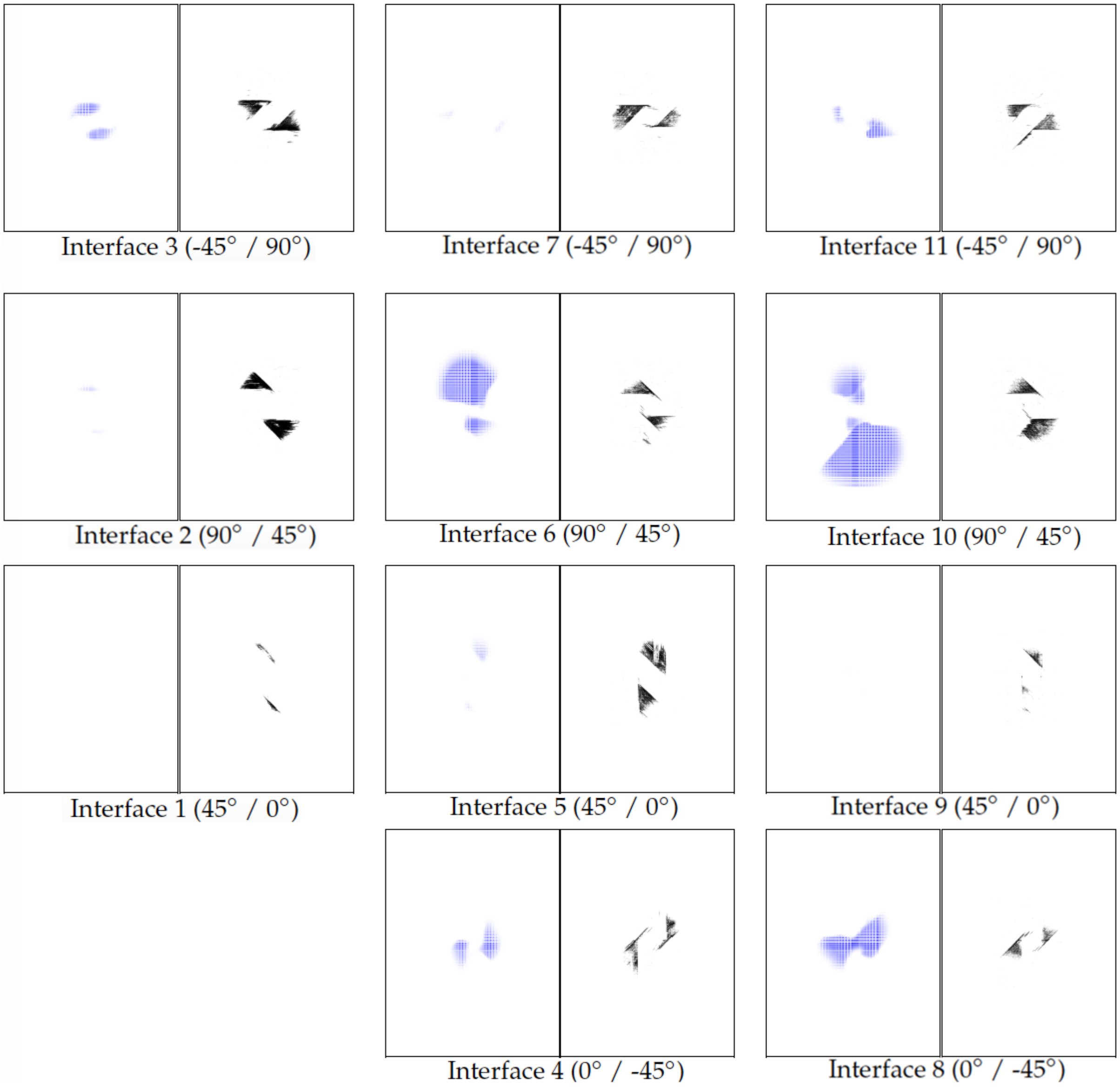

Figure 5.2. Correlation of (right) CT-scan results and (left) Delamination predicted by the IGA simulation for cohesive interfaces 1-11.

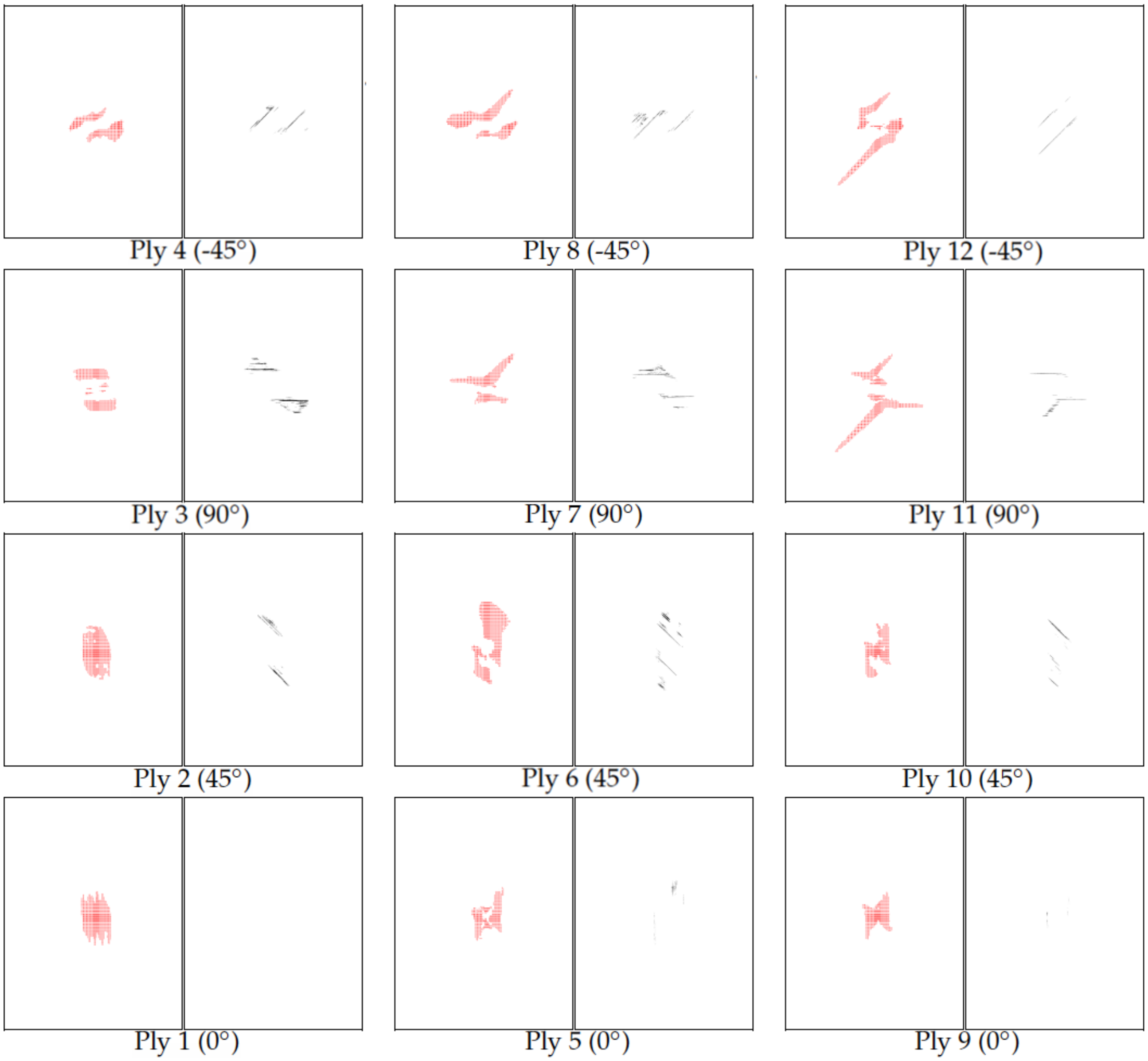
Ply 4 (-45°)
Ply 8 (-45°)
Ply 12 (-45°)
Ply 3 (90°)
Ply 7 (90°)
Ply 11 (90°)
Ply 2 (45°)
Ply 6 (45°)
Ply 10 (45°)
Ply 1 (0°)
Ply 5 (0°)
Ply 9 (0°)

Figure 5.3. Correlation of (right) CT-scan results and (left) Matrix damage predicted by the IGA simulation for plies 1-11.

5.2 PREVIOUS APPROACHES TO MODELING OF NDE DAMAGE STATES

Previous methods for modeling residual strength have generally been limited by the availability of detailed non-destructive evaluation information and have made assumptions about delaminations as either major delaminations for sub-laminate buckling calculations [8, 16], open holes of size relative to the delamination extent [51], or assumptions about delamination shape and through-thickness distribution [18]. Some methods for the implementation of CT data into modeling have been studied, but these methods have been limited to either small scale mesh generation on the order of individual fiber modeling [52], or direct tetrahedral meshing of a CT volume with large voids [53], both of which approaches are likely too fine in detail to create computationally tractable models of larger structures (i.e., a full-scale wing or stringer-stiffened fuselage panel). In terms of applications of data acquired directly from NDE sources to structural level damage, Moura et al. [16] presented a method based on checking the status of interface elements as either in or out of a simplified UT delamination area. Suemasu et al. [17, 44] presented a double spiral damage model based on the usual spiral pattern of impact damage to approximate the damage state for use in a residual strength model. More recently, Action et al. and Flores [19, 53] presented a compression strength after impact methodology for XFEM implementations of X-ray CT and UT data into a residual strength model based on manual segmentation and implementation of damage. However, an understanding of how best to implement an NDE damage state into finite element modeling is not yet established, particularly for application to large structures. The primary unaddressed question is: to what extent does the modeled damage have to physically capture damage behavior and what degree of damage modeling fidelity is required to create an effective modeling correlation. The discussion of modeling presented in this dissertation provides a series of models with varying levels of damage modeling fidelity, and based on the type of problem studied the modeling accuracy is established.

5.3 BASIC CONCEPTS IN MODELING OF AN NDE DAMAGE STATE

This section presents an investigation of damage mapping methods that take into account automated damage states segmented from CT and UT datasets and how such damage states should be implemented into finite element modeling techniques.

The CT-extracted damage zones enable more accurate and detailed representation of damage in models used for assessing damage growth and residual strength. Based on the nature of the developed segmentation results, a potential scheme for implementing the segmented results into numerical modeling is proposed.

For the implementation of delamination, two potential methods may be used depending on how the bonding between plies is modeled: cohesive elements and surface based bonding between nodes or integration points. In the case of cohesive elements, delamination may be implemented by comparing an overlay of the 2D damage map at the interface of interest from CT onto the mesh of cohesive elements representing that interface in the model. Pixels from the damage map are then associated with a pixel area calculated as the square of the CT scan resolution. Elements are marked as damaged if a certain percentage (per user-defined threshold) of the area of the element is covered by damaged pixels based on the CT data. This mapping concept is illustrated in Figure 5.4 where a 1 x 1 mm element mesh is superimposed onto the CT map showing damaged (dark) and undamaged (white) pixels. The right-hand element in Figure 5.4 exceeds a 25% damaged area threshold. Example results of mapping the delamination onto a 1 x 1 mm mesh are shown in Figure 5.5 based on a 25% threshold. A lower threshold would result in a larger set of elements representing delamination, whereas a higher threshold would produce the opposite effect. For bonding between nodes or integration points, a similar method may be used by associating an effective area with each point of interest and marking these points as damaged if enough of the area is covered by damaged pixels from the CT damage map. It is important to note that the physical response of a delamination is highly determined by the type of material system.

This approach was designed to maintain the original orientation and rectilinear shape of the mesh which may be an important consideration for CDM models, but other approaches may be viable that better match the outline of the delamination. Due to the modeling approach of including heavily weakened cohesive zones to represent initial damage states, models that incorporate these types of damage states, may be prohibitively expensive for implicit integration schemes, as the early presence of damage may cause convergence issues. It is for this reason that the models presented in this chapter were exclusively run with explicit integration.

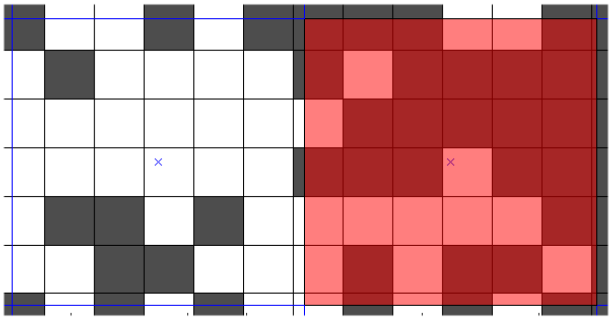

Figure 5.4. Schematic of pixel overlay onto finite element mesh where black pixel boxes represent damaged pixels from the CT Segmentation damage mapping. The element on the right has a high enough proportion of damaged internal area to be marked as a damaged element.

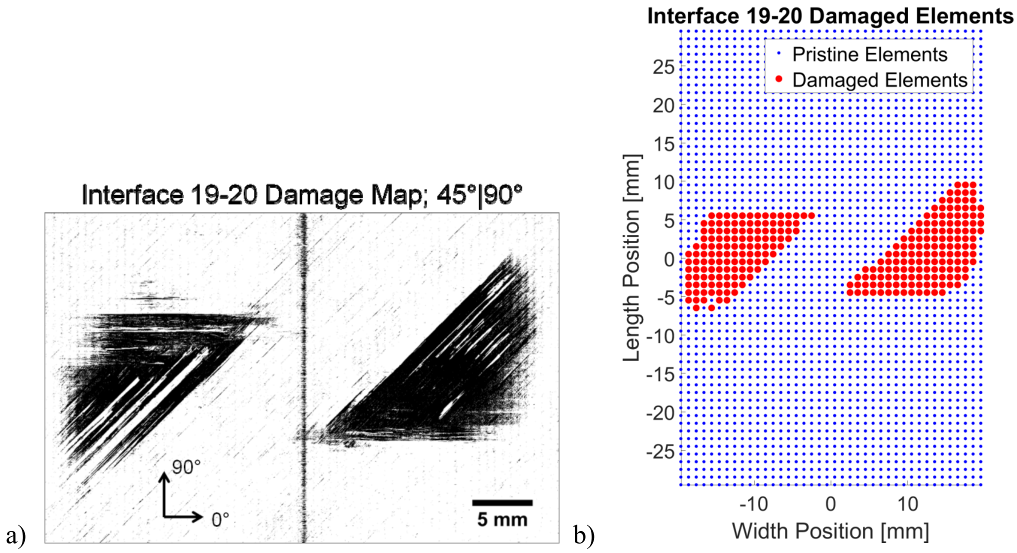

Figure 5.5. a) Delamination at an example interface from the TC-24-32-1 specimen scan, b) delamination mapping to a set of damaged elements shown as larger red markers for a representative mesh of cohesive elements.

Matrix damage may be implemented in accordance with the modeling techniques used. In the case of a fiber-aligned mesh where the continuity of cracked elements along the fiber direction is important, CT data can first be mapped to thin crack like geometry consisting of two geometrical endpoints and a direction by searching for cracks longer than a certain length that lie in the fiber direction of each ply and then outputting the crack length and position as simplified crack information. Figure 5.6a and Figure 5.6b show an example of an intraply damage map converted to a thin crack geometry by this procedure. Then thin cracks can be matched to the mesh by finding the closest set of element centers along the crack length. This procedure is applied to an example mesh in Figure 5.6c. Alternatively, for meshes that are less sensitive to fiber directionality, matrix damage can be mapped by the same overlay method as described for delamination mapping. Because fiber damage is characteristically similar to matrix cracking but approximately perpendicular to the fiber direction, implementation of the fiber breakage can be achieved by removing the damage features that are parallel to the fiber direction (i.e., removing matrix cracks) and then converting the remaining damaged pixels to thin cracks perpendicular to the fibers, i.e., similar to how matrix damage can be modeled. In certain modeling procedures that take into account the inclination of matrix cracking, this damage assignment can be coupled with the inclination quantification presented in Chapter 4.4.

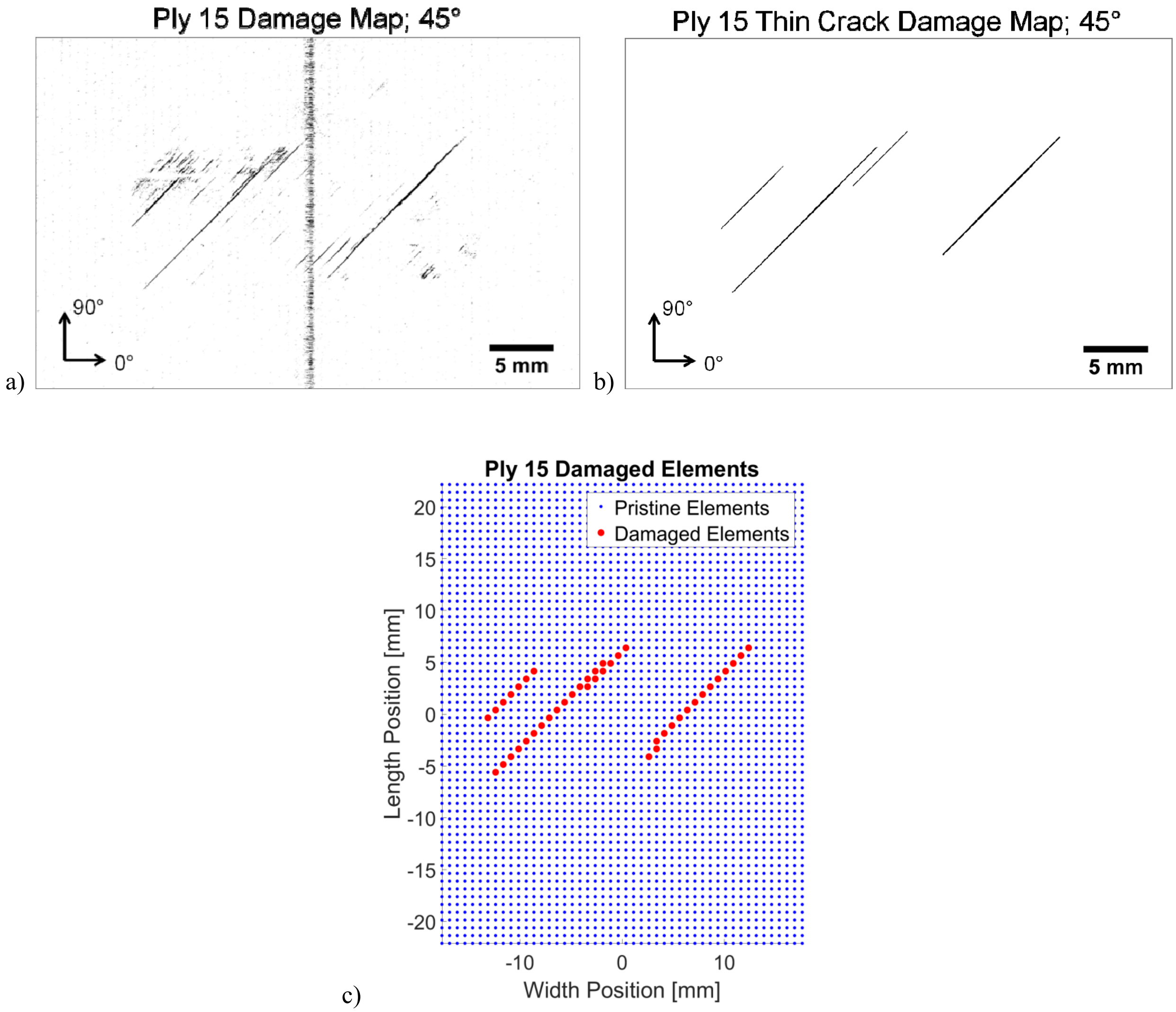

Figure 5.6. a) Intraply damage map as output by the developed CT Segmentation for the TC-24-32-1 specimen scan, b) intraply damage map converted to major 45° thin cracks by searching for damage features longer than a minimum length in the fiber direction, c) damage map converted to damaged elements in a representative set of 0.75 x 0.75 mm element centers with damaged elements shown as larger red markers.

Based on the modeling techniques suggested above, the choice of a relatively large interface size during the ply and interface identification process (in this case equal to the ply sizes) can be further justified. In general, some modeling techniques for matrix cracking may benefit from a cleaner definition of thin matrix cracks, thus the interfaces were assumed to be larger so that features from delamination cracks would not be erroneously marked as ply damage. For delamination modeling, the element mapping method based on damaged pixel area is more tolerant of small erroneous intraply damage being captured by the interface damage maps. Overall, larger assumed interface sizes reduce the effect of errors in the automatic segmentation on model generation.

Lastly, the indentation profiles extracted from CT top and bottom curve fits can be included as initial imperfection data. For modeling that implements 3D continuum elements, the indentation can be applied as the interpolation of the front and back face indentations through the thickness in order to capture geometric tapering effects. Additionally, for shell based modeling, the indentation can be implemented as the average of the front and back indentations. An example of the implementation of this residual indentation is given in the next section.

Even after defining the elements that will be marked as damaged, assigning a change in behavior that creates the desired damaged effect is a non-trivial question. Physically, damage appears as a local discontinuity of material that can no longer transfer stresses except though interfacial compression and friction. However, many common finite element techniques utilize continuum damage mechanics implementations of damage that model damage as a reduction in material properties averaged in elements instead of as a material discontinuity. One simple approach to modeling this behavior in a continuum damage framework is to reduce material properties associated with the damage mode. For example, in the case of a matrix crack within an element, matrix associated properties of E_2 and G_{12} can be reduced to a value small enough to be negligible. It should be noted that a reduction to zero of these properties is not possible in most finite element applications due to matrix stability requirements. This method may be effective for capturing the resulting stress concentration around a damage location, but in the case of cohesive elements, the reduction in stiffness may allow interpenetration of connected parts. Another approach is the reduction of material strengths to cause early failure within the model. This approach has the benefit of creating a damage state that is consistent with the damage modeling technique applied in the model. However, the presence of damage from an early state of the model may create issues for some solving techniques such as implicit integration and the damage elements may distort excessively during the analysis. In order to ensure that the damaged material follows the desired fracture behavior, the energies associated with the damage mode must be reduced by the square of the strength reduction factor. This is because the relationship between fracture energy and strength is governed by the area under the stress-strain curve and reducing the peak stress effectively reduces the area by a squared reduction factor.

5.4 MATERIAL PROPERTIES USED IN COMPRESSION SIMULATIONS

Material properties used for T800S/3900-2B are given in Table 5.1. Because Abaqus/Explicit does not currently have in-built capabilities for different compression and tension responses, the compression modulus E_{1C} was used as E_1 in the compression modeling cases. Cohesive elements were utilized to model disbond in the compression models with material properties given in Table 5.2.

Table 5.1. T800S/3900-2B simulation properties.

Density [g/cm^3]	1.55
E1T [GPa]	159.9
E1C [GPa]	131.0
E2 [GPa]	8.96
G12 [GPa]	6.205
v12	0.27
v23	0.36
Fiber Tensile Strength [MPa]	2840
Fiber Compression Strength [MPa]	1551
Matrix Tensile Strength [MPa]	55.2
Matrix Compressive Strength [MPa]	165.5
Matrix Shear Strength [MPa]	88.2
GXT [N/mm]	91.6
GXC [N/mm]	79.9
GYT [N/mm]	0.2
GYC [N/mm]	0.2

Table 5.2. Cohesive element simulation properties

Density [g/cm^3]	1.55
K [GPa]	159.9
Mode I Strength [MPa]	50
Mode II Strength [MPa]	115
Mode III Strength [MPa]	155
G_{IC} [N/mm]	0.71
G_{2C} [N/mm]	2.2
G_{3C} [N/mm]	1.7

5.5 ABAQUS MODELING OF NDE DAMAGE STATE

All models presented in this work have been created using the commercial finite element analysis software Abaqus version 6.14. Most residual strength models were performed using Abaqus/Explicit with time and mass scaling to reduce computational time. Abaqus/Explicit utilizes explicit time integration schemes that solve for the model state by taking small stable time steps forward. The maximum stable time increment is associated with the mass and volume of the smallest element. Thus, to improve quasi-static model run times the mass of the model can be augmented to increase the stable time increment as long as the increase in mass does not introduce dynamic effects into the model response. For each model, several mass scaling factors were investigated to find the maximum model speed up within the acceptable limit of kinetic energy behavior. However, due to the dynamic nature of progressive damage events, certain models such as the residual strength model of the cap impacted cases, showed dynamic response after the initial failure event.

5.6 MODELING OF FLAT PANEL CAI

A flat panel CAI model was created using the techniques developed in Chapter 4.5 that incorporated the segmented CT damage state. Modeling was primarily performed in Abaqus/Explicit due to computational difficulties in modeling an initial damage state in Abaqus/Implicit. Models were developed as a full ply-by-ply layered model with cohesive elements connecting adjacent plies.

Flat panel models were developed according to the following process: a) the geometry and mesh were created for each ply and interface. b) Material properties and section assignments were defined. b) The mesh information was fed into a script that overlays CT damage states onto the mesh of each layer to define damaged element sets, such as shown in Figure 5.5 and Figure 5.6. d) Damaged material properties and section assignments to the damage element sets were defined. e) The residual indentation map was overlaid onto the nodes and a data file was created to define the mesh initial imperfection such as shown in Figure 5.7. f) Boundary and load conditions were imposed. The overall damage mapping is shown for the TC-24-31-2 specimen in Figure 5.8. Projected damaged elements sets are shown in Figure 5.8c for ply damage and Figure 5.8 for interface damage and the through-thickness distribution of the delamination state is illustrated in Figure 5.8e.

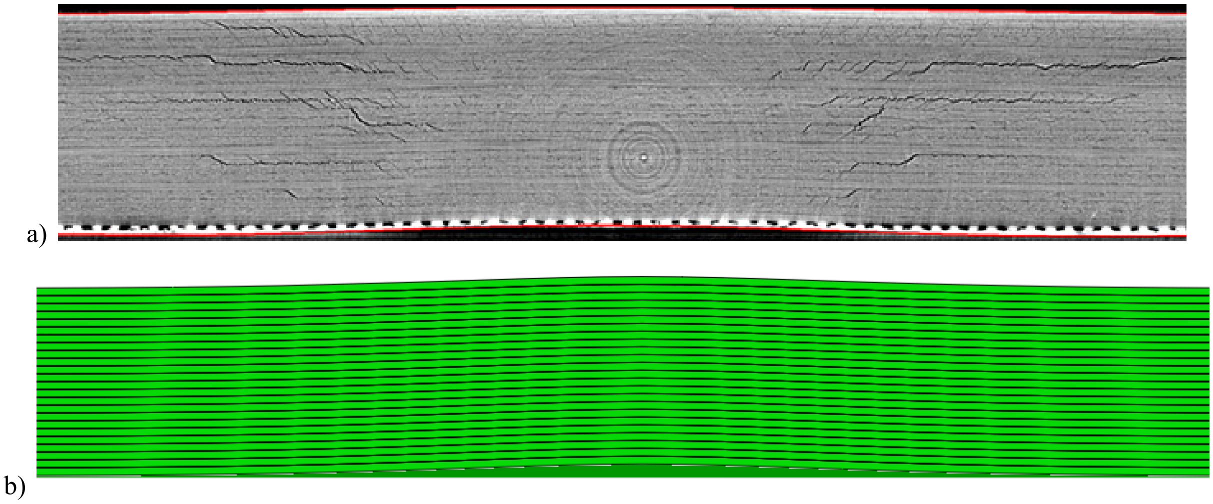

Figure 5.7. a) Example through-thickness CT slice with indentation profile highlighted. b) Indentation as imposed in the Abaqus CAI model.

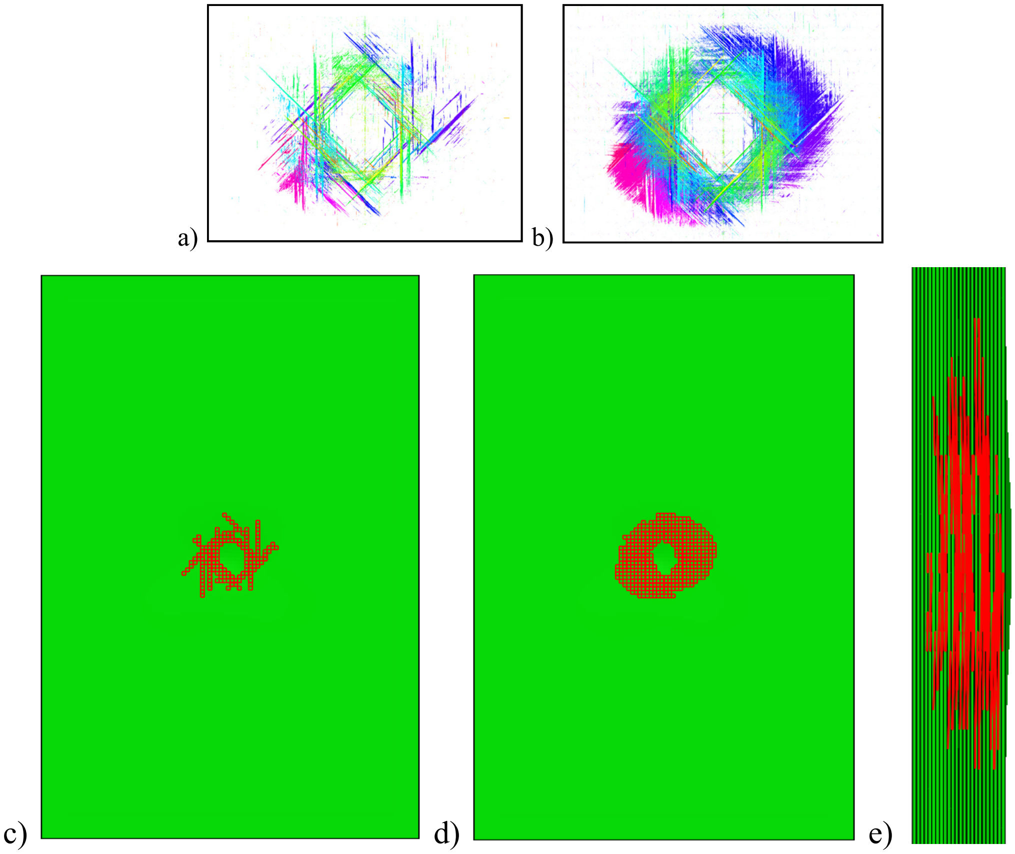

Figure 5.8. Damaged element sets as modeled in Abaqus. a) Projected intraply damage from the segmented CT results. b) Projected interply damage from the CT results. c) Projected intraply damaged elements. d) Projected interply damaged elements. e) Through-thickness view of delamination distribution.

The developed model was then run with reduced strength for the elements marked as damaged by the previous procedure. A uniform mesh size of 1 mm square elements was used in a addition to the ply-by-ply modeling approach this created a mesh with 740,000 elements and 2.3 million degrees of freedom. Force-displacement results for the model that incorporated the CT damage state and indentation for specimen TC-24-31-2 is shown in Figure 5.9. Although the stiffness of the model agrees well with the DCDT displacement results for this specimen, the overall failure behavior is largely over-predicted. This indicates that either the conversion of the damage state to damaged element sets is inaccurate due to the resolution limitations of the mesh size or that the implementation of damaged material within the CDM modeling techniques is not physically capturing the effect of the damage state. In many studies of CAI behavior for flat panels, sublaminate buckling behavior is identified as a key driver of the failure behavior [12] hence it may be the case that the modeling of the delamination does not allow for sublaminate buckling behavior and thus prevents failure due to the initial damage state. The final failure state of the model is shown in Figure 5.10 and indicates a failure mode that is close to the experimentally observed failure behavior, namely a central band of compression failure.

The general difficulty of capturing the failed behavior in this case may be due to a variety of causes. First, the mesh may be too coarse to accurately model the progression of cohesive damage. Second, the CDM modeling approach may not capture the interplay between delamination and matrix cracking. As observed in post-failed CT scanning for this type of specimen, several features of the brooming failure were seen as sublaminate domains sliding past one another with an angled matrix crack as a slip plane. This type of kinematic matrix crack behavior is not captured by a general reduction in material properties as implemented in this CDM modeling approach. Lastly, due to resolution constraints in the CT characterization, it is possible that the implemented delamination under predicts the actual damage state. Given the unstable behavior of sublaminate buckling, slight changes in the effective length of delaminations may have significant effects on the stability of the delaminated composite.

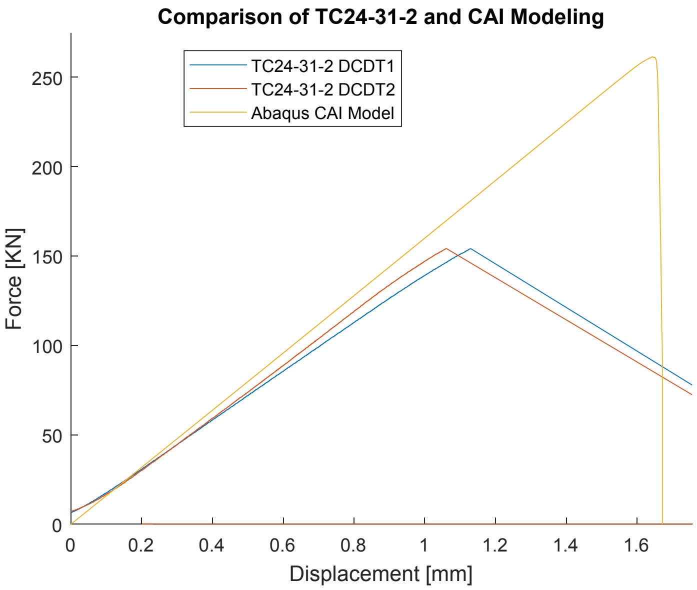

Figure 5.9. Force-history response of TC-24-31-2 CAI model compared with experimental DCDT results.

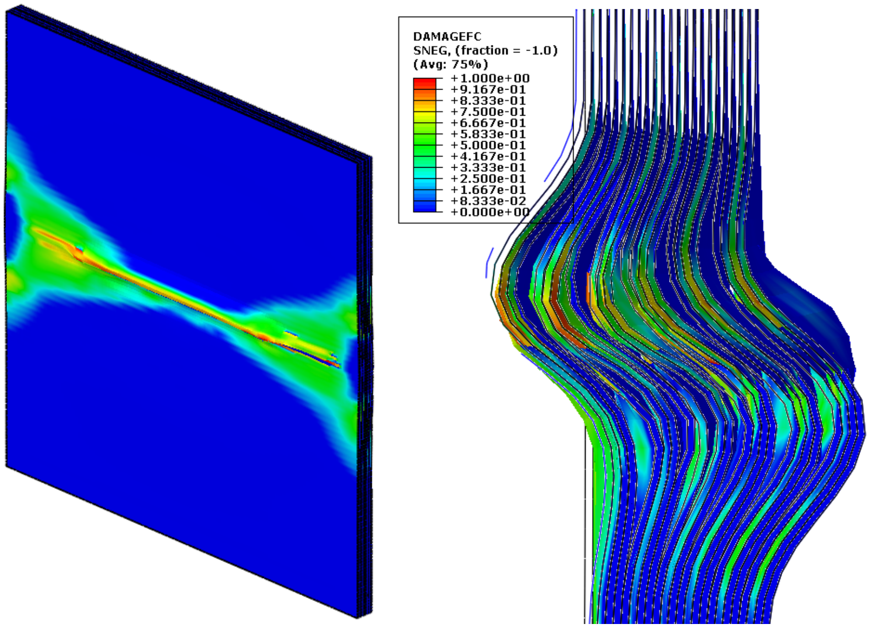

Figure 5.10. Failure mode for CAI model of specimen TC-24-31-2.

5.7 MODELING OF FLANGE IMPACTED RESIDUAL STRENGTH

Residual strength models were created for the flange impacted residual strength specimens using approximations of the damage state as observed in the UT C-scan TOF maps as discussed in Chapter 4.9. Initially, a non-impacted specimen model was created as shown in Figure 5.11. This base model consists of reduced integration continuum shell elements for the skin and stringer laminate with a layer of cohesive elements connecting the skin and stringer flanges. Material properties used for T800S/3900-2B are given in Table 5.1. It should be noted that this material system has a significant difference between the tensile and compressive moduli along the fiber direction (151 and 129.9 GPa respectively). Because this test places the specimen into a primarily compressive stress state and because Abaqus does not include a separate material law for tension and compression, without the use of user subroutines, the compressive modulus was used for E_1 in these models which could be a source of error, especially as the post-buckling state may induce significant tensile stresses before final failure. Boundary conditions were imposed by contact with a rigid plate to simulate the compressive platen loading. The end potting was modeled as a zone of constrained out-of-plane displacement. The base mesh size was a uniform 3 mm mesh. This mesh size is significantly larger than the recommended mesh size based on recommendations for cohesive element sizing to achieve effective disbond growth. However, for this case sudden and final failure was observed as the first damage growth, so it may be sufficient to consider the cohesive initiation criteria as the final failure point in the model.

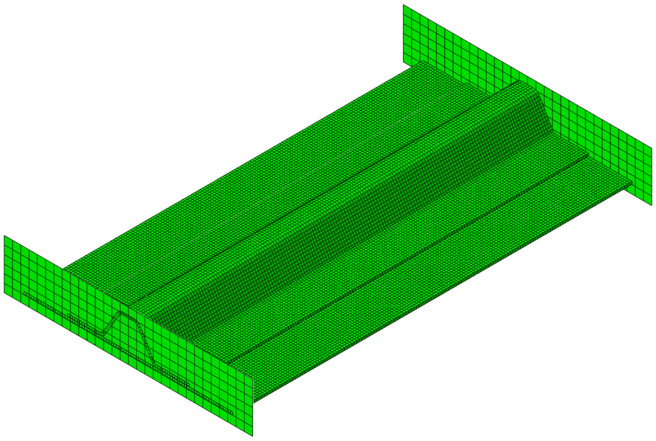

Figure 5.11. View of base 3 mm element mesh for the undamaged residual strength test case.

Initial buckling mode analyses predicted a three half-wave buckling mode in the skin as was observed during compression testing. Figure 5.12 shows a comparison between the predicted buckling mode from Abaqus and the observed 3 half-wave mode captured by DIC. The predicted end-shortening at the onset of buckling was 1.1 mm and the experimentally observed onset of buckling was seen around 1.78 mm crosshead displacement as can be observed in the force-displacement behavior shown in Figure 3.26. To prevent dynamic effects from the sudden onset of buckling behavior, all flange type models were seeded with an initial imperfection based on the first calculated buckling mode of 0.1 mm, about half of a ply thickness.

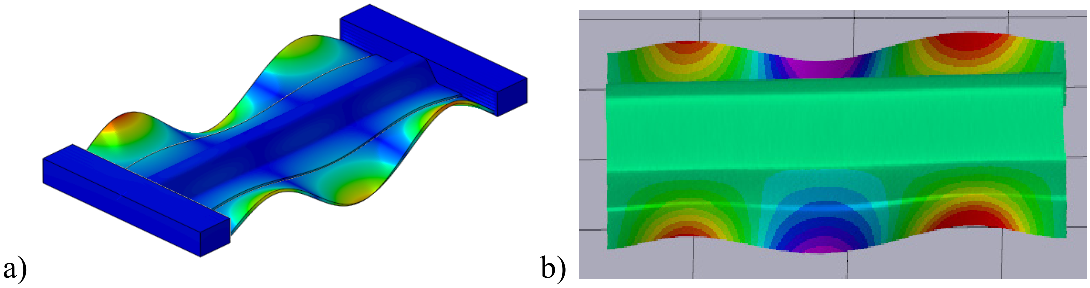

Figure 5.12. Buckling mode for the undamaged specimen as a) predicted by buckling analyses and b) as observed during compression testing.

Model force-displacement results are shown in Figure 5.13 compared with experimentally observed results for the non-impacted specimen. Model initial stiffness and peak force agree very well with experimental results although there is a slight discrepancy between the final displacements at failure. Figure 5.14 shows the failure mode and location observed in the model and test. The location of the skin compression failure shows good agreement with the location of damage in the test specimen, but the stringer failure location is offset from the mid-span of the specimen where damage was observed in the test.

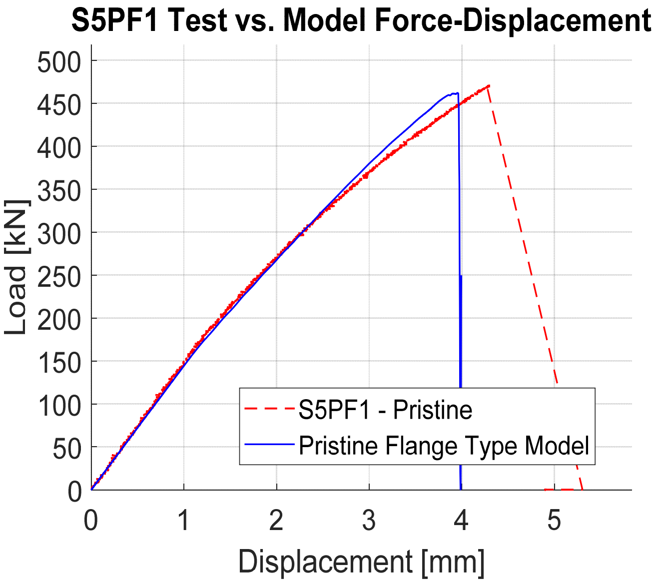

Figure 5.13. Force history results comparing the pristine model to the S5PF1 test specimen.

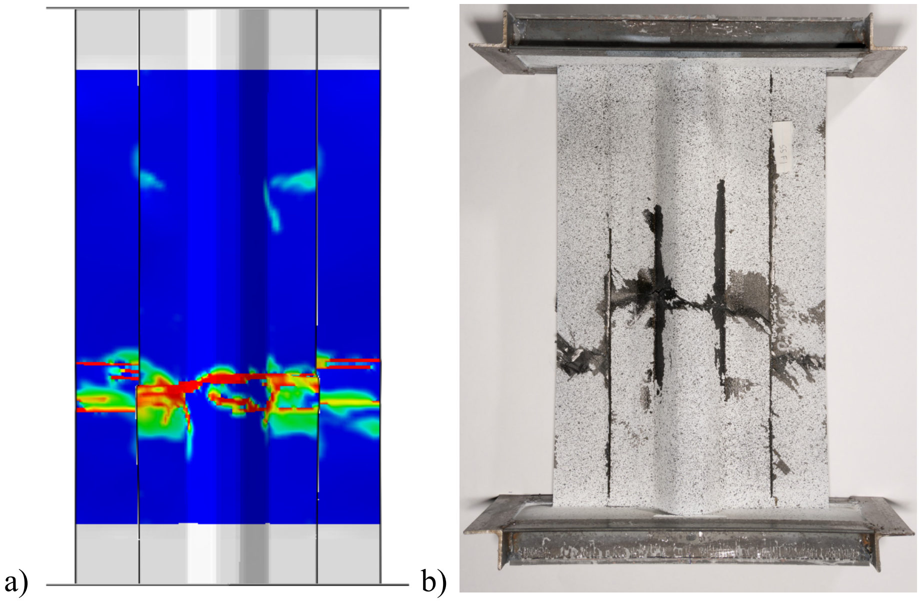

Figure 5.14. Failure mode for pristine specimen a) model (fiber compression damage variable) and b) test specimen S5PF1.

To verify the quality of the 3 mm mesh model, a mesh sensitivity study was performed for the pristine model case. Force-displacement curves for this mesh study are shown in Figure 5.15. Although there is a slight difference in failure displacement between the 3 mm mesh and the 1 and 2 mm meshes, the overall predicted failure load is in very good agreement with the test and did not change significantly with the mesh size. This suggests that the 3 mm mesh case can be considered converged. The likely reason for the slight difference in failure behavior is that the cohesive elements may require a higher opening displacement before failure in the refined mesh cases.

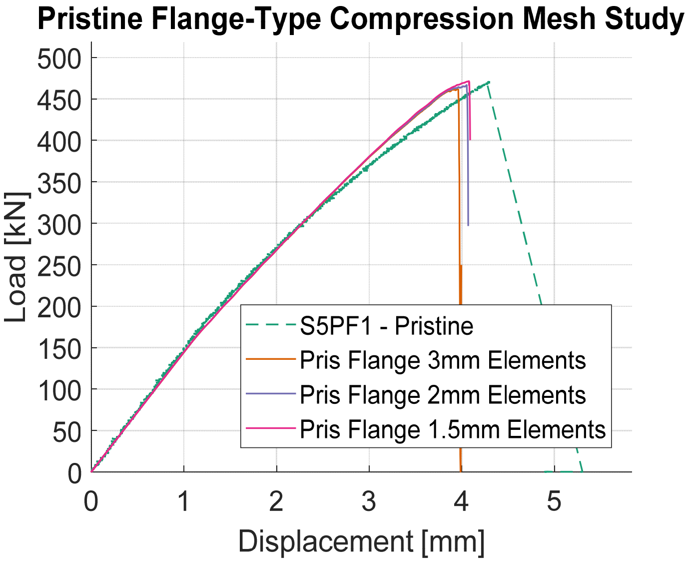

Figure 5.15. Mesh study force-displacement curves for the pristine flange-type compression case.

To model the initial damage state observed in the UT scans, the mesh details from the pristine model were overlaid with the UT damage as illustrated in Figure 5.16a. To establish an initial damage state in the cohesive elements connecting the skin and stringer, the overall damage extent was overlaid as an envelope to the cohesive elements and any elements contained within were included in a damaged element set that was assigned properties representative of initial cohesive damage (as discussed in Section 5.3) such as the example cohesive damage zone represented in Figure 5.16b. Laminate damage was represented in this first set of models as a reduction of matrix properties (E_2, G_{12}, v_{12}) in the roughly circular zones depicted in Figure 5.16a in red for skin damage as seen in Figure 5.16c and blue for flange damage as seen in Figure 5.16d. This approach generates a rough approximation of how the delamination and matrix cracking in the laminates may affect the overall properties. Due to the lack of CT characterization for the residual strength tested flange impact specimens and the computational cost of ply-by-ply modeling approaches, this method was chosen with the assumption that the major form of damage in these tests was disbond growth driven, and thus ply-by-ply modeling may not be required to capture the critical failure type. All specimen UT disbond areas and resulting damaged cohesive elements are shown in Figure 5.17. The resulting delamination area shows that the 64.8 J impact damage area is more closely trapezoidal compared to the higher impact energy cases which have a more curved disbond boundary. This behavior may be due to more localization of the damage in the higher impact energy case, potentially resulting in greater laminate damage for these specimens.

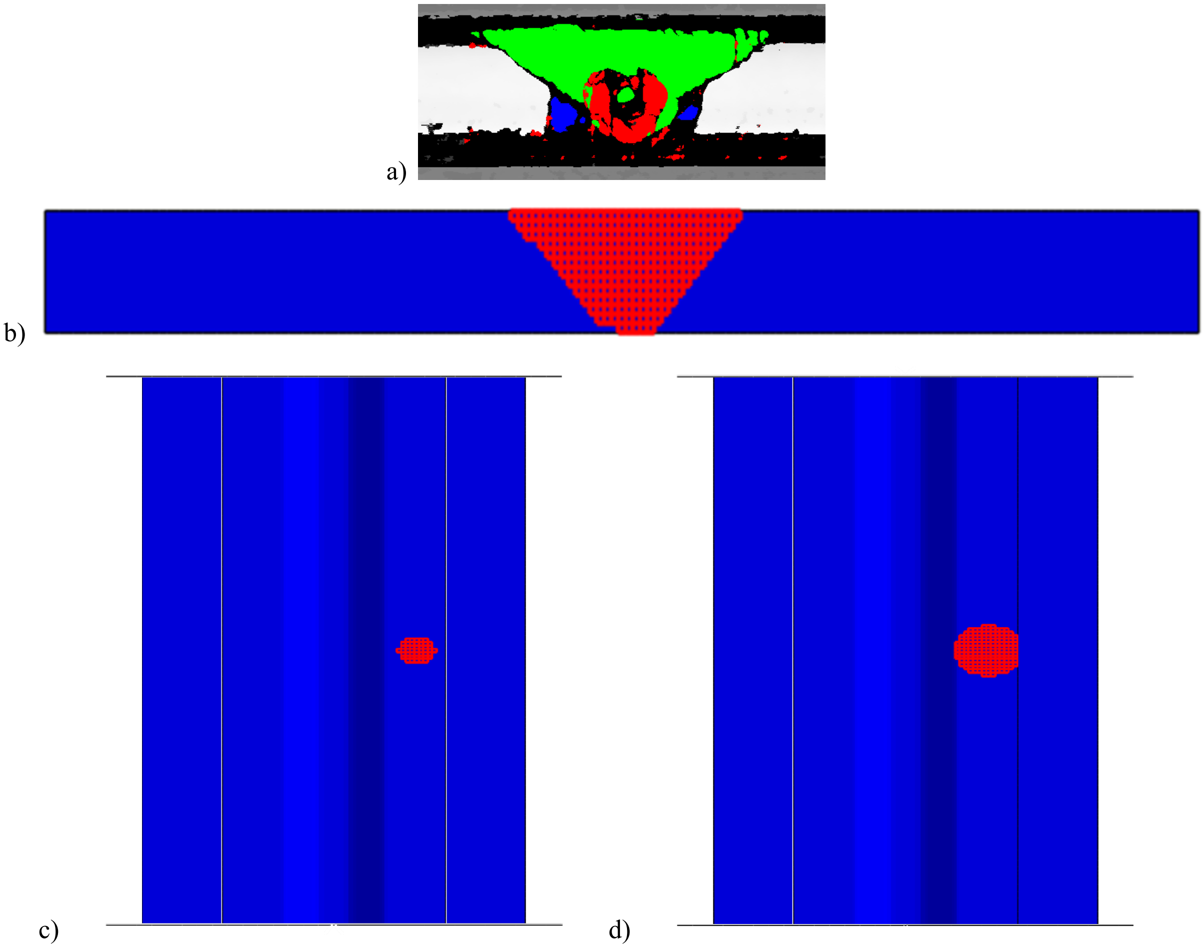

Figure 5.16. a) Damage observed in UT scan color coded as described in Chapter 4.14. b) Damaged elements mapped onto cohesive elements connecting the skin and flange. c) Damaged elements mapped onto the skin laminate. d) Damaged elements mapped onto the flange laminate.

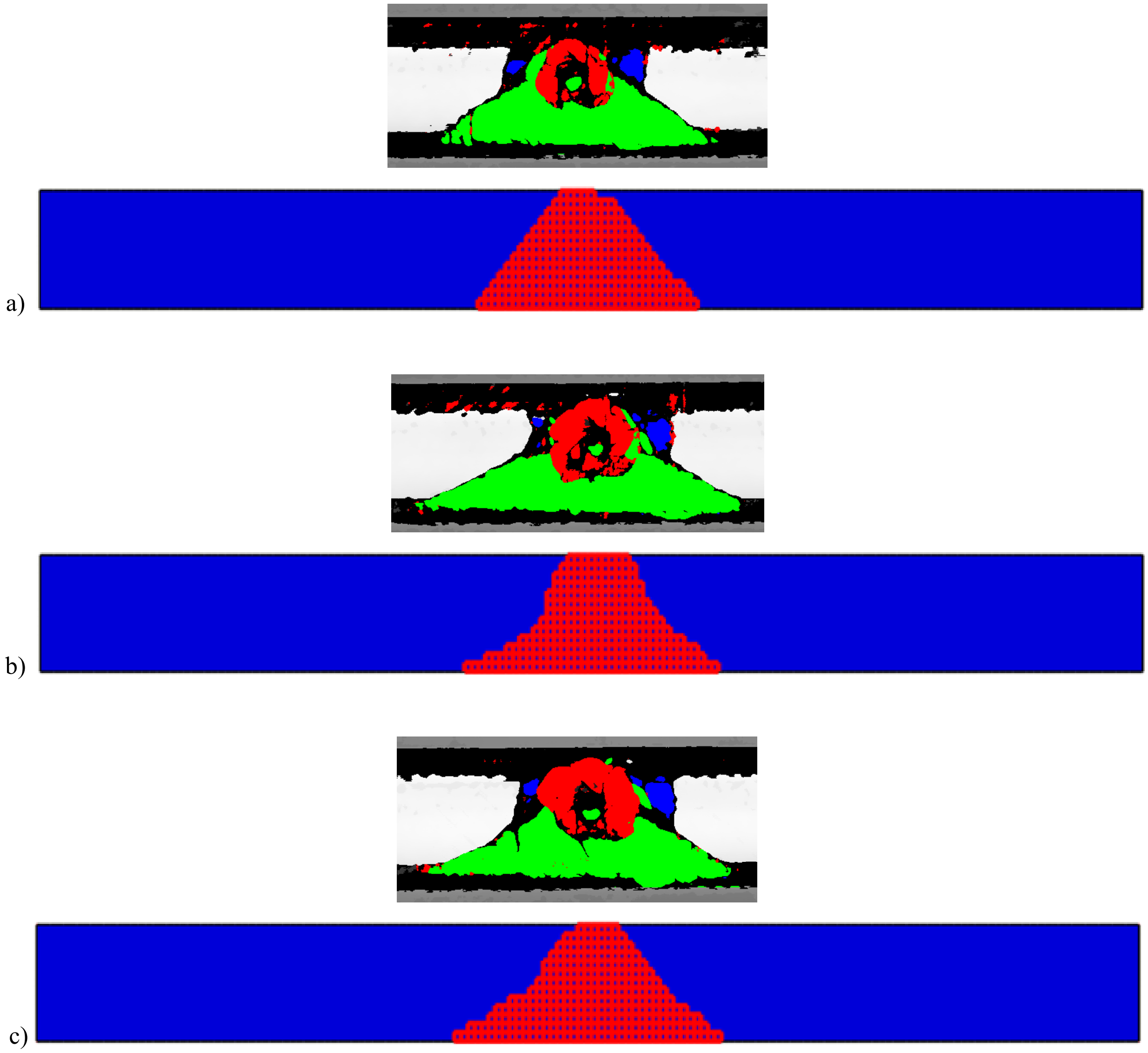

Figure 5.17. All color coded impact damage states measured from UT scanning and mapped damaged element sets into Abaqus. a) Specimen S4F2. b) Specimen S3F1. c) Specimen S3F2.

Models were run for all three impacted specimens with the initial disbond implemented as strength reduced cohesive zones and for both matrix damage and no matrix damage modeling cases. Modeling of specimen S4F2 (64.8 J impact, Figure 5.18a) shows a very good correlation between the force-displacement from the compression test and nearly no effect from the inclusion of matrix damage. In contrast, modeling of specimen S3F1 (84.5 J impact, Figure 5.18b) shows a good match between experiment and model for the model which includes the simplified matrix damage implementation, but the model with no matrix damage shows a significantly higher failure load that is closer to the response of the lower impact energy specimen. Similarly, the model of specimen S3F2 (82.8 J impact, Figure 5.18c) also correlated well with the experimental results when the simplified matrix cracking was included, but over-predicted the failure load when only the disbond was input into the model. This may indicate that the damage mode for the higher impact energy case is more strongly associated with laminate failure and the stress concentrations due to ply damage than in the lower energy case, thereby requiring some form of stress concentration to capture the appropriate failure load, in this case modeled as simplified matrix cracking. Model and experimental results are summarized in Table 5.3 for the flange impact compression specimens.

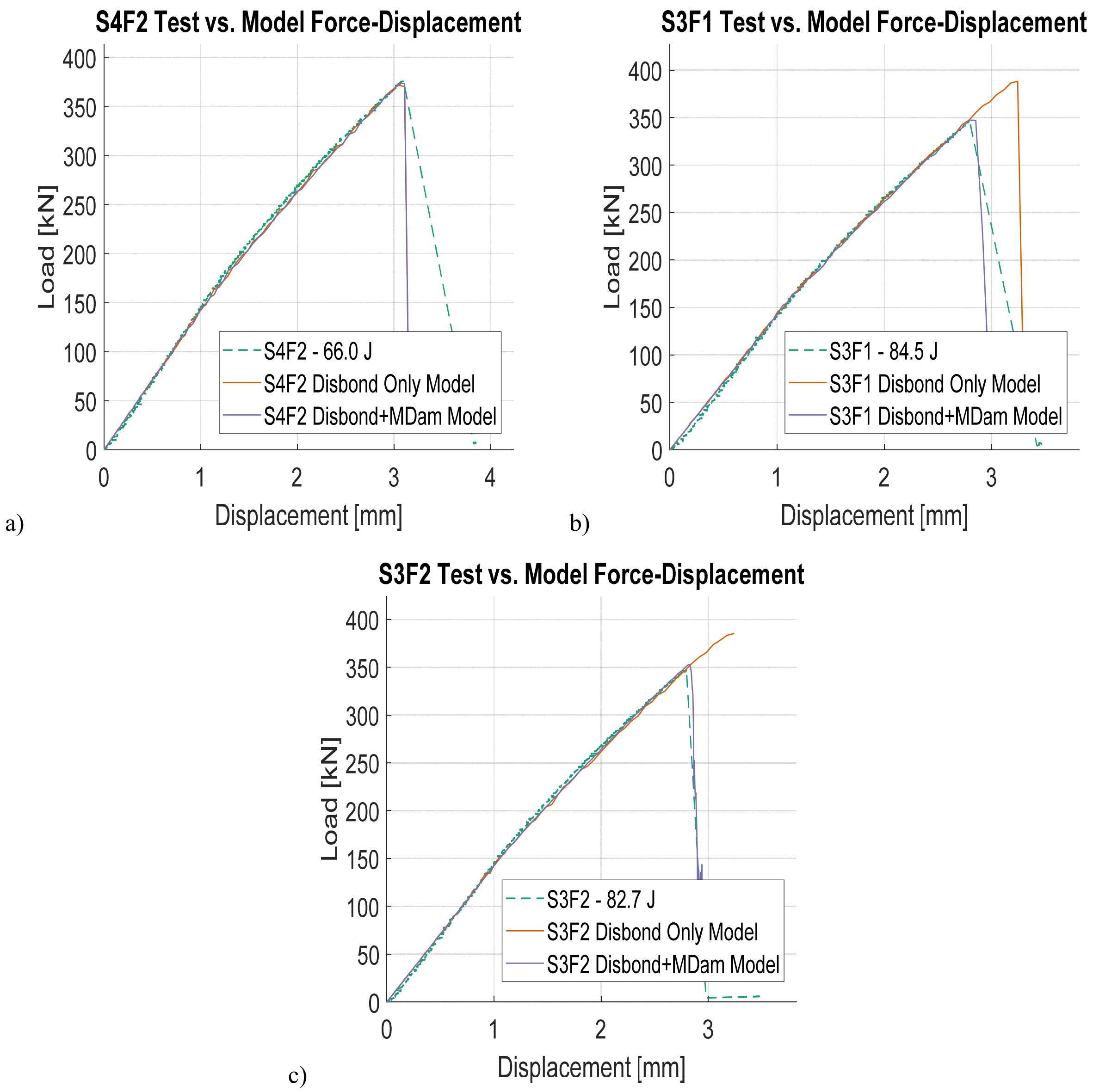

Figure 5.18. Impacted model results for cases including and not including simplified matrix damage implementation. a) Modeling of specimen S4F2. b) Modeling of specimen S3F1. c) Modeling of specimen S3F2.

Table 5.3. Comparison of residual strength experiments and modeling for flange impacted single stringer specimens.

Specimen ID	Impact Energy [J]	Experiment Peak Load [kN]	Experiment Peak Disp. [mm]	Model Peak Load [kN]	Model Peak Displacement [mm]
S5PF1	--	470.9	4.27	464.8	4.04
S4F2	70	376.1	3.07	376.9	3.15
S3F1	90	347.2	2.79	350.0	2.84
S3F2	90	347.2	2.79	352.7	2.82

5.8 MODELING OF CAP IMPACTED RESIDUAL STRENGTH

Models of the cap-impacted type specimens were created to investigate what kinds of damage features need to be included in a FEA model of residual strength to capture the effect of impact damage. For this type of specimen, primary modeling goals include capturing the progressive damage events of cap failure leading up to final failure. Because models were run with an explicit time integration scheme utilizing mass scaling, this progressive damage event posed a significant challenge for modeling due to the sudden acceleration and energy release during this event.

First, the non-impacted specimen was modeled with single continuum shell layups for both the skin and stringer with the built-in Hashin damage criteria in Abaqus to model ply damage modes. Because of the buckling of the skin away from the stringer after the final failure, an additional layer of cohesive elements was included between the flange and skin to allow the model to capture this type of disbonding. The basic mesh size chosen was a uniform 3 mm mesh resulting in a model with 12866 elements and 38598 degrees of freedom as shown in Figure 5.19. Model results are compared with both non-impacted specimens in Figure 5.20. The initial model stiffness compares well with both specimens, but the final non-linear behavior leading to failure as observed in the experiments was not captured by the model. This effect is most likely due to fiber compression non-linearity near failure as observed in Allix et al. [55] and as shown in Figure 5.21 for an example compression coupon testing result.

In addition to the 3 mm uniform element size mesh, a mesh study of the pristine model was conducted for mesh sizes of 2 and 1 mm. Force-history results for the three different mesh sizes are shown in Figure 5.22. Models show good agreement in pre-failure behavior for all three meshes, but the 1 mm mesh case shows a somewhat different failure behavior where the post failure initiation force increases slightly before the final model failure.

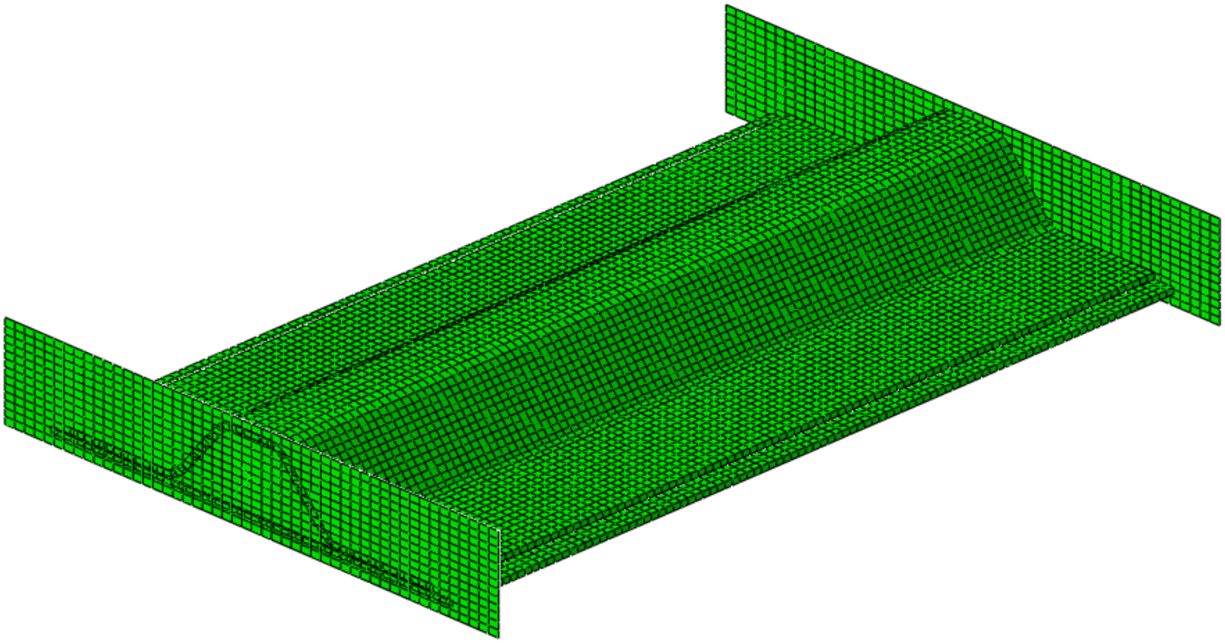

Figure 5.19. General compression model for cap-impact type specimens.

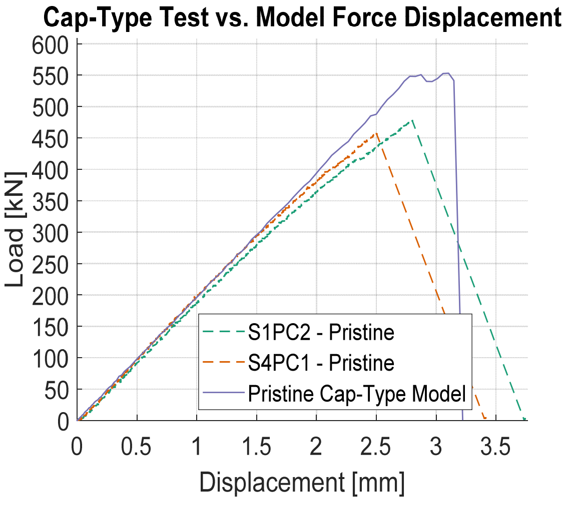

Figure 5.20. Comparison of pristine model and experiment. Model shows good stiffness comparison with test, but fails to capture some of the non-linear behavior leading to failure as observed in the test.

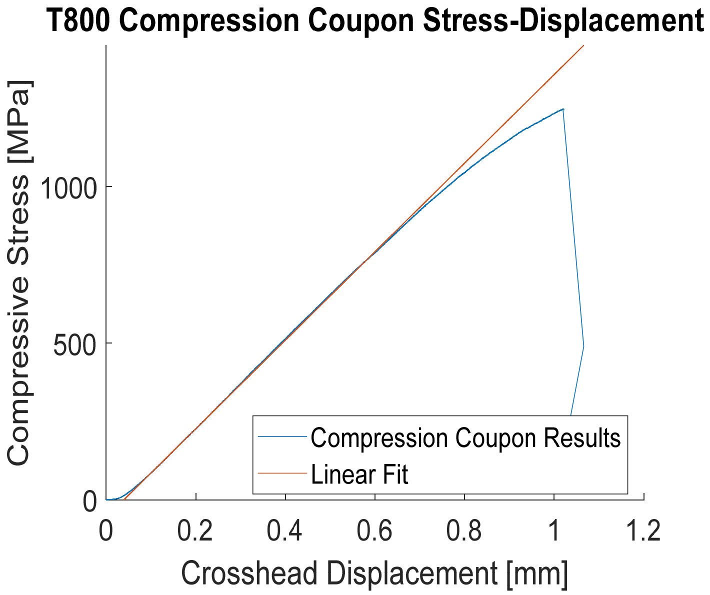

Figure 5.21. Example compression coupon data showing non-linear stress response before compressive failure.

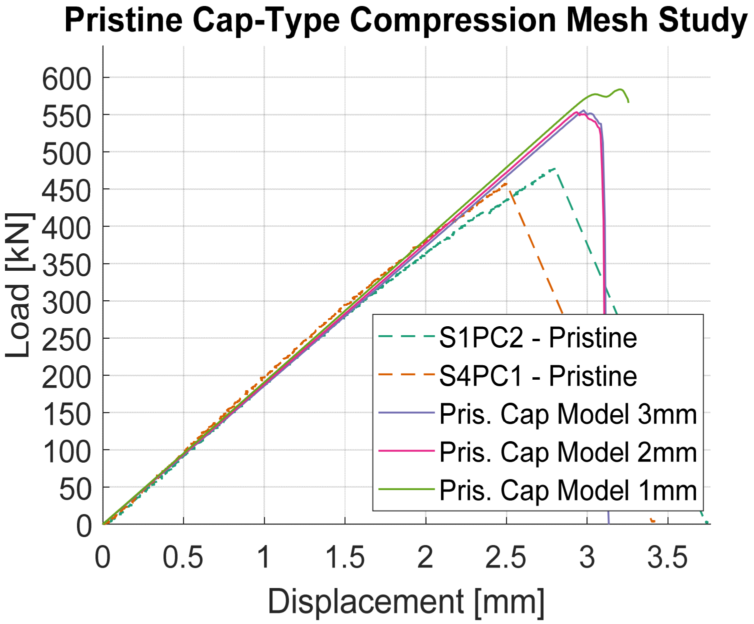

Figure 5.22. Mesh study force-history results for the pristine cap-type specimen model.

To break down the damage state as captured by CT analysis two major damage modes were investigated: major disbonding that contributes to sublaminate buckling and fiber damage that leads to cap failure.

Major disbonding was observed between most plies, except the laminate mid-plane, but to reduce model complexity and allow for a ply grouped modeling approach, delaminations were classified by types based on how likely they would be to cause sublaminate buckling. The three major types of delaminations were found to be: delaminations that stretch along the crown longitudinally (see Figure 5.23a), delaminations primarily contained in the radius that stretch longitudinally (see Figure 5.23b), and radius delaminations near the mid region (see Figure 5.23c). Because of their length and size along the loading direction, the class of delaminations as seen in Figure 5.23a were chosen as the most important to include in the cap damage model. The other two classes of delaminations are smaller and concentrated in the stringer radius region where the specimen curvature was assumed to somewhat inhibit sublaminate buckling.

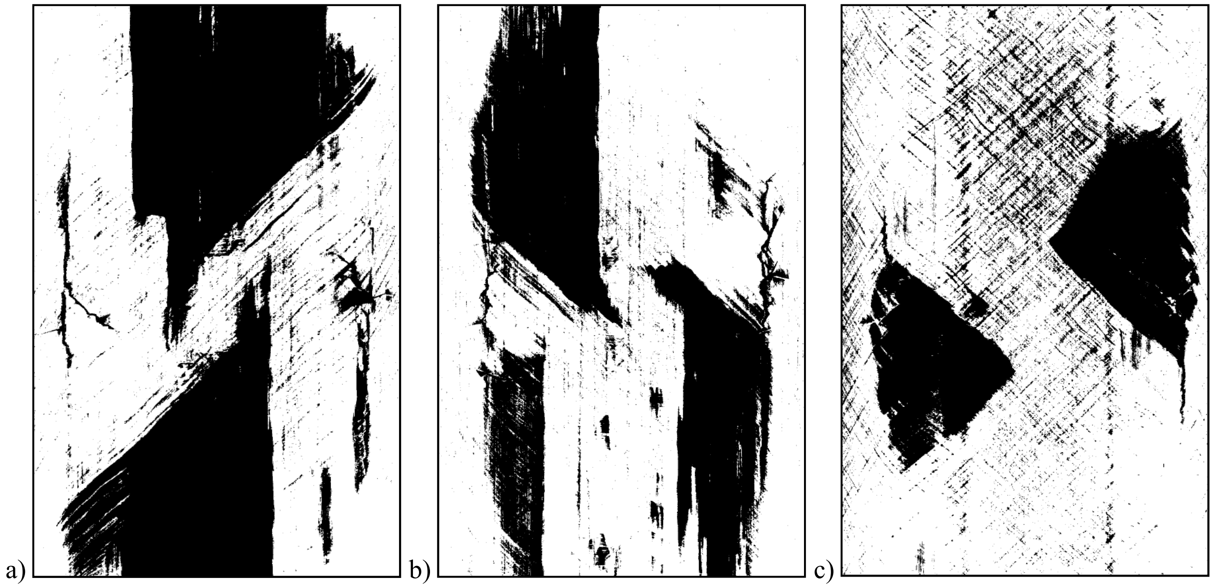

Figure 5.23. Examples of delaminations based on major characteristics. a) Longitudinal crown delamination. b) Longitudinal radius delamination. c) Mid radial delamination.

Ply damage such as fiber breakage and matrix cracking was also simplified based on the impact case modeled. For the high energy impacted specimens where damage traveled into the web on both sides of the cap, this damage feature was taken to be the most critical to model. A color coded map of the 2D projected delaminations can be seen in Figure 5.24 showing a horizontal band of damage near the impact center. Additionally, an example of this damage feature broken down by ply and interface can be seen in Chapter 4. To simplify this feature, fiber damage was applied to the entire laminate in a 5 mm wide strip to both the radius and web near the impact center, except in 90° plies where the direction of this feature corresponds with matrix damage instead of fiber breakage.

In order to streamline model development, a general script to generate models with varying levels of damage and delamination was created in Python for use with Abaqus. To prevent the computational costs associated with full ply-by-ply modeling, the script was designed to utilize user selected ply grouping to model delamination at a reduced number of interfaces. Ply groups were chosen based on modeling the most critical delaminations. Additionally, to model initial fiber damage and delamination, elements were assigned damaged material properties based on the reference sections shown in Figure 5.25. In the case of long delaminations in the crown, cohesive elements in regions 4, 5, and 6 were marked as initially damaged, and in the case of fiber damage travelling into the stringer web sections 3, 4, 6, and 7 were marked with reduced fiber compression strength properties.

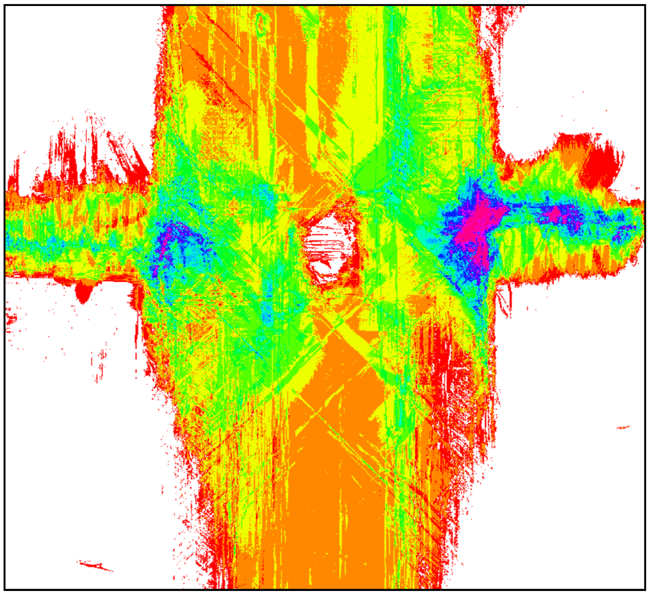

Figure 5.24. Map of delaminations and ply damage for specimen S4C2 color coded by the number of damage features in that region. The horizontal band of damage observed here is strongly associated with fiber damage and delamination traveling down the web.

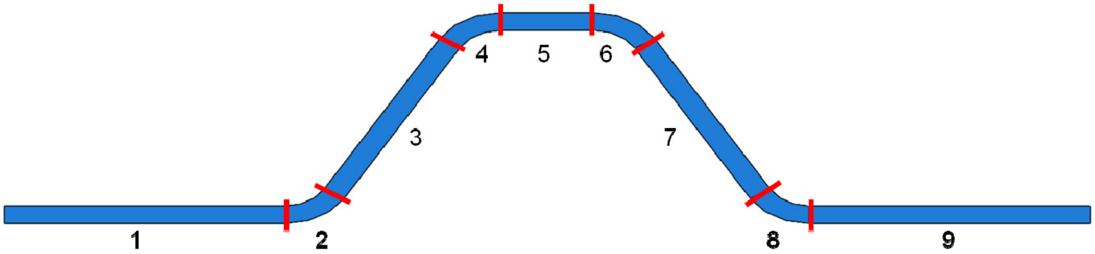

Figure 5.25. Stringer sections as partitioned in the Abaqus model.

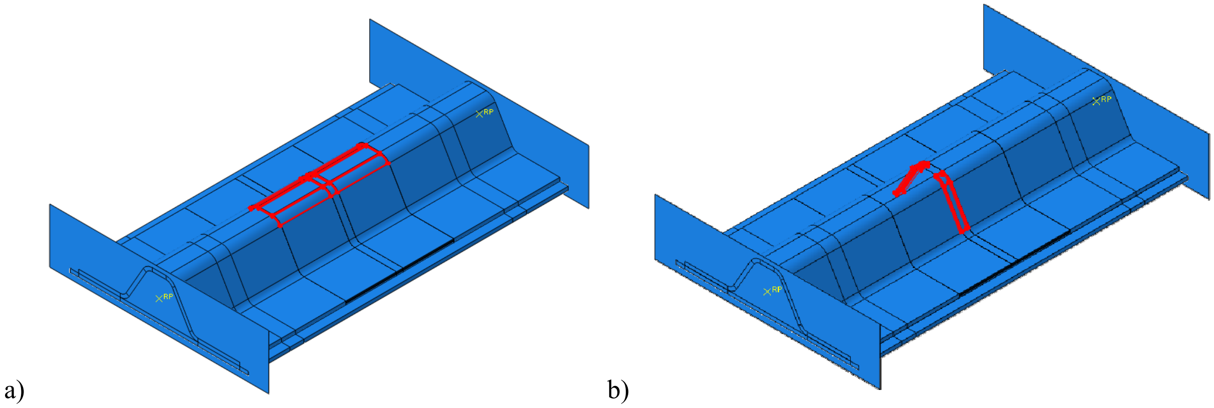

a)

b)

Figure 5.26. Initial damage state as applied to the Abaqus model of specimen S4C2: a) zones with initial cohesive damage between ply groups and b) the band of fiber damaged elements.

The affected regions in the high energy impacted specimen model are highlighted in Figure 5.26b. Because of the severity of a fiber damage feature like this, the fiber damage band and sublaminate buckling critical delaminations were the only damage features included in the high-energy impacted residual strength model. The high-energy impacted model force-displacement results are shown in Figure 5.27 compared with specimen SSC3 test results. The failure states from the model are shown in Figure 5.28. The first failure event shows a progression of the damage state slightly further into the stringer web root and across the crown, completing the fiber damage across the cap. The second failure event shows a progression of the fiber damage across the stringer flange and some buckling of the skin away from the stringer flange. The model captures the initial cap failure event, as observed in the experiment, fairly well in behavior (see the failure mode in Figure 5.28a) and initiation force, but the final failure load is over predicted by the model. Additionally, the presence of the cap failure event presents difficulties for explicit modeling, because the sudden increase in kinetic energy can cause excessive distortion errors and lead to oscillations as a results of the mass scaling scheme employed. As a result, the model presents oscillatory force behavior after the onset of this cap damage.

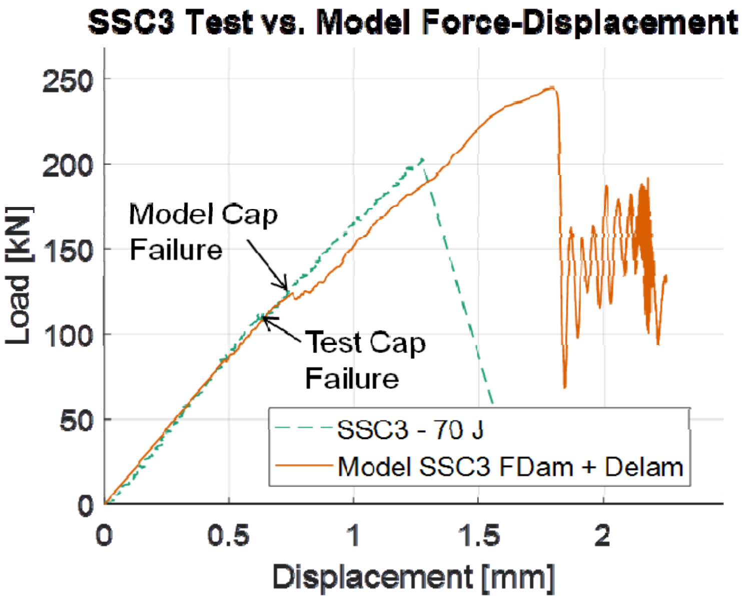

Figure 5.27. Comparison of model and experiment force-displacement curves. Model shows good agreement with initial cap failure displacement, but over predicts the final failure strength.

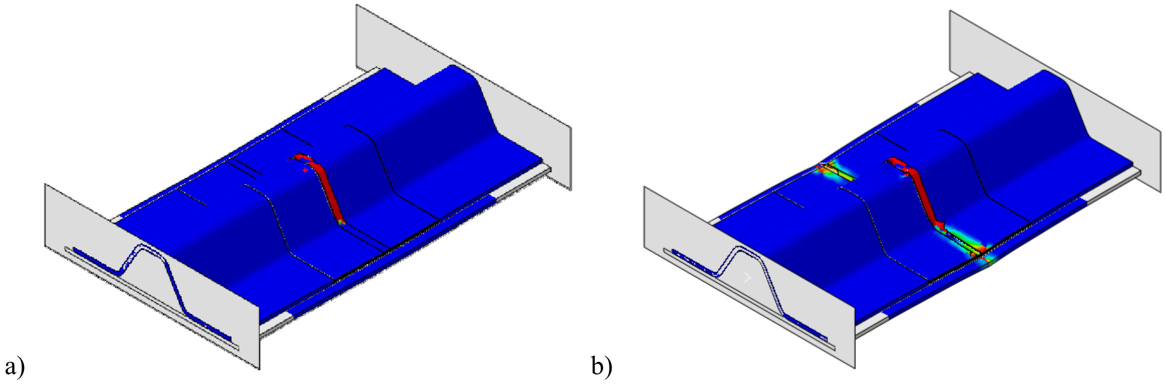

Figure 5.28. a) Fiber damage state after initial cap failure and b) fiber damage state after final failure.

To verify that the model is capturing the effect of delaminations on the residual strength behavior, the out-of-plane displacement fields from the model and DIC results directly before cap failure are shown in Figure 5.29. The overall behavior of a slight buckling inward of the skin, and the outward buckling at the center of the crown show good qualitative agreement between the DIC and model. Because of the initial fiber damage and the usual behavior of failed elements in Abaqus, it is not possible to plot an accurate displacement field from the model in the stringer web region to compare with the DIC results that show a highly localized crack like feature in the displacement field of the web.

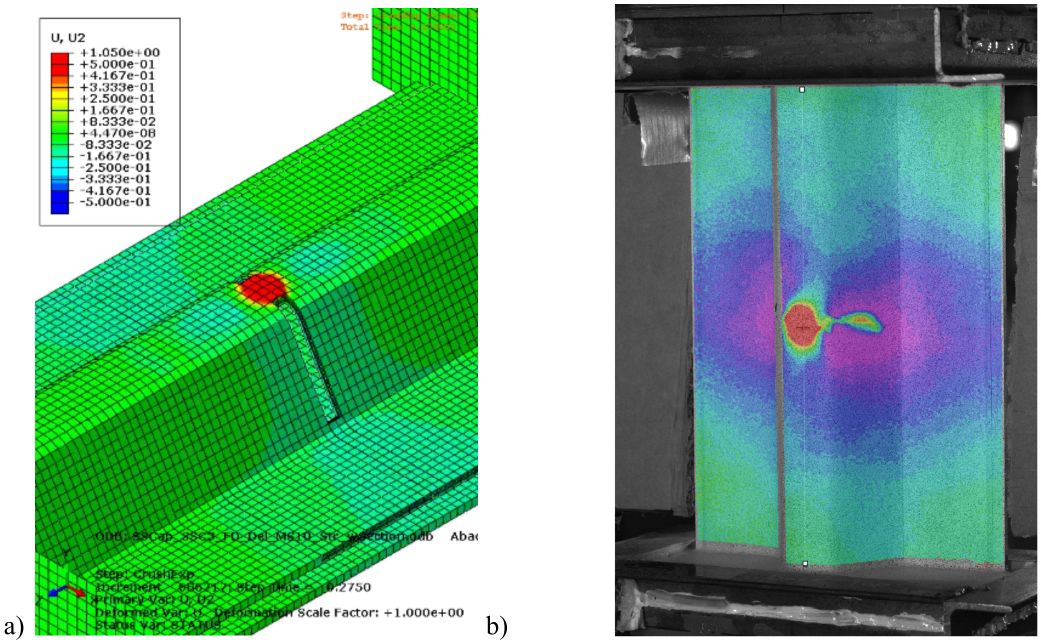

Figure 5.29. Sublaminate buckling behavior as observed in the out-of-plane displacement fields directly before cap failure event for a) the high impact energy residual strength model (U2 variable is the out-of-plane displacement in the model) and b) DIC results from the specimen SSC3 test.

To verify the model performance, several mesh cases were studied. Figure 5.30 shows the force-displacement curves for the model mesh sizes of 3, 2, and 1 mm overall mesh sizes. The 3 and 2 mm model cases showed good initiation and final failure agreement, however, the 1 mm mesh case crashed prematurely due to excessive element distortion. This difficulty is likely due to the behavior of failed cohesive elements which are not deleted after failure in order to prevent interpenetration of the sublaminates. Overall, the mesh study indicates that the 3 mm mesh is sufficiently converged.

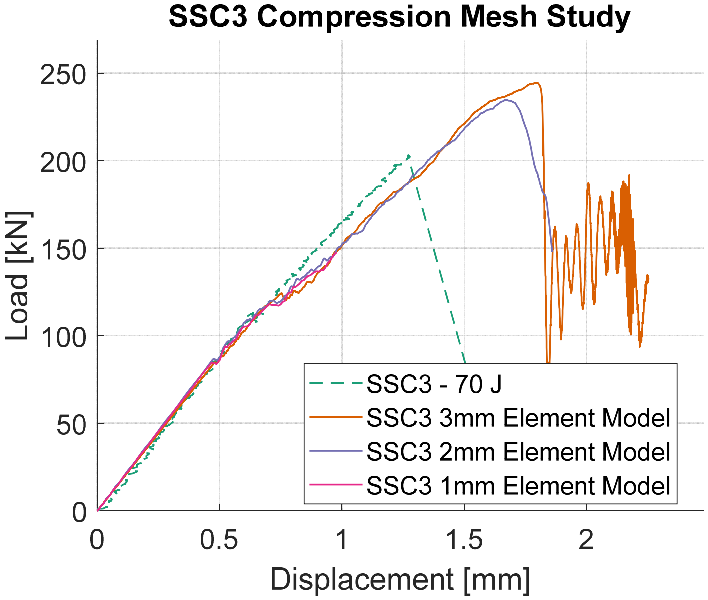

Figure 5.30. Mesh study of high-energy cap impact residual strength model.

For the lower impact energy cases, there were two different damage formations for the two tested residual strength specimens. For S4C3, the damage state was observed to be fully contained within the crown and stringer radius, but for S2C2 the damage state traveled into the web on one side of the cap, creating an asymmetric fiber damage like feature in this specimen. In the crown contained case, the damage state is primarily composed of delaminations and some more significant ply damage within the radius region. The first modeling approach taken for this case was to use the fiber damage band method used for the higher energy impact case with the damage zone reduced to just the radius region sections of 4 and 6 as indicated in Figure 5.24. The force-history results for this radius fiber damage model are shown in Figure 5.31 compared with both runs of the S4C3 specimen. The model does not capture the initial cap failure event as observed in the experiments and greatly over-predicts the final failure load. This indicates that to accurately model the damage behavior in this case, a more detailed implementation of delaminations and the radius ply damage may be required.

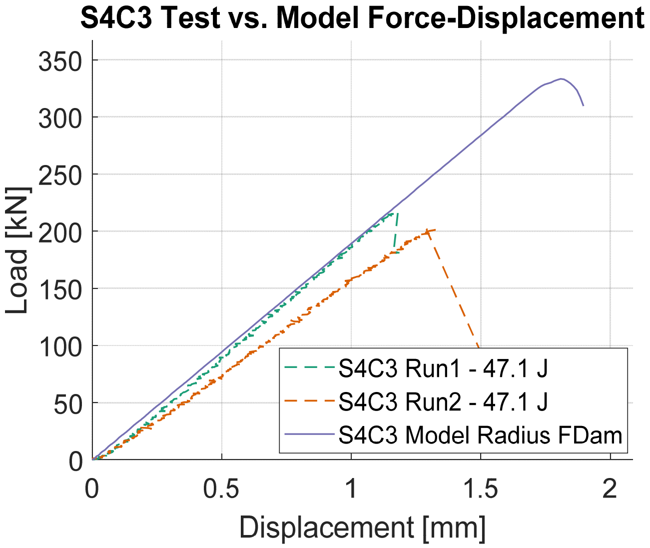

Figure 5.31. Force-history results for radius fiber damage model of S4C3 damage state.

To model the asymmetric web damage observed in specimen S2C2, the fiber damage model was adapted to a one sided initial damage zone of sections 6 and 7 as indicated in Figure 5.24 as shown in the highlighted region in Figure 5.32. Similarly to the experiment, this model had an initial failure mode where only the side of the cap with web fiber damage failed following the first damage event. The displacement field in the model post-initial failure is shown in Figure 5.33a. This displacement field is similar to the displacement field observed in the DIC results for S2C2 after the first load drop as seen in Figure 5.33b-c. The initial progression of the damage into the crown region seems well captured by the modeling approach of initial fiber damage in one side of the stringer web. Model force-displacement is compared with experimental results in Figure 5.34. Unlike specimen S2C2, only one major load drop was observed in the model, but the peak load agrees well between model and experiment. The model does not experience progression of the damage down the other side of the stringer web until final failure.

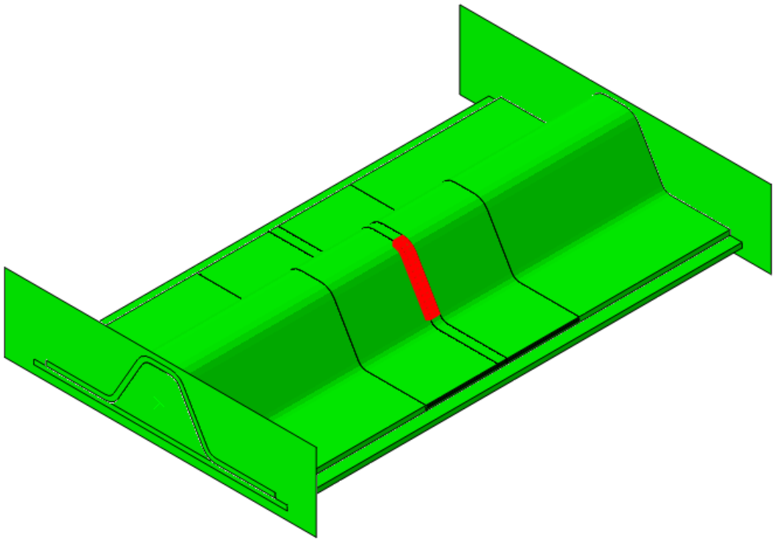

Figure 5.32. Asymmetric fiber damage element set assignment for the model of specimen S2C2.

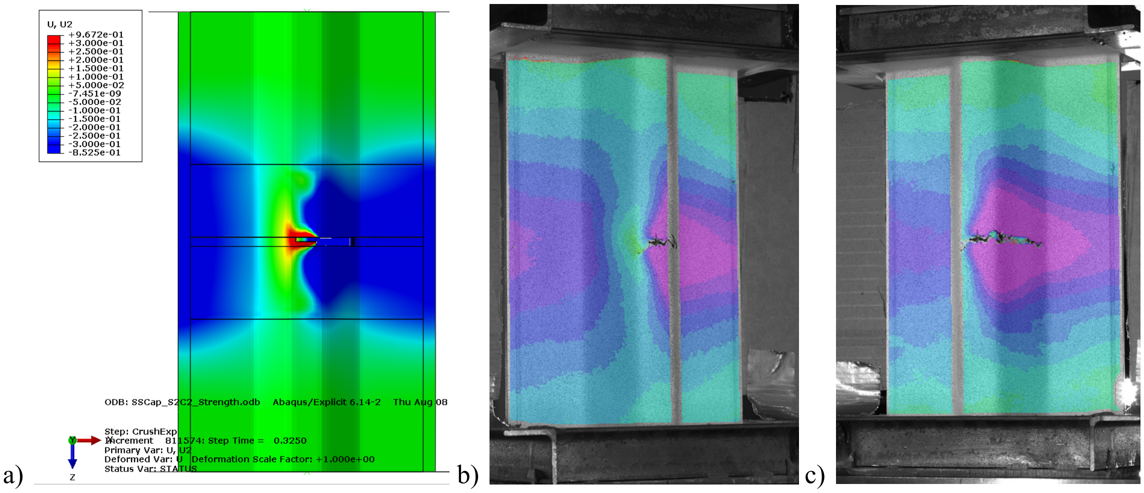

Figure 5.33. a) Asymmetric damage model displacement after first damage event. b-c) Damage observed in the DIC out-of-plane displacement results for specimen S2C2 after the first load drop in b) the left camera system and c) the right camera system

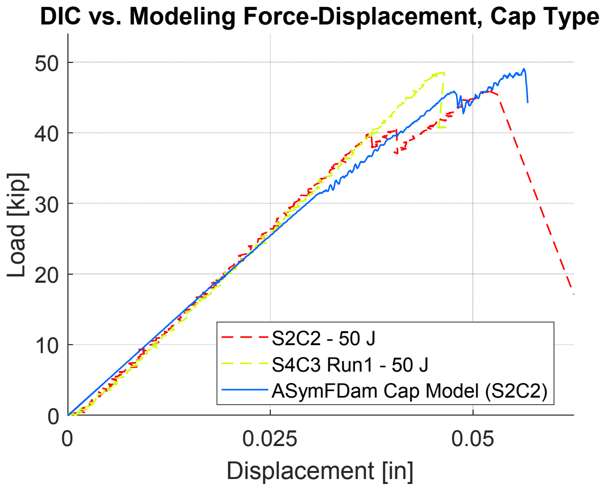

Figure 5.34. Force-displacement comparison between the asymmetric damage model and the ~47 J impacted specimens.

5.9 MODELING DISCUSSION

Several issues were encountered during the modeling process. For the single stringer panel models, limitations of the finite element formulation available in Abaqus/Explicit forced the use of linear elements to represent the curved sections of the stringer cap. Due to the linear interpolation of the curved geometry, elements were initialized with a somewhat distorted trapezoidal shape. Throughout the modeling program, certain applications of boundary conditions, mesh refinements, and mass scaling resulted in spurious oscillations (hourglassing) within the curved elements. These oscillations would often initiate at a random time in the model and seemed to be unassociated with the onset of more physical deformation modes such as buckling. An example of a model stress field illustrating the stress concentrations and oscillations is shown in Figure 5.35. This behavior was also associated with the development of large viscous damping energy, likely due to the default damping behavior in Abaqus/Explicit designed to suppress such modes. An example of the energy totals for a model with this behavior is shown in shown in Figure 5.36. This non-physical vibration behavior likely points to the difficulty in modeling curved components with linear elements. Models presented in this chapter have been carefully chosen to avoid this oscillatory behavior, but it is important to note that this behavior is mesh dependent and inherent to the presented model formulation.

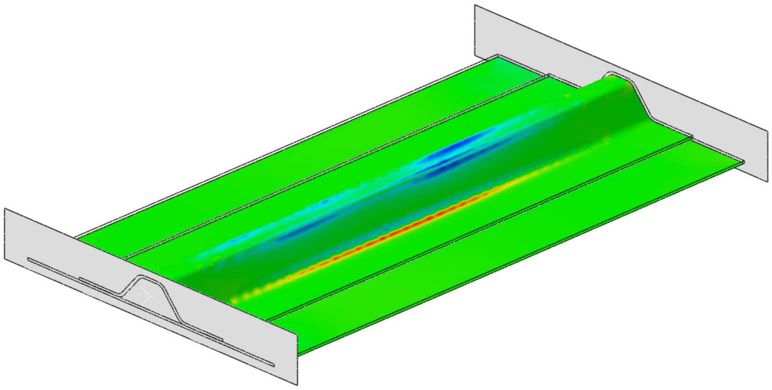

Figure 5.35. Fiber stress variable for model experiencing oscillatory behavior. Curved regions show stress concentrations due to spurious behavior.

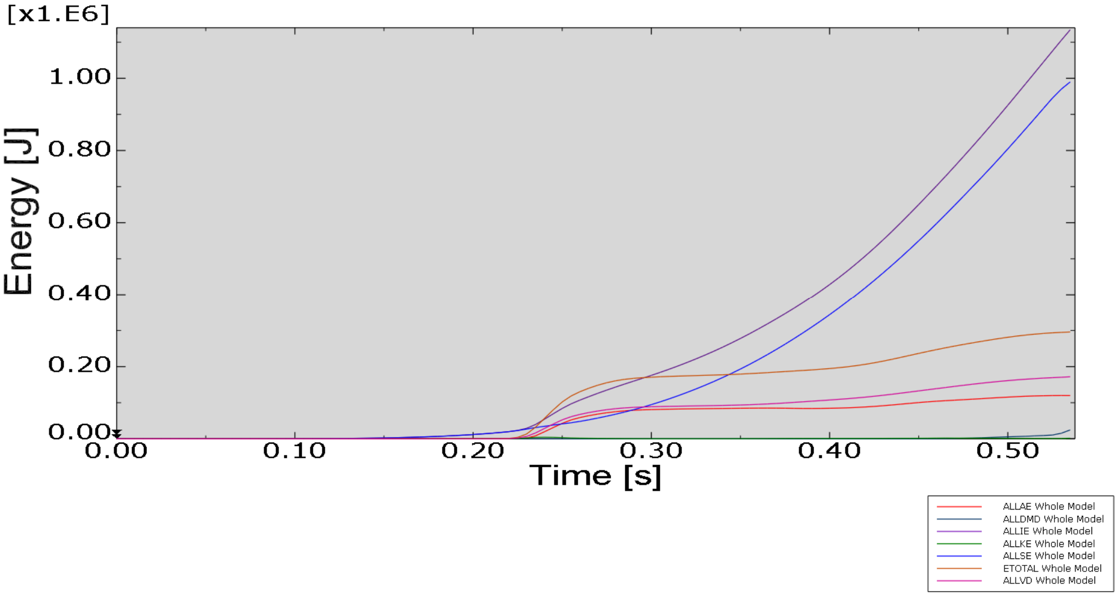

Figure 5.36.Energy totals of oscillatory behavior. Viscous damping energy starts to increase rapidly at around 0.22s in model time.

5.10 MODELING CONCLUSIONS

Despite the relative simplicity of the damage state modeling employed in the single stringer models, as compared with the flat panel modeling, overall model predictions compared more favorably with experimental results. Specifically, in configurations where significant damage modes or geometric effects from buckling strongly influenced failure behavior, these failure modes were better captured even in the simplified model. In the cap impacted model, the presence of fiber damage in the higher energy impact case permitted the use of simplified delaminations and fiber damage modeling while still capturing the major effects of these damage modes. For the flange impacted specimens, the post-buckling driven failure modes allowed for the use of simplified damage state modeling with cohesive bonded zones (and disbonded zones) only between the stringer flange and skin and greatly simplified laminate damage while still capturing the onset of failure and the failure mode. Alternatively, in the case of the flat panel model where no specific delaminations can be easily identified as the critical delamination, more complex full ply-by-ply modeling techniques were applied. However, the modeling of delamination and smeared matrix crack damage still did not fully captured the kinematics of the problem, potentially indicating that a more physically accurate model may be required that better takes into account the discontinuity behavior of matrix cracking.

5.11 NOTES/ACKNOWLEDGEMENT

Parts of Chapter 5 are taken in part from:

Pigazzini, M. S., Bazilevs, Y., Ellison, A., & Kim, H. (2018). Isogeometric analysis for simulation of progressive damage in composite laminates. *Journal of Composite Materials*, *52*(25), 3471–3489. https://doi.org/10.1177/0021998318770723. The author of this dissertation was a co-author in this work. Comparisons of CT results with IGA modeling was developed in collaboration with Marco Pigazzini.

Methods for converting NDE into flat panel CAI models are an edited version of work originally published as:

Ellison, A., & Kim, H. (2018). Computed tomography informed composite damage state model generation. *Journal of Composite Materials*, *52*(25), 3523–3538. https://doi.org/10.1177/0021998318773464. The author of this dissertation was the primary investigator and author of this study.

6 CONCLUSIONS

This dissertation presents an automated approach to analyzing X-ray CT characterization of impact damage and the resulting residual strength performance of a damaged laminated composites structure. The automated procedure identified the specimen and then utilized the exterior geometry to convert the complex 3D data set into color coded damage visualizations and 2D damage maps for each ply and interface. This CT segmentation procedure was designed to improve damage quantification in CT scans of impacted composites and transmit CT data into a format ready to be implemented into finite element modeling approaches. With this procedure, models were developed with improved representations of the initial damage state compared to previous approaches presented in the literature. The automated nature of the segmentation also improved the rapidity of CT analysis and model generation. CT segmentation results were also utilized to create and validate a predictive model for estimating the shadowed delaminations and matrix cracking in a pulse-echo UT scan of composite impact damage. This shadowed delamination estimation procedure demonstrates that NDE characterization can be potentially enhanced by an understanding of the expected damage morphology.

Additionally, an experimental characterization was presented for impact and residual response for flat and stiffened composite panels. While flat panel CAI and flange impacted stringer panels have been previously well characterized in the literature, stringer cap impacted residual strength testing has not been well studied. The cap impact specimens tested for this dissertation established a significant progressive damage growth behavior (as opposed to sudden collapse after damage initiation) and additionally showed the critical nature of cap fiber damage.

The characterization of this fiber damage by CT scanning was utilized to create models that captured this progressive behavior and well approximated the load at which the initial cap damage progressed. For the flange impacted stringer specimens, it was found that the importance of the geometric effects of the initial disbond between the stringer and skin was the largest contributing factor to the failure behavior. Modeling of these specimens was greatly simplified compared to the cap specimens due to the availability of only UT characterization of the damage state. However, these models were still able to accurately predict the failure behavior observed in the experiment. This supports the idea that the fidelity of damage modeling required to predict failure is highly dependent on the type of failure and the presence of significant damage features. Flat panel residual strength modeling proved the most difficult of the studied cases due to the complexity of the initial damage state and the lack of single dominant damage features. The flat panel damage state consisted of many smaller delaminations spread through many separate layer as opposed to the flange impact's major disbond between the skin and stringer. This diffuse damage state lead to high fidelity modeling requirements as it was difficult to effectively reduce modeled damage complexity due to an inability to identify non-critical damage features. Additionally, the presented modeling effort demonstrates that in the modeling of an initial damage state there are two major and distinct components: the definition of the damage in the model, and the determination of the damaged material behavior. While this work has shown success with modeling damage cohesive elements in Abaqus, the difficulties in modeling the flat panel CAI behavior highlight potential deficiencies of continuum damage mechanics approaches in capturing ply damage behaviors.

6.1 FUTURE RESEARCH DIRECTIONS

This work highlights several areas for improvement and further research. With regard to the modeling of NDE data, further parametric studies need to be conducted with damage modeled at varying levels of fidelity. The current models presented here for the stringer stiffened panels showed that with major damage features incorporated into the model, the force-history behavior can be decently approximated, but in order to better verify this modeling approach for a broader number of damage and load cases, it may be important to capture more of the damage features to predict features such as stress concentrations with more accuracy. Additionally, this study has been performed for single quasi-static layup cases. The significant variation in potential damage tolerance behaviors between layups may be important to consider with respect to identifying major damage features. With regard to the analysis of X-ray CT data, improvements can be made to the interpretation of pixels as damage, potentially by leveraging machine vision and other machine learning technologies.

7 REFERENCES

[1] C. Soutis, “Fibre reinforced composites in aircraft construction,” *Prog. Aerosp. Sci.*, vol. 41, no. 2, pp. 143–151, 2005.

[2] S. Abrate, *Impact on Composite Structures*. Cambridge University Press, 2005.

[3] S. Abrate, “Impact on Laminated Composite Materials,” *Most*, vol. 44, no. 4, 1991.

[4] N. Adsit and J. Waszczak, “Effect of Near-Visual Damage on the Properties of Graphite/Epoxy,” in *Fifth Conference on Composite Materials: Testing and Design*, 100 Barr Harbor Drive, PO Box C700, West Conshohocken, PA 19428-2959: ASTM International, pp. 101-101–17.

[5] Federal Aviation Administration, “Advisory Circular Advisory Circular,” *Advis. Circ.*, vol. 075, no. August, pp. 1–20, 2012.

[6] C. Bouvet and S. Rivallant, “Damage tolerance of composite structures under low-velocity impact,” *Dyn. Deform. Damage Fract. Compos. Mater. Struct.*, pp. 7–33, Jan. 2016.

[7] M. P. Delaney, S. Y. K. Fung, and H. Kim, “Dent depth visibility versus delamination damage for impact of composite panels by tips of varying radius,” *J. Compos. Mater.*, vol. 52, no. 19, pp. 2691–2705, 2018.

[8] Y. Xiong, C. Poon, P. V. Straznicky, and K. Vietinghoff, “A prediction methods for compressive strength of impact damage composite laminates,” *Compos. Struct.*, vol. 30, pp. 357–367, 1995.

[9] C. Bouvet, B. Castanié, M. Bizeul, and J. J. Barrau, “Low velocity impact modelling in laminate composite panels with discrete interface elements,” *Int. J. Solids Struct.*, vol. 46, no. 14–15, pp. 2809–2821, 2009.

[10] X. C. Sun, M. R. Wisnom, and S. R. Hallett, “Interaction of inter- and intralaminar damage in scaled quasi-static indentation tests: Part 2 - Numerical simulation,” *Compos. Struct.*, vol. 136, pp. 727–742, 2016.

[11] E. Abisset, F. Daghia, X. C. Sun, M. R. Wisnom, S. R. Hallett, “Interaction of inter- and intralaminar damage in scaled quasi-static indentation tests: Part 1 - Experiments,” *Compos. Struct.*, vol. 136, pp. 712–726, Feb. 2016.

[12] A. Riccio, A. Raimondo, S. Fragale, F. Camerlingo, B. Gambino, C. Toscano, and D. Tescione, “Delamination buckling and growth phenomena in stiffened composite panels under compression. Part I: An experimental study,” *J. Compos. Mater.*, vol. 48, no. 23, pp. 2843–2855, Sep. 2014.

[13] A. D7137/D7137M-07, "Standard Test Method for Compressive Residual Strength Properties of Damaged Polymer Matrix Composite Plates," *ASTM Int.*, no. Standard Test Method for Compressive Residual Strength Properties of Damaged Polymer Matrix Composite Plates1 This, pp. 1–17, 2012.

[14] W. Tan, B. G. Falzon, L. N. S. Chiu, and M. Price, "Predicting low velocity impact damage and Compression-After-Impact (CAI) behaviour of composite laminates," *Compos. Part A Appl. Sci. Manuf.*, vol. 71, pp. 212–226, 2015.

[15] E. V. González, P. Maimí, P. P. Camanho, A. Turon, and J. A. Mayugo, "Simulation of drop-weight impact and compression after impact tests on composite laminates," *Compos. Struct.*, vol. 94, no. 11, pp. 3364–3378, Nov. 2012.

[16] M. F. S. F. D. Moura, J. P. M. Gonçalves, A. T. Marques, and P. M. S. T. D. Castro, "Prediction of compressive strength of carbon-epoxy laminates containing delamination by using a mixed-mode damage model," *Compos. Struct.*, vol. 50, no. 2, pp. 151–157, 2000.

[17] H. Suemasu, "Analytical approaches to compression after impact (CAI) behavior of carbon fiber-reinforced composite materials," *Adv. Compos. Mater.*, vol. 25, no. 1, pp. 1–18, 2016.

[18] R. Craven, L. Iannucci, and R. Olsson, "Delamination buckling: A finite element study with realistic delamination shapes, multiple delaminations and fibre fracture cracks," *Compos. Part A Appl. Sci. Manuf.*, vol. 41, no. 5, pp. 684–692, 2010.

[19] J. Action and M. Flores, "ICME Approach to Compression Strength after Impact Modeling," no. January, pp. 1–26, 2018.

[20] C. Bisagni, R. Vescovini, and C. G. Dávila, "Single-Stringer Compression Specimen for the Assessment of Damage Tolerance of Postbuckled Structures," *J. Aircr.*, vol. 48, no. 2, pp. 495–502, 2011.

[21] R. Vescovini, C. G. Dávila, and C. Bisagni, "Failure analysis of composite multi-stringer panels using simplified models," *Compos. Part B Eng.*, vol. 45, no. 1, pp. 939–951, 2013.

[22] M. R. Abir, T. E. Tay, M. Ridha, and H. P. Lee, "On the relationship between failure mechanism and compression after impact (CAI) strength in composites," *Compos. Struct.*, vol. 182, pp. 242–250, Dec. 2017.

[23] M. Delaney, "Low Velocity Impacts of Variable Tip Radius on Carbon / Epoxy Plates," pp. 1–179, 2013.

[24] C. A. Schneider, W. S. Rasband, and K. W. Eliceiri, "NIH Image to ImageJ: 25 years of image analysis," *Nat. Methods*, vol. 9, no. 7, pp. 671–675, Jul. 2012.

[25] S. R. Stock, “X-ray microtomography of materials,” *Int. Mater. Rev.*, vol. 44, no. 4, pp. 141–164, 1999.

[26] S. C. Garcea, Y. Wang, and P. J. Withers, “X-ray computed tomography of polymer composites,” *Compos. Sci. Technol.*, vol. 156, pp. 305–319, 2018.

[27] J. F. Barrett and N. Keat, “Artifacts in CT: Recognition and Avoidance 1 Learning Objectives for Test 5 CME Feature,” *RadioGraphics*, vol. 24, pp. 1679–1691, 2004.

[28] P. J. Withers and M. Preuss, “Fatigue and Damage in Structural Materials Studied by X-Ray Tomography,” *Annu. Rev. Mater. Res.*, vol. 42, no. 1, pp. 81–103, 2012.

[29] P. J. Schilling, B. P. R. Karedla, A. K. Tatiparthi, M. A. Verges, and P. D. Herrington, “X-ray computed microtomography of internal damage in fiber reinforced polymer matrix composites,” *Compos. Sci. Technol.*, vol. 65, no. 14, pp. 2071–2078, 2005.

[30] P. Wright, X. Fu, I. Sinclair, and S. M. Spearing, “Ultra high resolution computed tomography of damage in notched carbon fiber-epoxy composites,” *J. Compos. Mater.*, vol. 42, no. 19, pp. 1993–2002, 2008.

[31] P. Wright, A. Moffat, I. Sinclair, and S. M. Spearing, “High resolution tomographic imaging and modelling of notch tip damage in a laminated composite,” *Compos. Sci. Technol.*, vol. 70, no. 10, pp. 1444–1452, 2010.

[32] F. Léonard, J. Stein, A. Wilkinson, and P. Withers, “3D Characterisation of Void Distribution in Resin Film Infused Composites,” *Conf. Ind. Comput. Tomogr.*, vol. 17, no. 12, pp. 69–76, 2012.

[33] J. E. Little, X. Yuan, and M. I. Jones, “Characterisation of voids in fibre reinforced composite materials,” *NDT E Int.*, vol. 46, no. 1, pp. 122–127, 2012.

[34] F. Léonard, Y. Shi, C. Soutis, P. J. Withers, and C. Pinna, “Impact damage characterisation of fibre metal laminates by X-ray computed tomography,” *iCT Conf.*, pp. 123–130, 2014.

[35] G. P. McCombe, J. Rouse, R. S. Trask, P. J. Withers, and I. P. Bond, “X-ray damage characterisation in self-healing fibre reinforced polymers,” *Compos. Part A Appl. Sci. Manuf.*, vol. 43, no. 4, pp. 613–620, 2012.

[36] F. Léonard, J. Stein, C. Soutis, and P. J. Withers, “The quantification of impact damage distribution in composite laminates by analysis of X-ray computed tomograms,” *Compos. Sci. Technol.*, vol. 152, pp. 139–148, 2017.

[37] F. A. Leone, “Deformation gradient tensor decomposition for representing matrix cracks in fiber-reinforced materials,” *Compos. Part A Appl. Sci. Manuf.*, vol. 76, pp. 334–341, 2015.

[38] C. Bouvet, S. Rivallant, and J. J. Barrau, “Low velocity impact modeling in composite laminates capturing permanent indentation,” *Compos. Sci. Technol.*, vol. 72, no. 16, pp. 1977–1988, Nov. 2012.

[39] A. Ellison and H. Kim, “Computed tomography informed composite damage state model generation,” *J. Compos. Mater.*, vol. 52, no. 25, pp. 3523–3538, Oct. 2018.

[40] J. C. Aldrin, J. N. Wertz, J. T. Welter, S. Wallentine, E. A. Lindgren, V. Kramb, and D. Zainey, “Fundamentals of angled-beam ultrasonic NDE for potential characterization of hidden regions of impact damage in composites,” *AIP Conf. Proc.*, vol. 1949, 2018.

[41] U. Farooq and P. Myler, “Finite element simulation of damage and failure predictions of relatively thick carbon fibre-reinforced laminated composite panels subjected to flat and round noses low velocity drop-weight impact,” *Thin-Walled Struct.*, vol. 104, pp. 82–105, 2016.

[42] F. Aymerich and S. Meili, “Ultrasonic evaluation of matrix damage in impacted composite laminates,” *Compos. Part B Eng.*, vol. 31, no. 1, pp. 1–6, 2000.

[43] M. McElroy, W. Jackson, R. Olsson, P. Hellström, S. Tsampas, and M. Pankow, “Interaction of delaminations and matrix cracks in a CFRP plate, Part I: A test method for model validation,” *Composites Part A: Applied Science and Manufacturing*, vol. 103. pp. 314–326, 2017.

[44] H. Suemasu and M. Ichiki, “Analytical study on low compressive strength of composite laminates with impact damage,” *Compos. Struct.*, vol. 104, pp. 169–175, 2013.

[45] S. Long, X. Yao, and X. Zhang, “Delamination prediction in composite laminates under low-velocity impact,” *Compos. Struct.*, vol. 132, pp. 290–298, 2015.

[46] I. Lapczyk and J. A. Hurtado, “Progressive damage modeling in fiber-reinforced materials,” *Compos. Part A Appl. Sci. Manuf.*, vol. 38, no. 11, pp. 2333–2341, 2007.

[47] P. P. Camanho and C. G. Dávila, “Mixed-Mode Decohesion Finite Elements for the Simulation of Delamination in Composite Materials,” *Nasa/Tm-2002-211737*, no. June, p. 42, 2002.

[48] M. S. Pigazzini, “An Isogeometric Analysis Framework for Progressive Damage Modeling of Multi-Layer Composite Materials,” 2018.

[49] M. S. Pigazzini, Y. Bazilevs, A. Ellison, and H. Kim, “Isogeometric analysis for simulation of progressive damage in composite laminates,” *J. Compos. Mater.*, vol. 52, no. 25, pp. 3471–3489, Oct. 2018.

[50] C. Soutis and P. T. Curtis, “Prediction of the post-impact compressive strength of CFRP laminated composites,” *Compos. Sci. Technol.*, vol. 56, no. 6, pp. 677–684, 1996.

[51] R. M. Sencu, Z. Yang, Y. C. Wang, P. J. Withers, C. Rau, A. Parson, and C. Soutis, “Generation of micro-scale finite element models from synchrotron X-ray CT images for multidirectional carbon fibre reinforced composites,” *Compos. Part A Appl. Sci. Manuf.*, vol. 91, pp. 85–95, 2016.

[52] A. Abdul-aziz, D. J. Roth, R. Cotton, G. F. Studor, and E. Christiansen, “Material Characterization and Geometric Segmentation of a Composite Structure Using Microfocus X-Ray Computed Tomography Image- Based Finite Element Modeling,” no. July, 2011.

[53] M. David Flores, “Damage Tolerance and Assessment of Unidirection Carbon Fiber Composites: an Experimental and Numerical Study.”

[54] O. Allix, P. Ladevèze, and E. Vittecoq, “Modelling and identification of the mechanical behaviour of composite laminates in compression,” *Compos. Sci. Technol.*, vol. 51, no. 1, pp. 35–42, Jan. 1994.

APPENDICES

A. APPENDIX. DESCRIPTION OF UCSD LIBRARY HOSTED DATABASE

Due to the large and digital nature of the data sets collected throughout the course of this work, a publically available digital repository was established through the UCSD Library to host the data sets. For each specimen tested a large number of different data types were collected including: impact and residual strength testing curves, UT scanning, X-ray CT scanning, and digital image correlation photos.

These digital data collections can be found at the following locations:

Ellison, Andrew C.; Kim, Hyonny (2020). Flat Panel Impact and Residual Strength Testing and Characterization by Ultrasonic and X-Ray Computed Tomography Non-Destructive Evaluation. UC San Diego Library Digital Collections. https://doi.org/10.6075/J01C1V8V

Ellison, Andrew C.; Kim, Hyungsuk Eric; Kim, Hyonny (2020). Stiffened Composite Panel Impact and Residual Strength Testing and Characterization by Ultrasonic and X-Ray CT Non-Destructive Evaluation. UC San Diego Library Digital Collections. https://doi.org/10.6075/J0N29VB8

These datasets describe a set of impact and compression after impact (CAI) residual strength tests and accompanying non-destructive evaluation (NDE) data. The data has three major divisions: impact testing, NDE collection, and CAI testing.

Impact testing data primarily consists of force-history impact curves, residual indentation measurements and some accompanying photos.

Non-destructive data collected for this specimen include X-ray computed tomography (CT) and ultrasonic pulse-echo (UT) scanning. CT data is available as .att, .raw, and .tif formats.

ATT (.att) format files correspond to the collected X-ray attenuation images collected. RAW (.raw) format files correspond to the dataset as reconstructed by VGStudio and are associated with the accompanying header (.hdr) and project (.vgl) files. TIFF (.tif) format files are the CT database output as image slices provided in a stacked format. UT data is .mat format. MAT (.mat) files are Matlab readable database files that include each A-scan and relevant scanning parameters, these files are also readable with Python.

CAI testing data consists of the force-displacement curve, digital image correlation (DIC) images collected by 2 stereo camera pairs for the front and back of the specimen, and accompanying testing images (including post-failure damage state photos). DIC images are provided in .tif format with an .xls file describing the DIC frame count connection with the loading of the specimen. DIC processed output is provided as Vic3D output and project files (.out and .Z3D) and as MAT (.mat) Matlab output.